AN ABSTRACT OF THE DISSERTATION OF

Jude Ogheneyoreme Ighere for the degree of Doctor of Philosophy in Materials Science presented on April 11, 2019.

Title: Point Defects and Impurities Adapted Phonon Thermal Properties of Zirconium Diboride: Its Influence on Thermal Conductivity, Thermal Expansion and Specific Heat.

Abstract approved: _____

Liney Arnadottir and P. Alex Greaney

The study outlined in this dissertation elucidate the thermal and structural properties of ZrB_2 based ceramics as choice materials for high temperature applications. Thermal properties were investigated to improve understanding on aspects that are affected by point defects and impurities at nanoscale and electron level using a combination of lattice dynamics, molecular dynamic (MD) simulations and density functional theory. Macroscopic approach to heat transfer is limited as characteristic time and length scale reduces and become analogous to phonon relaxation times and mean free path over the stages transfer. A correlation between atomic structure property and thermal parameters were investigated using phonon (lattice vibration) analysis. In this study is described thermal contribution in a collaborative effort to develop a defect-adaptive predictive model for zirconium diboride (ZrB_2) properties. This portion focuses on the thermal property of point defects and impurity defects of metallic and covalent form. Introduction of defects into perfect ZrB_2 to tune or investigate the variations in its thermal conductivity, expansivity and heat capacity for desired application provides endless space for controllable parameters.

Green-Kubo (GK) method which is well established in the study of transport phenomena was applied to compute thermal transport with expected differences in heat current in the

various axial directions. It relates the thermal conductivity of solids to the integral of autocorrelation of heat current within the lifetime of the fluctuations. Evolution in the microstructure of ZrB_2 under thermal stress was studied. Temperature dependency of the coefficient of thermal expansion (CTE) and anisotropy observed in the elongation of lattice parameter of ZrB_2 were presented. Lattice vibration also characterizes the capacity for materials to store thermal energy storage. Phonon-based constant volume heat capacity trend with temperature is shown in the presence and absence of impurities (C, Si, Hf, W). The energy level changes in the valence and conduction region due to impurities were characterized. Calculations of total and projected density of states using density functional theory (DFT) to understand atomic level variation are shown and compared to phonon dispersion. Dynamic stability of structures in the presence of covalent and metallic impurities were correlated to the imaginary and non-imaginary modes of phonons.

Point Defects and Impurities Adapted Phonon Thermal Properties of Zirconium Diboride: Its Influence on Thermal Conductivity, Thermal Expansion and Specific Heat.

by

Jude Ogheneyoreme Ighere

A DISSERTATION

Submitted to

Oregon State University

in partial fulfillment of
the requirement for the
degree of

Doctor of Philosophy

Presented April 11, 2019
Commencement June 2019

Doctor of Philosophy dissertation of Jude Ogheneyoreme Ighere presented on April 11, 2019

APPROVED:

Major Professor, representing Materials Science

Director of the Materials Science Graduate Program

Dean of the Graduate School

I understand that my dissertation will become part of the permanent collection of Oregon State University libraries. My signature below authorizes release of my dissertation to any reader upon request.

Jude Ogheneyoreme Ighere, Author

ACKNOWLEDGEMENTS

My gratitude cannot be conveyed in writing to all the amazing educators, researchers, classmates and friends I have been privileged to meet. These people have contributed positively to my life in so many ways. Everyone has played a vital role in the course of my life and graduate career. Therefore, I will make this a short list of those who have directly and indirectly impacted my experience at Oregon State University and otherwise to the framework of the work presented here.

To my advisor, Professor P. Alex Greaney: I am forever grateful and indebted for all the support, commitment and patience you have displayed towards this project and to my personal development, for your keen willingness to teach and explain concepts to your students. To my co-advisor, Professor Liney Arnadottir: Thank you for all the advice and encouragement right from the first day I visited your office and for moving your group meeting just to fit my evening schedule. I thank my other committee members Professor Brian Bay, Professor David Cann, Professor Todd Palmer and Professor Laurence Schimleck (GCR) for making my journey in Oregon State University a success and for their support and readiness throughout the dissertation process. Professor William Warnes and Professor Alex Greaney taught courses that setup me up for structure-property relations of materials and molecular dynamics.

Acknowledging teammates and collaborators, all whom have become great friends over the years both at Oregon State University and at University of California River Side: Laura de Sousa Oliveira, Aria Hosseini, Jackson Harter, Agnieszka Truszkowska and Pegah Mirabedini. I also want to thank Kingsley Chukwu and Sean Seekins from Professor Liney Arnadottir's group who have responded to some of my emails for resources. To Juliet Claudio-Ighere, my spouse, I am forever grateful for her sacrifice and support throughout this process. Thanks to my son,

Adrian and my daughter, Esther for unknowingly sacrificing their time towards my academic pursuit.

Thanks to Oregon State University for providing me with enabling environment and resources (tools) required for this project including software licenses (Matlab, Python, Mathematica, JMP) which are very pricy. This work used the computing resources of Extreme Science and Engineering Discovery (XSEDE). This academic opportunity was made possible by the education assistance program provided by my employer (Intel). My ultimate praise goes to God who has kept me alive and gave me the needed strengths to embark on this journey.

TABLE OF CONTENTS

Page

TABLE OF CONTENTS (Continued)

TABLE OF CONTENTS (Continued)

LIST OF FIGURES

Figures Page

LIST OF FIGURES (Continued)

Figures Page

LIST OF TABLES

Tables Page

1. Introduction and Relevance of Research

Next generation of materials for advanced thermal applications, particularly at the leading edges of hypersonic vehicles as well as missile systems require thermal properties and microstructural capability that can withstand temperatures in excess of 1500^{o} C and erosion forces. Recent advances in technology have simultaneously demanded mechanically reliable, chemically resistant and advanced thermally stable materials [1, 2, 3, 4]. Transition metal diborides are ultra-high temperature ceramics (UHTC) with melting temperatures exceeding ~ 3000^{o} C, hence are favorable candidates for advanced thermal engineering (Fig. 1.1). In the space craft industry, leading edges and sharp nose design have required ultra-high temperature ceramics (UHTC) due to drag generated high temperatures at these locations which increases with decreasing radius at the stagnation points [1, 5]. Since temperatures at leading edges are high, hypersonic designs are only possible if the conduction and re-radiation of heat from these edges are improved by enhancing the thermal properties of the applicable materials. Therefore, tuning material property to improve thermal insulation or conductivity is critical for safer, more adaptable aircraft. Another applicable area of interest is in microelectronics where Moore's law has continued to drive the size reduction of integrated circuits and thus challenges thermal diffusivity and material endurance. The aspect ratio shrinkage in complex integrated devices presents emerging challenges for device thermal efficiency contributing to failure due to leakage [6]. It is therefore necessary to determine ways to optimize the energy dissipation mechanism by improving properties of the materials used around the high heat-generating regions.

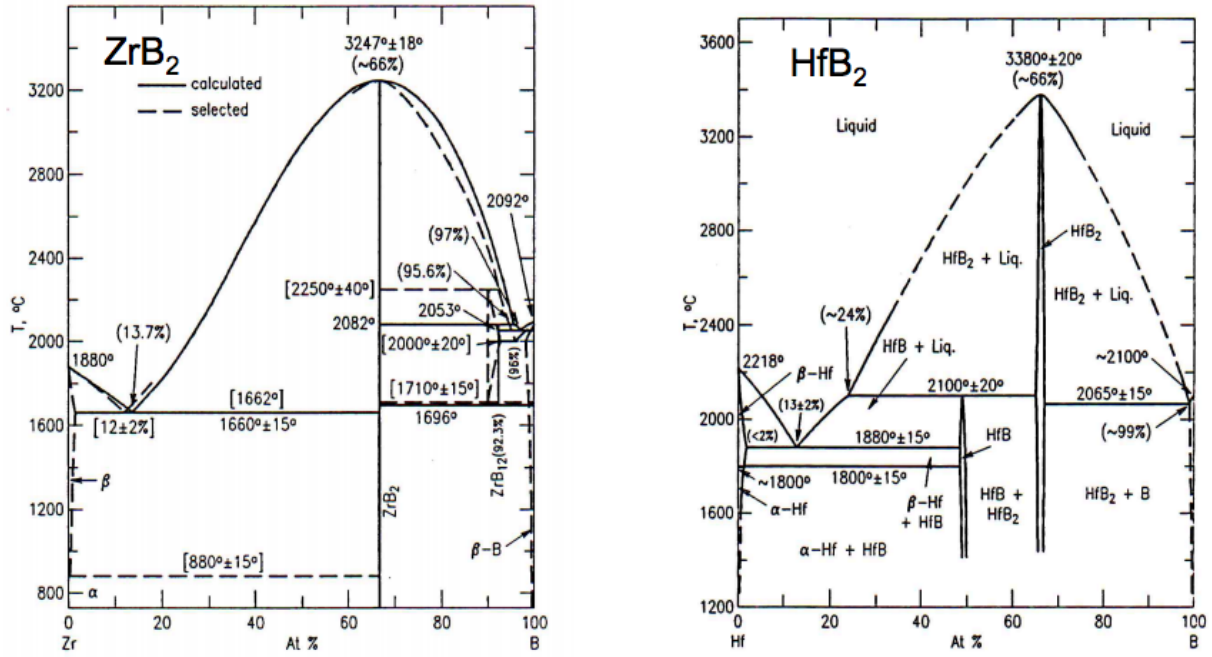

Fig. 1.1 Phase diagram of ZrB_2 and HfB_2 showing very high melting temperatures [65].

Quantized lattice vibration that carries energy through crystalline solids is termed phonons and has been known to dominate the atomic level heat transfer processes in insulating materials [7]. Depending on the application, either low or high thermal conductivity could be desirable for performance enhancement. While high thermal conductivity is required for downscaled integrated circuits in electronic devices, hypersonic flight and rocket propulsion, in thermoelectric applications low thermal conductivity is desirable in materials [9, 10]. It is therefore critical to understand the atomic level property and technique to adapt materials for particular applications.

But there are challenges with micro- and nano- scale computations. Understanding the basic mechanism of heat propagation at the atomic scale in materials of interest is a major challenge. Phonons and Electron propagation are the underline vehicle for thermal transport in solids. While electronic transport dominates the mechanism in metals (conductors), phononic

transport is the primary carrier in semiconductors and insulators. However, solutions to Schrödinger's equation for complex systems is difficult and immense computational resources is required. Thus, neglecting electrons to minimize computational resources. At atomic scale, the conventional model of heat transfer may not precisely explain the heat transfer in all materials as it assumes that the material is a continuum (classical), ignoring electronic contributions. Device performance and material structural endurance are dependent on nature and composition of its crystal structure which are both investigated in atomic level simulations. Imperfections such as point defects and impurities are among compositional and structural changes that impact phonon scattering and changes its group velocity [8,9,10]. Therefore, the thermal conductivity across crystal lattice is impacted mainly by scattering the heat propagating phonons due to the presence of impurities, vacancies, interstitials and grain boundaries. The modification of thermal properties of ultra-high temperature transition metal diboride ceramics by imperfections are investigated in this study. In depth understanding of defects and defect interaction with dissimilar materials is required for desirable modification of phonon dispersion curve for materials of interest. Wide variation in the literature reported thermal conductivity (Table 1) values of ZrB_2 can be attributed to intrinsic imperfections in microstructure from production process.

Table 1.1: Variation in Thermal Conductivity at 25^{o} C for pure ZrB_2 and Sintering Techniques

Corresponding Authors	Synthesis and Sintering Processes of ZrB_2	Thermal Conductivity @ 25°C (W/m•K)
Guo et al [66]	Reaction Spark-Plasma Sintering of ZrH_2 and B powders that were ball-milled with SiC media	133.01
Zhang et al [67]	Spark-Plasma Sintering of commercially available	108

Thompson et al [69]	Hot-Press Sintering of commercially available ZrB_2 that was ball-milled with ZrB2 media	92
Thompson et al [69]	Hot-Press Sintering of commercially available ZrB_2 that was attrition-milled with WC media	58.7
Zimmermann et al [68]	Hot-Press Sintering of commercially available ZrB_2 that was attrition-milled with WC media	56

1.1 Conduction Heat Transfer in Solids

Several studies in the 20th century advanced microscale and nanoscale physics to explain macroscale heat transfer formulation [60-61]. The famous Fourier and Cattaneo equations does not model microscopic heat transfer despite its vast application in macroscopic level. Majumdar et al reported that Fourier's equation over predicts actual heat flux and is incomparable to experimental data at smaller time and length scales [61]. The form of conduction equation derived from combining energy conservation with Fourier law, assuming constant mass is expressed as;

$$k\nabla^2 T = \rho C_v \frac{\partial T}{\partial t} \qquad 1.1$$

where C_v, ρ, t represents specific heat capacity, density and time respectively. And k refers to thermal conductivity of medium while T is temperature. It is noteworthy that thermal conductivity is a tensor property, and thus in highly anisotropic crystals, k here will be replaced by appropriate Cartesian indices. Equation 1.1 assumes that the energy carrier transport is diffusive, and also does not describe heat transport in materials when length and times scales are relative to relaxation time and mean free path of phonons (or electrons). Equation 1.1, is

therefore, not representative at small length and time scales characterization of transport. Approaches such as Boltzmann's transport equation has been applied towards phonon transport and scattering mechanism in a bid to describe size and time scales of heat transfer capturing boundaries and imperfections but depend on bulk property predicted from phonon modes experimentally (e.g. carrier mean free path). Other computational methods such as classical MD simulations for lattice dynamics and density functional theory for electronic structure emerged to further advance studies on atomic level heat transfer. Molecular dynamic gives the time evolution of complex systems using phonon space that otherwise cannot be studied analytically. The atomic distortion due to lattice vibration is captured in particle position overtime. Phonon space correlates the time evolution to phonon population in the system using frequency and wave vector.

1.2 Real Space and Phonon Region of Heat Conduction

Phonon contribution to heat transfer depends on the amount of constructive lattice vibration and destructive ones which determines how far phonons travel in the material before scattering. Heat transport in diborides based ceramics is largely dependent on phonon propagation (or phonon scattering mechanism). This work is focused on the transition metal diborides, ZrB_2 which are ultra-high temperature ceramics. Analysis of microstructure and phase changes are presented in a frequency (wave)-based model and intensity along path of high symmetry, which is described as the phonon space. Molecular dynamic (MD) approach was used to study the phonon properties of the material. MD simulations applies Newton's law of motion to predict the position and momentum (real space) of a system of particles. Therefore, creating a bridge between real space analysis (macroscopic) and phonon space (atomic level behavior) given the

interatomic potential and lattice structure. Two approaches are adopted in MD simulations when computing thermal transport: (1) non-equilibrium system driven by perturbation to measure response, or (2) equilibrium system simulation to measure local fluctuations using Green-Kubo formulation. In this study, the equilibrium simulation approach was adopted for thermal conductivity calculations with our introduction of enthalpy correction technique.

Material modeling in heat conduction is divided into four sublevels based on spatial and temporal regimes. The characteristic sizes and times in material modeling are subdivided as shown in Table 1.2. Macroscopic and microscopic formulations have been popular in the literature, where nanoscale is commonly grouped with microscopic formulations due to size and time dependence transport mechanisms.

Table 1.2: Characteristic sizes and times in material modeling [62]

Sublevel	Size (m)	Time (s)
Macroscale	$>10^{-3}$	$>10^{-3}$
Mesoscale	$\sim10^{-4}$ - 10^{-7}	$\sim10^{-3}$ - 10^{-9}
Microscale	$\sim10^{-6}$ - 10^{-8}	$\sim10^{-8}$ - 10^{-11}
Nanoscale	$\sim10^{-7}$ - 10^{-9}	$\sim10^{-10}$ - 10^{-14}

1.2.1 Time in Microscopic Thermal Transport

Time and size characterizes simulations in the microscopic regime. Time stages (or parameters) heat transport processes or simulations are categorized [60]:

The time is takes for a system of particles to reach thermal equilibrium is referred to as the **thermalization time**

The time that elapsed for information to travel through an entire field (medium) is termed the **diffusion time**

The time it takes for the particle (electron) to attain average velocity between successive perturbation in a system is called the **relaxation time**

The time an external heating source (thermostat) is applied to a system is called **heating time**. The opposite is the case for **cooling time**

The total time duration of interest setup for the physics of the system or process is regarded as the **physical time**

When the relaxation time or the diffusion time is equivalent to the heating time, the finite speed of propagation becomes relevant. Similarly, when the thermalization time is equivalent to the heating time, the energy transferred (deposited) by the carrier becomes quantifiable. More importantly is, when the physical time becomes comparable to any of the above times in a system, the time scale is characterized as microscopic in time.

1.2.2 Size in Microscopic Thermal Transport

Goodson and Flik referred to two crucial size parameters that control thermal transport in a system, which are the (1) mean free path, λ and (2) the characteristic dimension, L of the material [60]. Fourier law becomes applicable when the mean free path is much less than the characteristic dimension as the heat transfer is diffusive and the system therefore is macroscopic. On the other hand, the system is characterized as microscopic in size if the mean free path is comparable to the characteristic dimension of the material or greater. Hence, different methods are often combined to explain transport mechanism and improve accuracy.

The objective of this work focuses on the impact of imperfections (point defects and impurities) on thermal properties of zirconium diboride ZrB_2 and its relation to structural properties. The overall goal in a collaborative effort is to predict material composition and microstructure based on desired eleastic, electrical and thermal properties for specific application. In the course of my research, the first subject addressed was the intrinsic properties of defect-free ZrB_2, explaining its phonon dispersion, density of states and thermal properties of the material. The properties in the presence of point defects using the equilibrium MD adopted and calculations of thermal conductivity performed in the Green-Kubo method (chapter 3). In chapter 4, structural changes and thermal storage potential of ZrB_2 were evaluated with imperfections. It presents the thermal expansion coefficients, its temperature dependency and anisotropy in lattice parameters. Heat capacity analysis with energy changes was also presented and DFT calculations of impurities. The impact of covalent (Si and C) and metallic (Hf and W) impurities on the stiffness and thermal conductivity was presented in chapter 5. Some of the band structure properties from chapter 4 are repeated for corresponding impurities in chapter 5. It combined classical simulations data with results from first principle calculations to correlation the thermal changes with the energy changes. In each chapter (3-5), additional details on background and methods are included in the paper. The main introduction and background provides interesting literature references and the relevance of transition metal diborides (Chapter 1 and 2).

2. Background and Literature Review

a. Lattice Dynamics and Bonding of Zirconium Diboride

Zirconium diboride belong to the family of hexagonal isostructural transition metal diboribes (TMB_2) with a AlB_2-type 4d crystal structure [11] with space group P6/mmm. The structure is a repeating layer of boron atoms with the zirconium atoms arranged in an alternating hexagonally closed packed layer as depicted in figure 2.1. Individual boron atoms are surrounded by three in-plane boron atoms and six zirconium atoms in adjoining plane while zirconium atom in the hexagonal closed packed plane is surrounded by six zirconium atoms as nearest neighbors and twelve boron atoms as nearest neighbors on opposite sides of the plane. The strange properties of this material have been attributed to its multi-bonding types. The boron-layered structure is

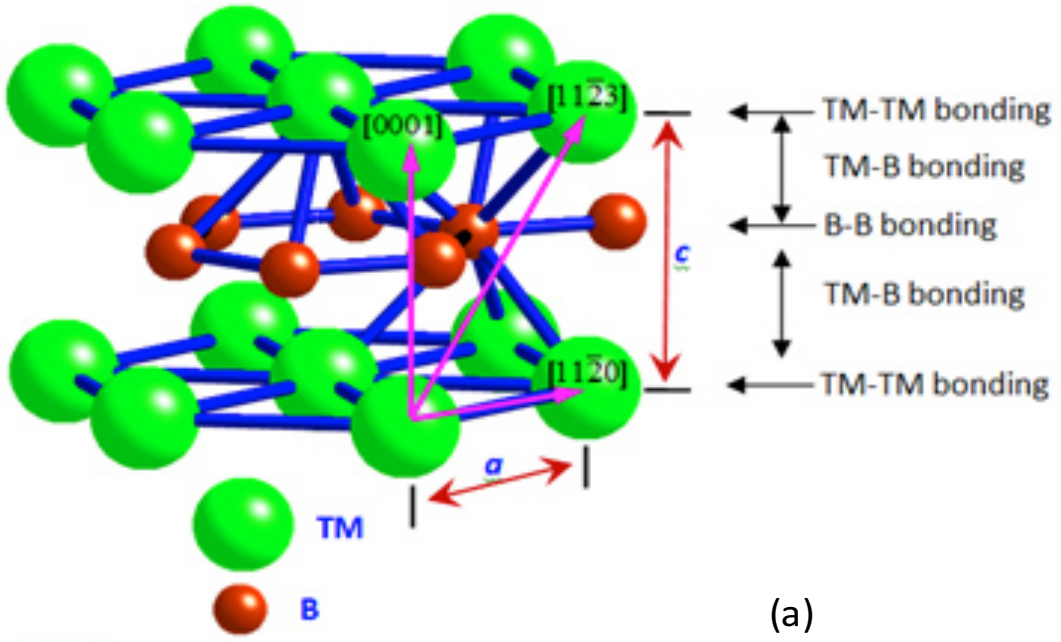

(a)

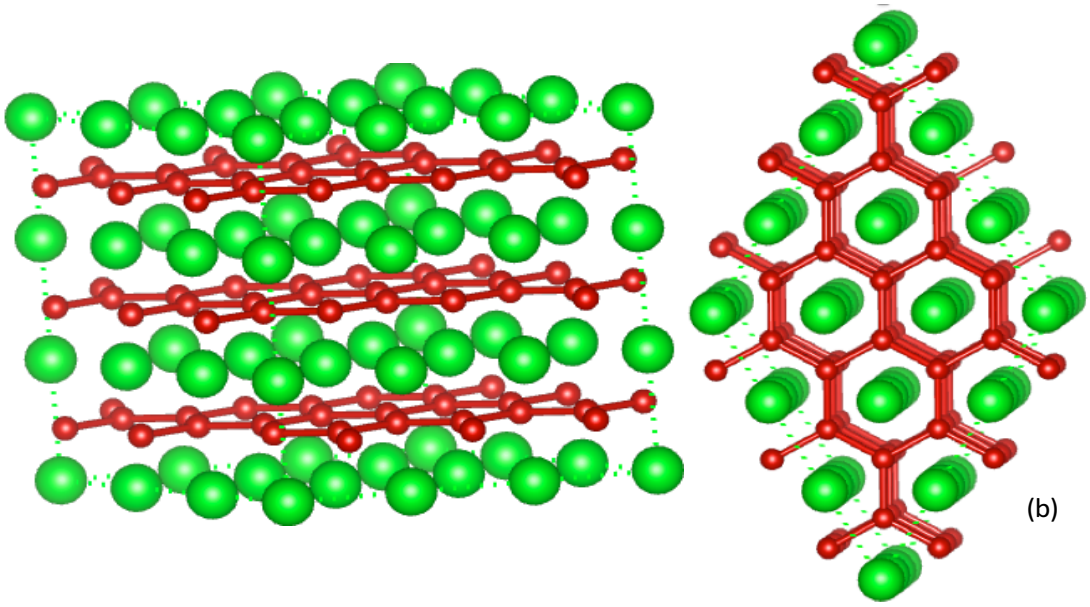

Fig. 2.1 Depiction of zirconium diboride alternating layer of boron (red) and zirconium (green): (a) bonding, (b) side-view and top-view

similar to the hexagonal planes of carbon atoms in graphite but unlike carbon, boron atoms only have three valence electrons. Like carbon atom in graphite, boron bonds to its nearest neighbor boron atoms to form strong sigma bond within the planes and weak pi bond between planes (interlayer bonding). Thus, since there are only three valence electrons available in a boron atom, some of the sigma bonds are not filled and thereby enhancing lattice vibration in the boron planes [12]. Researchers have attributed the characteristic stiffness of ZrB_2 to the strong boron-boron covalent bonds and the thermal conductivities to the metallic bonds [13].

2.2 Theory and Mechanism of Phonon Interaction in Molecular Dynamics Simulations.

Atoms or molecules in crystalline solids are not at rest but in a state of continuous vibration about an equilibrium position at specific temperatures. These small amplitude

vibrations collectively give rise to the propagation of elastic waves in crystalline solids. The quantized unit of this vibration across the crystal lattice is termed Phonon [17]. In classical mechanics, time evolution analysis of the sequence of atomic or molecular displacements about their regular lattice sites are performed. This quantized vibrational wave called phonon can be characterized by its velocity of propagation, thermal (vibrational) energy, wave vector (or wave number) and frequency of vibration [14,15]. Phonon contributions to thermal properties are categorized by the type of vibrational modes (acoustic or optical phonons) exhibited across the crystal lattice. These are not independent, and the relationship between the wavevector and the frequency of a vibrational wave propagating through a crystal lattice is referred to as the dispersion relation.

For acoustic phonons, the displacement of collective atoms by the same amplitude and direction, and are therefore in-phase resulting in increased group velocity while atoms in optical phonons are displaced in opposite direction and amplitude, giving a zero-group velocity. These two types of phonons are depicted in Figures 2.2 and 2.3. A distinctive relationship exists between the wave vector and the frequency of a vibrational wave propagating through a crystal lattice referred to as the *dispersion relation.*

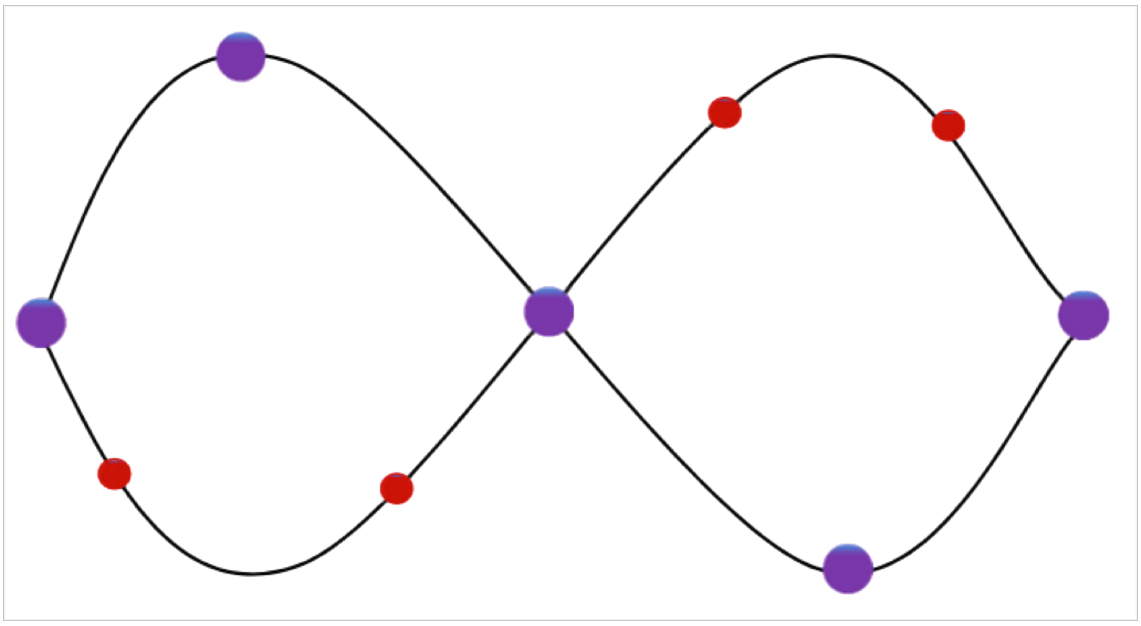

Fig. 2.2: Depicting optical phonon- displacement of two atoms are in opposite amplitude and direction

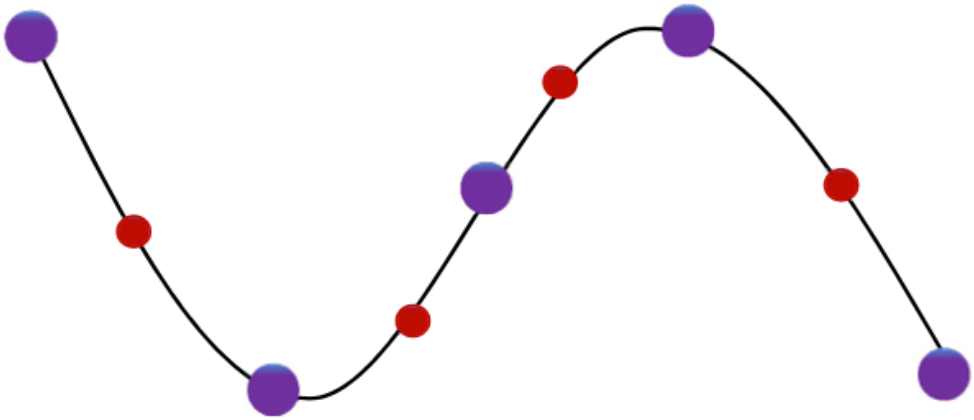

Fig. 2.3: Depicting acoustic phonon- displacement of two atoms are in same direction and amplitude.

Dispersion Relation. Since phonons are the dominant heat carriers in ceramics, understanding the phonon- boundary scattering is vital for effective control. Introducing boundary conditions changes the scattering rates and therefore modifies the thermal properties [16]. One-dimensional

mass-spring representation is often used for the analogy of vibrations in crystals as shown in Figure 2.4. For an atom located at position X_{na} and $X_{(n+1)a}$, the equations of motion are as follows:

$$m_1 \frac{d^2 X_{na}}{dt^2} = -C[2X_{na} - X_{(n-1)a} - X_{(n+1)a}] \quad 2.1$$

$$m_2 \frac{d^2 X_{(n+1)a}}{dt^2} = -C[2X_{(n+1)a} - X_{na} - X_{(n+2)a}] \quad 2.2$$

where C is the spring constant, m_1 and m_2 are the masses of atoms subjected to spring force and X_{ia} is the position of the atoms in the chain with separation a.

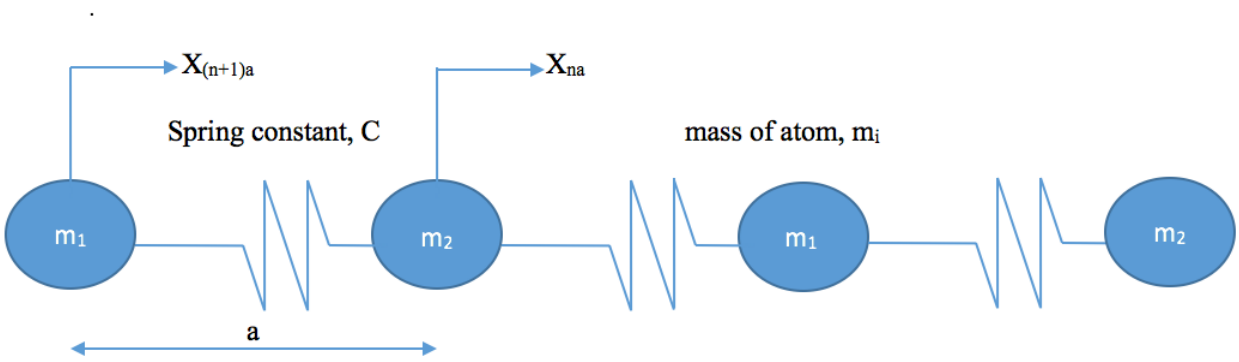

Figure 2.4: 1-Dimensional chain representation of lattice vibration

The solution to this 2-order differential equations, or equation of motion (equation 2.1) is the standing wave and the represents the dispersion relation [17, 18] (see equation 2.2).

$$\omega^2 = \mathrm{C}\left[\left(\frac{1}{m_1} + \frac{1}{m_2}\right) \pm \sqrt{\left(\frac{1}{m_1} + \frac{1}{m_2}\right)^2 - \frac{4}{m_1 m_2} sin^2|\boldsymbol{k}|\boldsymbol{a}}\right] \quad 2.3$$

where **k** is the wavevector, with magnitude $|\mathbf{k}|=2\pi/\lambda$, a represents the equilibrium separation between atoms and ω represents the frequency.

Therefore, dispersion relation relates the wave vector, **k** to the energy (i.e., frequency) of a phonon. The solution in equation 2.3 gives two values of ω for each k value. A plot of the frequency, ω against the wavevector, **k** shows two branches in the dispersion relation which represent both values. These branches on the dispersion curve are referred to as acoustic and optical branch (see Figure 2.5).

Although, there is a mathematical relationship between wave vector, k to the energy (i.e., frequency) of a phonon, dispersion curve clearly defines the allowable phonon modes (vibrational modes) because the atomic structure does not support all values of k. The speed of propagation of these phonons in the crystal or crystalline solid is given by group velocity, V_g (equation 2.4). And it is obtained from the slope of the dispersion curve, and because phonons are quantized energy carriers in conductors and semiconductors, group velocity represents the velocity at which energy is transported in crystals. However, the phonons (and therefore the amount of energy) is limited for a given level due to the density of states.

$$V_g = \frac{d\omega}{d\mathbf{k}} \approx a\sqrt{\frac{g}{m}} \qquad 2.4$$

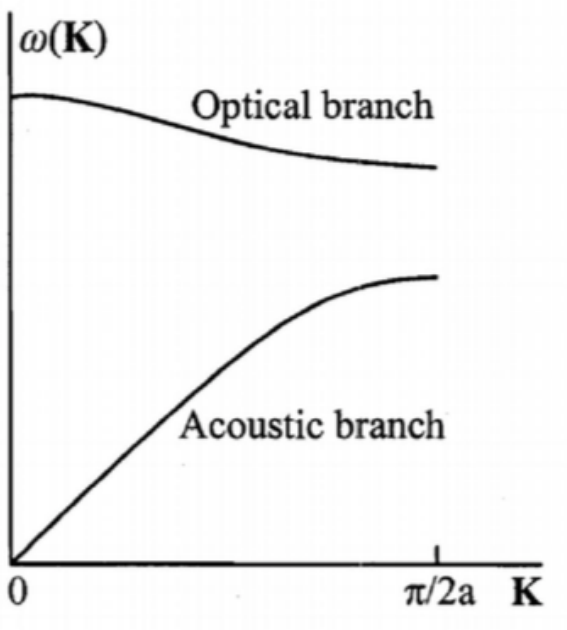

Figure 2.5: 1-D representation of dispersion relation for diatomic crystal vibration [19]

Phonon Density of States. It presents in a system, the number of states for a given energy level that are available and provides the energy distribution and the carrier concentrations within the system.

2.3 Computational Methodology: Classical and Quanta-Mechanical

Molecular dynamics (MD) is one of many computer simulation methods used to model the behavior of complex systems in science and engineering, to gain insight or estimate performance into idea of interest [20]. MD comprises different techniques or algorithm to compute many particles interactions at the atomistic level. In classical MD, the position and momentum of these particles are simulated by integrating Newton's laws of motion. The forces between atoms can be either computed from first principles by solving the Schrödinger's equation, or approximated using system of non-linear response with properties and functional form that are tuned to fit empirical data. The computed results for the properties at the

microscale can therefore be optimized to estimate macro-scale properties based on the appropriate periodic boundary conditions. According to Heisenberg uncertainty principle, experimental methods have limitations in the accuracy of measuring both the positions and momenta of these particles. Thus, MD simulation is a valuable tool for resolving a variety of challenges in experimental thermal transport, strength of material, physics of atoms and chemical reaction processes. In some cases, improved force fields parameters and longer MD trajectories have yielded approximate quantum effect [21,22]. Other approaches apply quantum mechanics to calculate material behavior. For instance, density functional theory (DFT) simulation approach solves a simplified form of the many body Schrödinger equation in which the many body exchange and correlation effects are approximated in a single exchange-correlation functional of the electron density [58, 59]. The hybrid of both classical MD and electronic structure methods are also used in other approaches such as the Car-Parrinello formulation. Sections 3.3.1 and 3.3.3 presents further details on these methods. However, Richard Lesar's "*Introduction to Computational Materials Science: Fundamentals to Applications*" is a useful text for thorough detail on this subject [64].

2.3.1 Classical Molecular Dynamics (CMD) and Interatomic Potentials

Classical MD has been used to obtain both particles position and momentum with a degree of accuracy in the simulation based on computational resources. In many problems of interest, there has not been a key concern in the difference in the results obtained between classical and quantum. Computing thermodynamic and dynamic properties of different system does not necessitate quantum mechanics. Hence, classical MD has not been outdated by quantum mechanics (QM). Empirical potentials are considerably quicker to compute than DFT and so

while not accurate, they enable one to simulate much larger systems for much longer times. Furthermore, the long correlation times required for crystals to eliminate noise in the trends are possible through classical MD simulation due to significantly affordable computational resources. And therefore, thousands of atoms in one supercell can be simulated if required for improved accuracy.

The MD simulation generates a trajectory of all particles as sequence of points in phase space as a function time in the system. From the trajectory, various properties including time averages can be calculated. The time evolution of the system of particles in phase space is defined by Hamiltonian mechanics:

$$\frac{dr}{dt} = \frac{\partial H}{\partial p_i}$$
$$\frac{dp}{dt} = \frac{\partial H}{\partial p_i} \qquad 2.5$$

The Newton's equation of motion for each atom along independent coordinates is resolved numerical for all N particles:

$$\dot{X} = \frac{\partial H}{\partial p_i} = \frac{p_i}{m} = v_i \qquad 2.6$$

$$\dot{p_X} = -\frac{\partial H}{\partial \mathrm{X}} = -\frac{\partial V(X)}{\partial X} = \mathrm{F_x} = \mathrm{ma_x}$$

where a is the acceleration of the atom of mass m in the x-direction, F is the force applied on the atom, V(x) is the potential energy and ν_i is the velocity. Figure 2.6 shows the steps-by-step procedure in setting up an MD simulation. It starts with selecting the correct interaction model

and boundary conditions required in force field and force calculations:

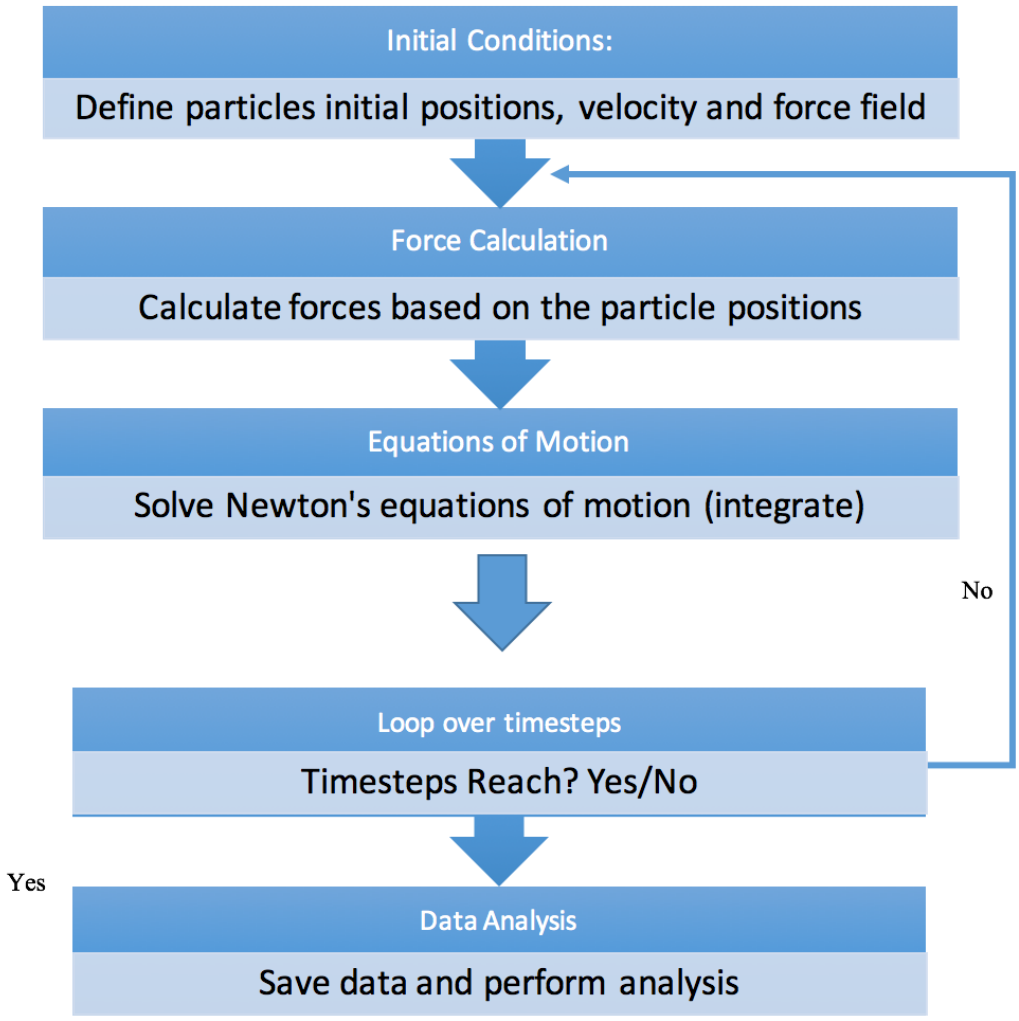

Figure 2.6: Flowchart for Setup and MD Simulation

Computing the force between all N particles is an important stage of the simulation. However, the appropriate time step (Δt) should be selected to obtain accurate subsequent positions and velocities at $t + \Delta t$ from the calculations at t. After evaluating all the forces exerted between the particles, Newton's equations of motion are solved (integrated) using several methods. Algorithms such as the Verlet and the Gear predictor-corrector are commonly used but

Verlet is a more simplified and accurate algorithm [23-25]. Verlet system comprises the basic, leap- frog and the velocity Verlet algorithm [23]. The expression for the position at $t + \Delta t$ is shown through the Verlet algorithm obtained from Taylor series expansion [26]:

$$x_i(t + \Delta t) = x_i(t) + v(t)\,\Delta t + \frac{1}{2}a(t)\,\Delta t^2 \quad 2.7$$

$$x_i(t - \Delta t) = x_i(t) - v(t)\,\Delta t + \frac{1}{2}a(t)\,\Delta t^2 \quad 2.8$$

Adding equations 2.7 and 2.8, one can obtain the appropriate Verlet algorithm for new position

$$x_i(t + \Delta t) = 2x_i(t) - x_i(t-\Delta t) + a(t)\,\Delta t^2 \quad 2.9$$

where x_i is the position of atom i, v (t) is initial velocity (1^{st} derivative with respect to time) and a is the acceleration. Thus, the velocity, v is not required to compute the new position $x_i(t + \Delta t)$ [26]. Since the kinetic energy of the system depends on the velocities of the atoms, it is important to compute it. The velocity Verlet and the leap-frog are exploited to derive it using the mid-step velocity equation [27, 28]. The new velocity from the velocity Verlet scheme is given as:

$$v(t + \Delta t) = v(t) + \frac{1}{2}\{a(t) + a(t+\Delta t)\}\Delta t \quad 2.10$$

The dynamics of molecular or atomic interaction is largely dictated by its interatomic potential. Therefore, the interatomic potential is very important in simulations. However, the interaction model of crystal structure is fitted by different parameters including bond types (ionic, covalent, metallic, van der Waals), bond angle and stiffness, structure (triangular and hexagonal as well as FCC, BCC and SC), neighboring atoms (many-body potential or pair potential) etc [29, 30]. Hence, it is a challenge for a single potential to perfectly depict a system of atoms. There are different functional forms of interatomic potentials to model different types of chemical bond. MD simulation is performed using interatomic potential forms that represent

the applicable properties of concern, and parameters used are selected based of previous research data [30]. One commonly used potential is Lennard-Jones (LJ). Lennard-Jones is a simple but effective model that depicts the interaction of uncharged and non-bonded atoms.

$$V_{LJ} = 4\varepsilon[\left(\frac{\sigma}{r}\right)^{12} - \left(\frac{\sigma}{r}\right)^{6}] \quad 2.11$$

where σ and ε represents the fitting parameters for length and energy scales, r represents the distance between particles. However, many-body systems require many adjustable fitting parameters, hence LJ cannot appropriately describe any real material. Closely related to Lennard Jones are Mie potential which has more fitting parameters, and Morse potential are modeled with respect to central-force system representing distance between particles [30]. These potentials are rarely used because ionic materials cannot be described their functional forms. Terms describing short (repulsive) and long (attractive) range Coulombic interaction are therefore introduced to describe ionic materials in many-body potentials [31]. The Morse potentials are infrequently used but have inspired a class of interatomic potential, bond pair potential used in MD simulations. Brenner potential is an example of bond pair potential while Tersoff is charge-optimized many body potential [32-35].

Tersoff potential is an example of bond order potential and has been used in this study. Jerry Tersoff, proposed a new approach to potential instead of many-body potential [32]. The approach modeled coupling effect of two body and higher number of neighboring atoms correlations. Like Morse potential, it considers the interactions between pairs of atoms, but the Morse potential the interaction strength is modulated by the number of other bonds that the atoms form. Therefore, Tersoff developed bond pair potential which strength depends on the number of atoms in its environment. The general expression representing the energy of an atom in a crystal system by Tersoff bond-order potential is written in the form:

$$E_i = \frac{1}{2} f_c \sum [f_R(r_{ij}) + B_{ij} f_A(r_{ij})], \qquad i \neq j \qquad 2.12$$

where $f_A and\ f_R$ are respectively attraction and repulsion pair potential, r_{ij} is the separation between atoms i and j, f_c is a smooth cutoff function and $B_{ij}$is not a constant but a bond order function (decreased or increased by the presence of other bonds).

2.3.2 Thermodynamics Constraint for MD Simulation

The controlled physical constraints on a system determine the appropriate function for its thermodynamics. Ensembles are an important in molecular dynamics for computing system properties from the law of classical mechanics. Observable macroscopic parameters of a system can be used to describe the different microscopic state using thermodynamic ensembles. Ensemble uses the probability distribution of the states in visual representation comprising of a large number of copies of a system to predict the real state of the bulk system following the principles of classical molecular dynamics [36, 37]. There are three common types of ensembles used with respect to the physical circumstance of the system (isolated and non-isolated):

The Microcanonical Ensemble (NVE): This ensemble is defined for a completely isolated system from its surroundings with both a fixed total energy, E and a fixed number of particles, N. For systems comprising of different types of components, the number of particles of each component is also fixed, and therefore a constant volume system, V. In the imaginary representation of virtual copies of the isolated system, each copy has the same fixed energy, E [39]. Thus, the micro-canonical ensemble can be presented as a single system and used to analyze an isolated system in equilibrium [38, 39]. Since E, N and V are all fixed independent parameters, the appropriate thermodynamic function used for isolated system entropy S (E, V, N). Therefore, at

equilibrium S should also be a single, constant value [39]. Micro-canonical ensemble is not often practical because isolated systems are hardly achieved in reality, and we often need to add or subtract energy that might be evolved during a chemical reaction.

The Canonical Ensemble (NVT): Like the NVE ensemble, canonical ensemble is defined by a fixed number of particles, N and therefore a fixed volume system, V but in contact with a heat source that maintains a controlled temperature T. Thus, there is energy transfer between the heat source and the different virtual copies of the system. The temperature of the heat source is the same fixed temperature, T for all copies. The Helmholtz free energy, F (T, V, N) is the appropriate function to describe a system with variables T, V and N. At equilibrium, the variables of F are constant, therefore F returns a single, stable value at equilibrium [39, 40].

The Isothermal-Isobaric Ensemble (NPT): This ensemble is used to evaluate systems with a fixed number of particles, N and a heat source (thermostat) at constant pressure. In this case, the constant exchange of heat keeps the system temperature constant while maintaining the system pressure by volume with the bariostat [40]. The characteristics thermodynamic function of this ensemble is the Gibbs free energy, G (N, P, T) [41].

2.3.3 Density Functional Theory (DTF) Simulation

Quantum mechanical wave-functions contain enormous information to accurately describe a system of atoms, molecules and condensed phases. Thus, solving the Schrodinger's equation is vital to determine other properties of the electronic states of the system. However, it is impossible to solve the wave-function of a system as described by Schrödinger's equation without assumptions to simplify it. Density functional theory (DFT) is a method that is used to obtain approximate solution of the Schrodinger's equation for many-body (electron) system.

DFT codes are popularly used for electronic structure property calculations of molecules, bulk materials and defects. The equation has been reduced into time-dependent form or time-independent.

2.3.3.1 Time-independent Density Functional Theory

Electron distribution determines the nature and type of bonding in materials and therefore its properties. Calculating the electronic structure is therefore of utmost importance. The energy of electrons in materials is described with the time-independent Schrodinger equation as

$$H\Psi = \left[\dot{T} + \dot{V} + \dot{U}\right]\Psi = \left[\sum_i^N (-\frac{\hbar^2}{2m_i}\nabla_i^2) + \sum_i^N \mathcal{V}(r_i) + \sum_{i<j}^N U(r_{i,}\, r_j)\right]\Psi = \mathbb{E}\Psi \qquad 2.13$$

where $\mathbb{E}$ is the total system energy, T is the kinetic energy, V is the potential, U is the electron interaction energy, Ψ the wave function and $\left[\sum_i^N (-\frac{\hbar^2}{2m_i}\nabla_i^2) + \sum_i^N \mathcal{V}(r_i) + \sum_{i<j}^N U(r_{i,}\, r_j)\right]$ is the Hamiltonian (H).

The electron-electron interaction operator $\dot{U}$ is the same for any system based on the Coulomb interaction,

$$\dot{U} = \sum_{i<j}^N U(r_{i,}\, r_j) = \sum_{i<j}^N \frac{q^2}{|r_i - r_j|} \qquad 2.14$$

Also, the kinetic energy operator $\dot{T}$ is the same for any system of particles under nonrelativistic quantum mechanics. Therefore, for a system of particles whether atoms, molecules or a solid, depends solely on the potential. For a system of atoms, the potential is represented as,

$$\dot{V} = \sum_i^N \mathcal{V}(r_i) = \sum_i \frac{Qq}{|r - R|} \qquad 2.15$$

And Q is the nuclei charges and R is the nuclei positions for all nuclei in the system. The fundamental differences between a spatial nuclei arrangements R, for atoms, molecules and solids are built into DFT. The above assumptions can only solve single-body quantum mechanics.

For many-electron quantum mechanics, DFT uses the relationship between the wave-function, Ψ and electronic density of the system:

$$\rho(r_1) = N \int \ldots \int |\Psi(\boldsymbol{r}^N)|^2 d\boldsymbol{r}_2 \ldots d\boldsymbol{r}_N \quad 2.16$$

Random electron position r_1 and r^N position of all N electrons are presented in the correlation. Therefore, individual wave function is mapped to a unique electronic density function as presented by Kohn and Sham [56].

The concept of density functional theory was first presented in Thomas–Fermi model and then established by Hohenberg–Kohn (H-K) theorems. The first H–K theorems formulated for ground states properties and relates electron density for many-electron system to three spatial coordinates [58, 59]. And by the use of electron density functional simplify n-electrons system comprising three times n-spatial coordinates to just three spatial coordinates. Then, H-K describes the relationship between electron density and the energy functional n-electron system. The energy in terms of density function (from eqn.) can be written as,

$$\mathbb{E}[\rho] = \mathrm{T}[\rho] + \int V(\boldsymbol{r_i})\rho(\boldsymbol{r})d\boldsymbol{r} + U(r_i, r_j)[\rho] \quad 2.17$$

where $U(r_i, r_j)[\rho]$ represents the electron-electron interaction, $\mathrm{T}[\rho]$ is the kinetic energy and the potential term, $V(\boldsymbol{r_i})\rho(\boldsymbol{r})d\boldsymbol{r}$ representing the nuclear-electron interaction.

2.3.3.2 Time-dependent Density Functional Theory (TDDFT).

Unlike time-independent, the time-dependent density functional theory solves the Schrodinger equation using particle position and time. The wave-function is therefore a function of position and time, $\Psi(\mathbf{r}, \mathrm{t})$.

$$i\frac{\partial}{\partial t}\Psi(\mathbf{r}, \mathrm{t}) = H(\boldsymbol{r}, t)\Psi(\mathbf{r}, \mathrm{t}) \quad 2.18$$

where the Hamiltonian H(**r**, t) = $\left[\sum_i^N (-\frac{\hbar^2}{2m_i}\nabla_i^2) + \sum_i^N \mathcal{V}(\boldsymbol{r_i}, t) + \sum_{i<j}^N U(r_i, r_j)\right]$ and only the potential is time dependent in the Hamiltonian [56, 57]. The expression for the TDDFT potential is analogous to the potential for time-independent in equation 2.13, except that it may also have particle- electromagnetic field interaction component, V_{int} (see eqn. 2.19). The total energy in time-dependent DFT is not conserved and thus there is no general minimized as in time-independent, in order to evaluate Schrödinger equation and electronic excited state.

$$\dot{V} = \sum_i^N \mathcal{V}(r_i, t) = \sum_i \frac{Qq}{|r(t)-R|} + V_{int.}(r, t) \quad 2.19$$

Kohn-Sham formulated an approach from an existing Runge-Gross (R-G) theorem but applied it to non-interacting system (to assume zero interaction potential). Thereby simplifying further, the density correlation to potential. However, the assumption of non-interacting requires a new potential, $(\mathcal{V}_s)$ for non-interacting Hamiltonian (U does not affect),

$$H(t) = \left[\dot{T} + \dot{V}\ (t)\right] \quad 2.20$$

to compute the new wave-function (ϕ) based on the sets of n orbitals and represent the Schrodinger equation (equation 2.21) and rewrite the electron density (time-dependent)

$$i\frac{\partial}{\partial t}\ \phi(\mathbf{r}, t) = (-\frac{\hbar^2}{2m_i}\nabla_i^2 + \mathcal{V}_s(\boldsymbol{r}, t))\ \phi(\mathbf{r}, t) \quad 2.21$$

2.3.4 Green-Kubo Relations and Direct Methods

Several approaches have been used to compute thermal conductivity. The Boltzmann transport approach requires the input (lifetimes and mean free path) from other simulations or experiment to compute thermal conductivity. On the other hand, atomistic simulations are effective approach because it based on atomic level scattering and helps to establish the time evolution of system energy and structure behavior. There are two techniques to atomic level simulations: (1) Imposed temperature gradient across the crystal structure is one way to study heat flow and it is referred

to as the non-equilibrium molecular dynamic methods while (2) the equilibrium technique simulates the natural fluctuation dissipation in the system. The Green-Kubo formulation uses the equilibrium molecular dynamics approach and the steady-state non-equilibrium molecular dynamics uses the direct method. The Green-Kubo method correlates thermal conductivity tensor to the heat current tensor for equilibrium fluctuations using the fluctuation dissipation theorem. Thus, for heat flux in direction x, thermal conductivity can be expressed as;

$$k_x = \frac{V}{k_B T^2} \int_0^\infty \langle J_x(t).J_x(0)\rangle \, dt, \qquad 2.22$$

where $J_x(t)$ is x-component of heat current vector at time t and $\langle J_x(t).J_x(0)\rangle$ is the autocorrelation function evaluated at equilibrium while k_B is Boltzmann constant and T is temperature. MD generates the heat current from atomic positions and velocities from which autocorrelation function (ACF) of the heat current is computed. The converged value of the ACF obtained after certain allowed correlation time is inputted for k_x.

The direct method solves Fourier law to predict thermal conductivity from the temperature gradient in a long simulation cell. The heat applied in a certain direction is defined from Fourier's law;

$$q = -\boldsymbol{k} * \nabla T \qquad 2.23$$

It relates temperature gradient, ∇T to heat flux vector, q across the material. The dependence of the direct method on phonon mean free path makes it challenging to converge as thermal conductivity increases with increase size of the simulation cell. Therefore, for direct method adopts linear extrapolation technique in cases where the thermal conductivity does not converge. Table 1.3 below highlights the obvious differences between the GK method and the direct method.

Table 1.3: Comparison of Green-Kubo Method and Direct Method of Thermal Conductivity

	Green-Kubo	**Direct**
Theory	Fluctuation-dissipation theorem	Fourier law
Approach	Equilibrium simulation	Steady-state non-equilibrium simulation
Output	full tensor, applicable to both isotropic and anisotropic materials	One component of k tensor, applicable to isotropic material
Size Effect Length Scale	Phonon wavelength	Phonon mean free path
Challenge	Specifying convergence heat current autocorrelation	Extrapolation to bulk properties

2.4 Thermal Properties of Transition Metal Borides- Zirconium Diborides

As discussed in the introduction, transition metal diborides low density to hardness, strength and melting point ratios are the outstanding proof of mechanical strength and durability. Zirconium diborides (ZrB_2) is classified as an ultra-high temperature ceramic, due to its high melting temperatures (exceeding 3000^oC). Additional choice properties including high wear resistance and chemical inertness have been harnessed in different applications [1,2,4-6]. However, like other materials, ZrB_2 responds to changes in its lattice energy- vibrating atoms. The thermodynamic parameters and changes in the lattices are correlated with associated thermal properties such as thermal conductivity, heat capacity and thermal expansion.

2.4.1 Phonons Thermal Conductivity

Heat flux ($J/s.m^2$) by unit temperature gradient through a material is quantified as its thermal conductivity (W/m.K). Thermal energy travels by conduction, convection and radiation. Radiation transport is by electromagnetic waves and cannot be accurately computed by

molecular dynamics simulation. On the other hand, convection requires fluid media for point-to-point transport of heat. For instance, in a gas, thermal energy is transported through an air gap in a temperature gradient. The molecules from the hot zone accelerate with kinetic energy towards the cooler end and give up the amount of energy. Also, heat transport due to temperature gradient in solids is shown by Fourier's law. However, for electrically non-conducting (dielectric) solids, the lattice vibration energy is proportional to thermal energy. The restrictive interatomic forces cause the atoms to vibrate around their fixed lattice sites, generating elastic waves. Of importance to this thesis, is thermal transport by conduction where lattice vibration (phonons) are the carriers of thermal energy [45].

Therefore, considering the crystalline solid as a box, for experimental purposes, containing a gas of phonons, phonon-phonon scattering are the only interactions in a perfect crystal. In the presence of imperfections, the phonon scattering mechanism changes. Characterizing the scattering mechanism will result in an average distance, mean free path (λ) travelled by the phonon as expressed;

$$\lambda = v_s \tau \qquad 2.23$$

where $\tau \; and \; v_s$ are relaxation time and speed of sound respectively. Note that the relaxation time is the average time between successive scatterings. Considering location x, in the hypothetical box, all atoms at this location would have same average force $\overline{F}$, acting in the positive direction of x^+, will possess energy, $\overline{F}$ (x+ λ) while in the opposite direction (x^-), <F> (x- λ). The total energy across this constant x-plane, can be written as;

$$q = \text{number of phonons} * (\text{energy to } x^- - \text{energy to } x^+) \qquad 2.24$$

but number of phonons, $N_{ph} = \frac{1}{6} n v_s$

thus,

$$q = \frac{1}{6} n v_s \,.\, \overline{F}(x - \lambda) - \frac{1}{6} n v_s . \overline{F}(x + \lambda) \qquad 2.25$$

$$q = \frac{1}{6} n v_s (-2\lambda \,.\, \overline{F}) \qquad 2.26$$

for differential distance dx,

$$q = -\frac{1}{3} n v_s (\lambda \,.\, \overline{F} \left(\frac{dx}{dx}\right)) \qquad 2.27$$

$$q = -\frac{1}{3} n v_s (\lambda \left(\frac{d\overline{E}}{dx}\right)) \qquad 2.28$$

where n represents phonon density, N_{ph} represents number of phonons, $d\overline{E} \approx \overline{F}.dx$ is energy of phonons across dx. Applying separation of variables gives $\frac{\partial \overline{E}}{\partial x} = \frac{\partial \overline{E}}{\partial T}\frac{\partial T}{\partial x} = c_{ph}\frac{\partial T}{\partial x}$, where c_{ph} is specific heat capacity. Therefore, equation 2.28 by substitution becomes

$$q = -\frac{1}{3} n v_s \lambda c_{ph} \frac{\partial T}{\partial x} \qquad 2.29$$

The phonon thermal conductivity is thus written in terms of heat capacity (C_{ph});

$$K_{ph} = \frac{1}{3} n v_s \lambda c_{ph}, \text{ or } \frac{1}{3} C_{ph} v_s \lambda \qquad 2.30$$

2.4.2 Phonon Contribution to Heat Capacity

The heat energy storage capacity of materials is quantified using its heat capacity. It is the reference physical property in most application to determine the energy required to raise the temperature of a material. Phonon heat capacity, C_{ph} is based on available vibrational modes for heat transfer hence related to the lattice vibration energy as discussed in section 2.4.1. Therefore, the heat capacity of solids is defined as $C_{ph} = \frac{\partial \overline{E}}{\partial T}$ (see equation 2.29). But from equipartition the average energy of classical oscillator $\overline{E}$ =Kinetic + Potential = $^1/_2 K_B T + {}^1/_2 K_B T = K_B T$

For a particle in 2-dimensional space, there are two degrees of freedom. Hence $\overline{E}$ for a 2D crystalline solid with N atoms is defined as $\overline{E} = 2NK_BT$, the heat capacity is obtained to be

$C_{ph} = 2NK_B$, and for 3D crystal $C_{ph} = 3NK_B$. Where T refers to temperature and K_B Boltzmann constant. The formulation of phonon heat capacity corresponds to the Dulong-Petit assertion (Fig. 2.7), that at the point of maximum lattice vibration, heat capacity become independent of temperature. The classical approach was unable to accurately quantify heat capacity at low temperatures. Einstein predictions of heat capacity through quantum mechanics by assigning vibrational frequencies to the vibrations of crystal particles is representative of the data from recent experiments. However, near absolute zero temperatures, Einstein's model failed and was modified by Debye's theory. The theory modified Einstein's same frequency approach to a range of frequencies with a maximum cutoff frequency (ω_D). At $\omega > \omega_D$, no normal modes are available.

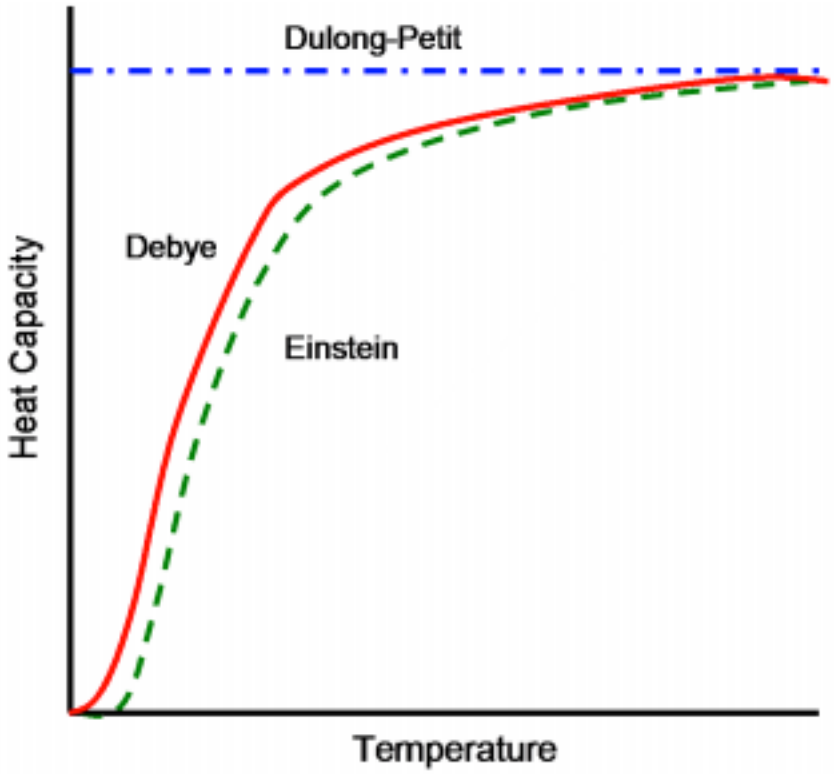

Fig. 2.7: Three Models of Heat Capacity, Dulong-Petit (blue), Debye(red) and Einstein(green)

The number of states with the same specific vibrational frequencies demonstrates the intensity as that vibration mode. Heat capacity depends on the phonon Density of States (DOS) following 2.31. The phonon DOS can be obtained from the phonon dispersion relations discussed in section 2.3.3. The Einstein and Debye models for the specific heat presented in equations 2.32 and 2.33 can be considered to differ only in the approximate form that they use for the DOS.

$$\overline{E} = \int_0^{\infty} (\text{energy})\,(\text{occupation function})(\text{DOS}) \tag{2.31}$$

$$C_E = 3N_A k_B \frac{h\omega}{k_B T} \frac{e^{\frac{h\omega}{k_B T}}}{(e^{\frac{h\omega}{k_B T}} - 1)} \tag{2.32}$$

$$C_D = 9N_A k_B \frac{T}{T_D} \int_0^{\frac{T_D}{T}} \frac{x^4 e^{-x}}{(1-e^{-x})^2} dx \tag{2.33}$$

Debye's approximation assumes that a lower temperature primarily elastic waves of long wavelengths are excited. Where k_B is Boltzmann's constant, ω is the vibration frequency, h is Planck's constant, N_A is Avogadro's number, T is temperature and T_D Debye temperature. Finding the defect offset for heat capacity of zirconium diboride is a property enhancement that is yet to be investigated.

2.4.3 Thermal Expansion Coefficient

The volume change in a material that accompanies a change in temperature is a distinctive property since crystalline solids have different melting points and bonding properties. The coefficient of expansion or contraction predetermines choice materials for specific applications particularly around expansion joints. For crystalline solids, the fractional change in dimensions with temperature can be calculated along length, plane or volume. As most designs are macroscopic and three-dimensional, it is practical therefore to compute coefficient of thermal expansion (CTE) which is commonly the volumetric thermal expansion of solids materials. The energy level of lattice thermal vibration is related to the bond potential well. With increasing temperature (the bond energy) the larger amplitude vibrations sample more of the softer tail of the potential. Fig. 2.8 shows the maximum ionic distance displaced with increased temperature(larger amplitude lattice vibration). Transition metal diborides with high melting values and strong bonds will therefore have high elastic properties and stiffness.

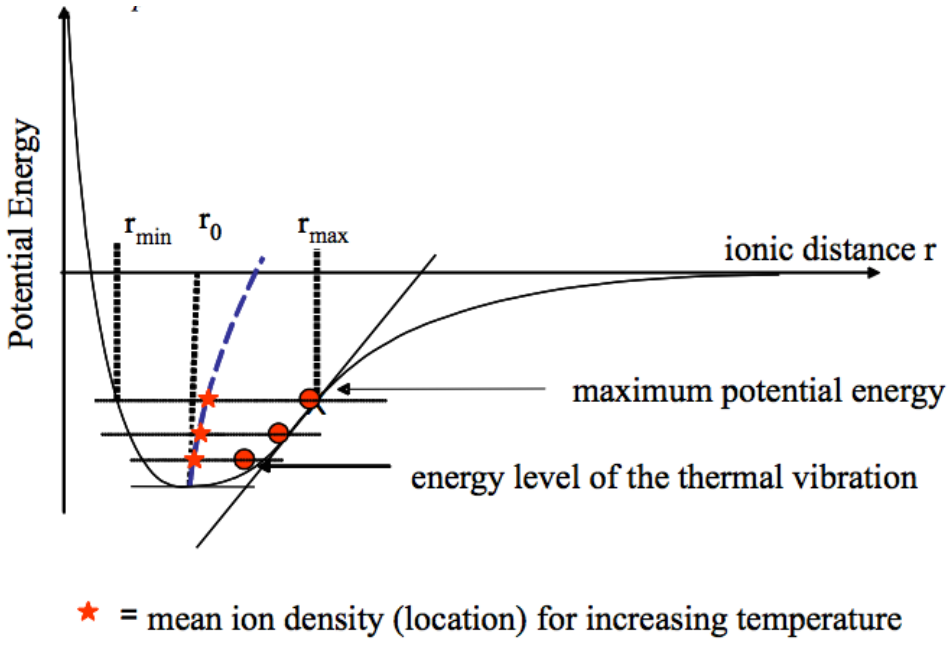

Fig. 2.8: Potential- Ionic Distance Curve denoting energy correlation to ionic radius and expansivity around the potential well [63]

It is therefore evident that lattice dynamics and lattice energy can be used to formulate the expansion coefficient in solids. Output for molecular dynamic simulations are used to calculate this parameter. The volumetric thermal expansion coefficient (γ) at negligible pressure can be expressed as;

$$\gamma = \frac{1}{\mathrm{V}} \frac{\mathrm{dV}}{\mathrm{dT}} \qquad 2.34$$

The fractional (relative) change in volume dV/dT is also very important for micro changes in volume with temperature, where instantaneous CTE values does not change. Percent elongation indicating phase transformation (bond angle changes or spatial dependency) with temperature can be identified [63]. Fig. 2.9 shows thermal expansion of different solids. Fig. 2.9(right) attributes increased covalent bonding with low expansion coefficient while the metal and ionic bonding solids showing high coefficient of expansion, corresponding to strong bond with high elasticity (stiffness).

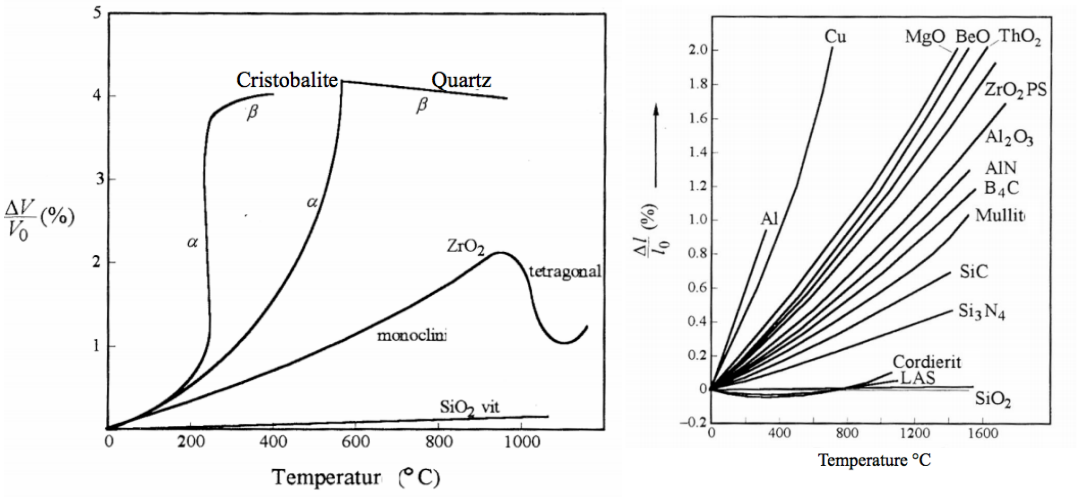

Fig.2.9: Thermal expansion of solids in volume fraction (left), spatial direction (right) [63]

Some solids exhibit non-symmetric expansion also known as anisotropy in expansivity in certain directions (x, y or z). This can not only be observed in the curvature of the potential well

but also through calculations of the 1-dimensional (linear) expansion coefficient. Similar to equation 2.31, linear coefficient of thermal expansion, α in any one-direction can be obtain from;

$$\alpha = \frac{1}{\mathrm{L}} \frac{\mathrm{dL}}{\mathrm{dT}} \qquad 2.35$$

Zirconium diboride is high melting temperature ceramics with iono-covalent bond, strong bonds and high lattice stiffness. ZrB_2 also reportedly exhibits anisotropy in the c-place and hence variations in the lattice parameters with temperature are quantified in this study [50].

2.5 Phonon Scattering and Mathieson's Rule

Thermal resistance in solids is determined by the several scattering mechanisms. Inclusions in solids such as impurities, point defects, boundaries and carrier interactions (phonon-phonon or electron-phonon) vary the scattering mechanisms from perfect crystal lattice. Mathieson's rule where applicable estimates total contributions thermal resistance from all the independent scattering variables. Generally, the total rate of scattering being the sum of all the rate from each type of active independent scattering mechanism. The additive resistance from lattice vibration and impurities scattering are depicted in Fig 3.0 and the total factor by virtue of Mathieson's rule can be expressed as;

$$\mathrm{r_{tot}} = \mathrm{r_{normal}} + \mathrm{r_{impurity}} \qquad 2.36$$

Scattering resulting from lattice vibration is expected even in perfect crystals, therefore impurity induced resistance can be calculated knowing the combined. Thermal resistance, r inversely proportional to thermal conductivity, k, the expression can be presented in terms of k and

equation 2.36 can therefore be written as a function of scattering time which is an important phonon property.

$$\frac{1}{\tau_{tot}} = \frac{1}{\tau_{normal}} + \frac{1}{\tau_{impurity}} \qquad 2.37$$

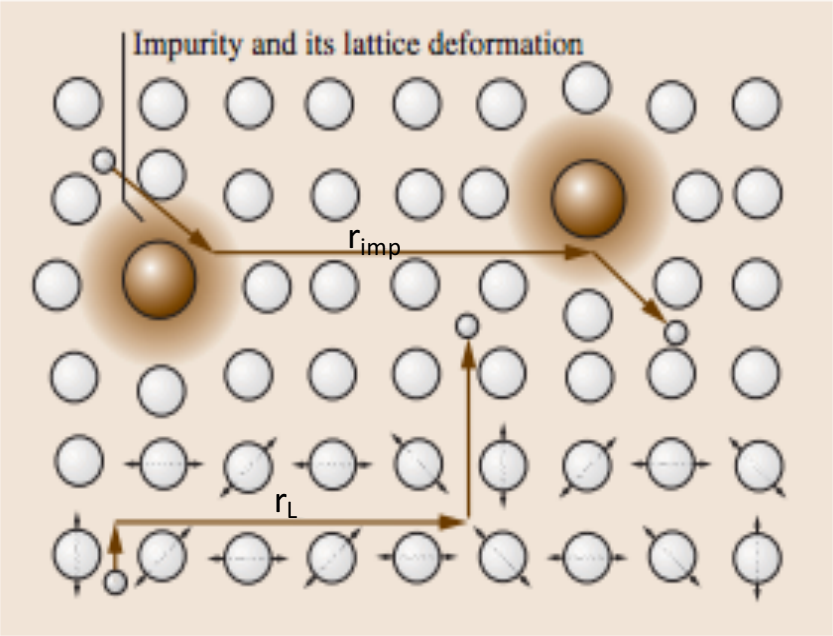

Fig. 3.0: Shows scattering time from lattice vibration (normal phonon-phonon), r_L and from impurity, r_{imp}[70]

REFERENCES

[1] Bansal, Narottam P., ed. *Handbook of Ceramic Composites*. Springer. p. 192 (2004).

[2] Salute, Joan; et al. (2001). *SHARP-B 2: Flight Test Objectives, Project Implementation and Initial Results*. 2nd Annual Conference on Composites, Materials and Structures, Cocoa Beach, FL, United States.

[3] Agarwal, D. C., and U. Brill, "Material Degradation Problems in High Temperature Environments," *Industrial Heating,* p. 56 (Oct. 1994).

[4] A. Jankowiak, J.F. Justin. Ultra-High Temperature Ceramics for aerospace applications. *ODAS 2014*, Jun 2014, COLOGNE, Germany. <hal-01103216v2>

[5] Sylvia M. Johnson. Ultra-High Temperature Ceramics: Applications, Issues and Prospects. NASA-Ames Research Center. 2nd Ceramic Leadership Summit Baltimore, MD. August 3, 2011

[6] A. Barua, Md. S. Hossain, K.I. Masood, S. Subrina. Thermal Management in 3-D Integrated Circuits with Graphene Heat Spreaders. International Conference on Solid State Devices and Materials Science, Physics Procedia. Volume 25, 2012, Pg 311–316

[7] D.G. Cahill and R.O. Pohl, Annu. Rev. Phys. Chem. 39,93 (1988)

[8] Bijaya Kumar Sahoo. (2011). Effect of Piezoelectric Polarization on Phonon group velocity in Wurtzite Nitrides. Condensed Matter, Material Science. arXiv:1108.2770v2.

[9] Balandin A A 2000 *Phys. Low-Dim. Structures* **5-6** 73; 2005 *J. Nanoscience Nanotech.* **5** 1015

[10] Fahrenholtz W. G. and Hilmas G. E. 2004 NSF-AFOSR Joint Workshop on Future Ultra-High Temperature Materials (NSF, Arlington, VA 22230).

[11] Wangsheng Chu[a, b], Ziyu Wu, Wenhan Liu, N.L. Saini[c], A. Bianconi[c], Tiandou Hu[b], Yaning Xie. Lattice dynamics study of AlB2-type 4d transition-metal diborides by extended X-ray-absorption fine structure. Radiation Physics and Chemistry. Volume 127, (October 2016) .

[12] Hyoung Joon Choi*, David Roundy*†, Hong Sun*, Marvin L. Cohen*† & Steven G. Louie. The origin of the anomalous superconducting properties of MgB2. Nature. Vol 418 (2002)

[13] J. W. Zimmermann, G. E. Hilmas, and W. G. Fahrenholtz, "Thermophysical Properties of ZrB_2 and ZrB_2-SiC Ceramics," *Journal of the American Ceramic Society,* **91**[5] 1405-11 (2008).

[14] J. M. Ziman, Electrons and Phonons. Oxford, Oxford, 2001.

[15] G. P. Srivastava, The Physics of Phonons. Adam Hilger, Bristol (1990).

[16] Fariborz Kargar, Sylvester Ramirez, Bishwajit Debnath, Hoda Malekpour, Roger K. Lake and Alexander A. Balandin. Acoustic phonon spectrum and thermal transport in nanoporous alumina arrays. Appl. Phys. Lett. 107, 171904 (2015).

[17] C. Kittel, Introduction to Solid State Physics, Danvers, MA: John Wiley and Sons, Inc., 1996.

[18] T. Wang, "Sub-Micron Thermal Transport in Ultra-Scaled Metal Oxide Semiconductor(MOS) Devices," PhD Thesis, School of Mechanical Engineering, Purdue University, West Lafayette, 2007.

[19] Aleksandr Chernatynskiy, David R. Clarke, and Simon R. Phillpot, "Thermal Transport in Nanostructured Materials," in *Handbook of Nanoscience, Engineering and Technology*, W. A. Goddard III, D. W. Brenner, S. E. Lyshevski and G. J. Iafrate, Eds., Boca Raton, CRC Press,

2002, pp. 545-572.

[20] Strogatz, Steven (2007). "The End of Insight". In Brockman, John. What is your dangerous idea? HarperCollins. ISBN 9780061214950

[21] Tuckerman ME, Berne BJ, Martyna GJ; Berne; Martyna (1991). "Molecular dynamics algorithm for multiple time scales: systems with long range forces". J Chem Phys. 94 (10): 6811–6815. Bibcode:1991JChPh..94.6811T. doi:10.1063/1.460259. Jump up

[22] Tuckerman ME, Berne BJ, Martyna GJ; Berne; Martyna (1992). "Reversible multiple time scale molecular dynamics". J Chem Phys. 97 (3): 1990–2001. Bibcode:1992JChPh..97.1990T. doi:10.1063/1.463137.

[23] 49] M.P. Allen and D.J. Tildesley. Computer Simulation of Liquids. Oxford University Press, USA, 1991. ISBN 0198556454.

[24] Loup Verlet. Computer" experiments" on classical fluids. i. thermodynamical properties of lennard-jones molecules. Physical review, 159(1):98, 1967.

[25] Loup Verlet. Computer" experiments" on classical fluids. ii. equilibrium correlation functions. Physical Review, 165(1):201, 1968.

[26] D. Frenkel and B. Smit. Understanding Molecular Simulation, Second Edition: From Algorithms to Applications. Academic Press, 2 edition, November 2001. ISBN 0122673514.

[27] Parviz Moin. Engineering numerical analysis, 2001.

[28] R. P. Feynman, R. B. Leighton and M. Sands, The Feynman Lectures on Physics, Vol. 1, Addison-Wesley, 1963, Chapter 9 (``Newton's Laws of Dynamics").

[29] Murray S. D., John W. L., and Charles W. B. Interatomic potentials for Zirconium Diboride and Hafnium Diboride. Computational Material Science 50 (2011) 2828-2835.

[30] Jaro Meller et al. Molecular dynamics. eLS, 2001.

[31] B. P. Feuston and S. H. Garofalini. Empirical three-body potential for vitreous silica. J. Chem. Phys., 89(9):5818, 1988.

[32] J. Tersoff, Phys. Rev. B 37, 6991 (1988).

[33] Adri CT Van Duin, Siddharth Dasgupta, Francois Lorant, and William A Goddard. Reaxff: a reactive force field for hydrocarbons. The Journal of Physical Chemistry A, 105(41):9396–9409, 2001.

[34] Tzu-Ray Shan, Bryce D. Devine, Travis W. Kemper, Susan B. Sinnott, Simon R. Phillip. Charge-optimized many-body potential for the hafnium/hafnium oxide system. Physical Review B, 81(12):125328, 2010.

[35] Donald W Brenner. Empirical potential for hydrocarbons for use in simulating the chemical

vapor deposition of diamond films. Physical Review B, 42(15):9458, 1990.

[36] Landau, L.D.; Lifshitz, E.M. (1980). Statistical Physics. Pergamon Press. pp. 9 ff. ISBN 0-08-023038-5.

[37] D.C. Rapaport. The Art of Molecular Dynamics Simulation. Cambridge University Press, 2 edition, April 2004. ISBN 0521825687.

[38] Roland Stote etc. Theory of molecular dynamics simulations, October 1999. URL http://www.ch.embnet.org/MD_tutorial/pages/MD.Part1.html. (accessed January 22nd, 2019)

[39] Henry R. Glyde. Statistical Mechanics and Thermodynamics. Spring 2010 http://www.physics.udel.edu/~glyde/PHYS813/Lectures/chapter_6.pdf (accessed November 14th, 2018)

[40] W. Cai. Introduction to statistical mechanics. March 2012. URL http://micro. stanford.edu/~caiwei/me334/ME346A_Lecture_Notes_Win2012.pdf.

[41] Dill, Ken A.; Bromberg, Sarina; Stigter, Dirk (2003). Molecular Driving Forces. New York: Garland Science.

[42] Melville S. Green. Markoff random processes and the statistical mechanics of time dependent phenomena. ii. irreversible processes in fluids. The Journal of Chemical Physics, 22(3), 1954.

[43] Rajiv Asthana; Ashok Kumar; Narendra B. Dahotre (9 January 2006). Materials Processing and Manufacturing Science. Butterworth–Heinemann. pp. 158–. ISBN 978-0-08-046488-6. Retrieved 7 May 2013.

[44] D. A. McQuarrie, Statistical Mechanics. University Science Books, Sausalito (2000) 520-521.

[45] Vijaya & Rangarajan and Gopala Rangarajan. Materials Science. Tata McGraw- Hill Education, February 2004. ISBN 0070534691.

[46] H. Kaburaki, J. Li, S. Yip, and H. Kimizuka, J. Applied Physics 102,043514 (2007)

[47] J. W. Lawson, M. S. Dawson and C. W. Bauschlicher, Jr. Lattice thermal conductivity of ultra-high temperature ceramics ZrB_2 and HfB_2 from atomistic simulation. Journal of Applied Physics, 110, 083507 (2011).

[48] Laura de Sousa Oliveira, P. Alex Greaney. Thermal resistance from irradiation defects in graphite. Computational Materials Science 103 (2015) 68–76

[49] D. P. Sellan, E. S. Landry, J. E. Turney, A. J. H. McGaughey, and C. H. Amon. Size effects in molecular dynamics thermal conductivity predictions. Phys. Rev. B 81, 214305 – Published 21 June 2010

[50] William A. Paxton, Tevfik E. Özdemir, İlyas Şavklıyıldız, Terence Whalen, Hülya Biçer, Enver Koray Akdoğan, Zhong Zhong, and Thomas Tsakalakos. Anisotropic Thermal Expansion of Zirconium Diboride: An Energy-Dispersive X-Ray Diffraction Study. Journal of Ceramics Volume 2016 (2016), Article ID 8346563

[51] McClane, Devon Lee, "Thermal properties of zirconium diboride - transition metal boride solid solutions" (2014). Theses. Paper 7265.

[52] H. Kinoshita, S. Otani, S. Kamiyama, H. Amano, I. Akasaki, J. Suda and H. Matsunami. Zirconium Diboride (0001) as an Electrically Conductive Lattice-Matched Substrate for Gallium Nitride. Japanese Journal of Applied Physics, Volume 40, Part 2, Number 12A.

[53] J. W. Zimmermann, G. E. Hilmas, W. G. Fahrenholtz, R. B. Dinwiddie, W. D. Porter, and H. Wang. Journal of the American Society. Vol. 91, 1405 (2008)

[54] Zhang, D. A. Pejaković, J. Marschall, and M. Gasch, "Thermal and Electrical Transport Properties of Spark Plasma-Sintered HfB2 and ZrB2 Ceramics," Journal of the American Ceramic Society, 94[8] 2562-70 (2011).

[55] John J. Chu, Craig A. Steeves. Thermal expansion and recrystallization of amorphous Al and Ti: A molecular dynamics study. Journal of Non-Crystalline Solids 357 (2011) 3765–3773

[56] W. Kohn and L. J. Sham. Self-consistent equations including exchange and correlation effects. Phys. Rev., 140:A1133–A1138, Nov 1965.

[57] Miguel AL Marques and EKU Gross. Time-dependent density functional theory. Annual Review of Physical Chemistry, 55(1):427–455, 2004.

[58] Hohenberg, Pierre; Walter Kohn (1964). "Inhomogeneous electron gas". Physical Review. 136 (3B): B864–B871

[59] Levy, Mel (1979). "Universal variational functionals of electron densities, first-order density matrices, and natural spin-orbitals and solution of the v-representability problem". Proceedings of the National Academy of Sciences. United States National Academy of Sciences. 76 (12): 6062–6065.

[60] [Goodson and Flik, 1992] Goodson, K. and Flik (1992). Microscale phonon transport in dielectrics and intrinsic semiconductors. HTD - Fundamental issues in small scale heat transfer - ASME, 227:29–36.

[61] [Majumdar, 1993] Majumdar, A. (1993). Microscale heat conduction in dielectric thin films. Journal of Heat Transfer, 115:7 – 16.

[62] Zhigilei, 2002] Zhigilei, L. V. (2002). Mse 524: Modeling in materials science. Website. http://www.people.virginia.edu/\~lz2n/mse524/.

[63] F. Filser & L.J. Gauckler. (2007). Ceramic Materials, Chapter 3: Bond Energy and Properties ETH-Zürich, Departement Materials.

[64] Richard Lesar. Introduction to Computational Materials Science: Fundamentals to Applications. 1st Edition.

[65] Ronald Loehman, Erica Corral, Hans Peter Dumm, Paul Kotula, and Rajan Tandon. Ultra-High Temperature Ceramics for Hypersonic Vehicle Applications. Sandia National Laboratories. SAND 2006-2925

[66] S. Guo, T. Nishimura, and Y. Kagawa, "Preparation of Zirconium diboride ceramics by reactive spark plasma sintering of zirconium hydride-boron powders," Scripta Materialia, 65 1018-21 (2011).

[67] Zhang, S. C; Hilmas, G. E; Fahrenholtz, W. G (2006). "Pressureless Densification of Zirconium Diboride with Boron Carbide Additions". Journal of the American Ceramic Society. 89 (5): 1544–50.

[68] J. W. Zimmermann, G. E. Hilmas, and W. G. Fahrenholtz, "Thermophysical Properties of ZrB2 and ZrB2-SiC Ceramics," *Journal of the American Ceramic Society,* 91[5] 1405-11 (2008).

[69] M. J. Thompson. Densification and Thermal Properties of Zirconium Diboride based Ceramics. Materials Science and Engineering. Missouri University of Science and Technology (2012).

[70] Kasap S., Koughia C., Ruda H.E. Electrical Conduction in Metals and Semiconductors. In: Kasap S., Capper P. (eds) Springer Handbook of Electronic and Photonic Materials. Springer Handbooks. Springer, Cham (2017)

PAPER

3. Thermal Conductivity of ZrB_2 from Equilibrium Molecular Dynamics Simulations and the Impact of Point Defects

Jude O. Ighere*, Laura de Sousa Oliveira and P. Alex Greaney

Abstract

Transition metal diborides are considered choice materials for thermal applications for its high melting temperatures and shock resistance. ZrB_2 and HfB_2 are found to be advantageous. In here is presented molecular dynamic simulations performed to obtain thermal conductivity using the Green-Kubo method for various point defects (vacancy, interstitials, isotopic). Tersoff potentials are used for atomic interactions and thermal conductivity computed for defective and defect-free ZrB_2. The thermal resistance correlation to number of defects were explored. The simulated structure with point defects are presented. Computed thermal conductivity values showed that interstitial defects are detrimental to thermal transport in ZrB_2 unlike vacancies. The defect formation energies were also investigated. The computed results are comparable to available experimental data and are presented to further the knowledge on ZrB_2 based materials.

Introduction

Understanding the relationship between atomic-level correlation to macroscale prediction of thermal properties is essential for designs in new generation technologies including sharp leading edge hypersonic aircraft as well as complex integrated circuits and advanced nuclear plants [1-5]. As an ultra-high temperature ceramics (UHTC) with melting point of about 3240^{o}C, ZrB_2 is a favorable candidate for advanced thermal engineering. Based on its high thermal conductivity coupled with high melting point, this material offers the possibility of high thermal re-radiation from high temperature regions. Recent data have shown that small changes in the

impurity content of ZrB_2-based ceramic resulted in significant thermal conductivity changes [6, 7]. This property combined with its high strength and chemical inertness has been harnessed in different applications including thermal conductivity prediction by intrinsic phonons [18]. Even though ZrB_2 is a conductor, studies have shown that its heat transport mechanism is dominated by phonons [16,18, 23]. It is essential to develop a structure-property multi-correlation for ZrB_2 materials. In this article, we predict thermal conductivity changes in theoretical materials in which defects dominate phonon scattering lifetimes. This has been done by modeling thermal transport using the Boltzmann transport equation in which the mean free paths of phonons are modeled as a function of wave vector and polarization, and how these scattering processes interact with the extreme anisotropy of the $ZrBr_2$ crystal structure. To this end, in this work we use a combination of classical molecular dynamics and Boltzmann transport theory to: (1) characterize the intrinsic thermal transport in ZrB_2, (2) compute structures and energies of point defects in ZrB_2, (3) Compute the thermal conductivity and phonon lifetimes in defected ZrB2 and finally (4) Quantify the phonon scattering cross-section of defects to phonons of different wave.

The impact of imperfection on the thermal conductivity of transition metal diboride reported in recent articles presents interesting challenge on defect adaptive thermal properties [22, 25, 26]. Other researchers have reported varying thermal conductivity values for zirconium diboride ranging from 56 W/(mK) to about 133 W(mK) at room temperatures. However, the source of disparities in the thermal properties of zirconium diboride remain unclear [6, 22, 25-27]. One could propose that imperfections and impurities in structure based on processing technique of ZrB_2 and different sources of component elements play a role. There are enormous

amounts of defect types to investigate in a bid to harness thermal properties of ZrB_2, however in this paper point defects are the focus.

Bonding and Lattice Structure

ZrB_2 belong to the family of hexagonal isostructural transition metal diborides (TMB_2) with a AlB_2-type 4d crystal structure with space group P6/mmm [8]. The structure is a repeating layer of boron atoms with the zirconium atoms arranged in an alternating hexagonally closed packed layer. The unusual properties of this material have been attributed to its multi-bonding types in the structure. The boron-layered structure is similar to the hexagonal planes of carbon atoms in graphite but unlike carbon, boron atom only has three valence electrons. Like carbon atom in graphite, boron bonds to its nearest neighbor boron atoms to form strong σ-bond within the planes and weak π-bond between planes. Thus, since there are only three valence electrons available in a boron atom, some of the σ-bonds are not filled. Therefore, researchers have attributed the characteristic stiffness of ZrB_2 lattice structure to the strong boron-boron covalent bonds and the thermal conductivities to the metallic bonds [10]. This disparity in stiffness of the different bond types along with the large mass difference between B and Zr creates distinct bands of high and low frequency lattice vibrations [9].

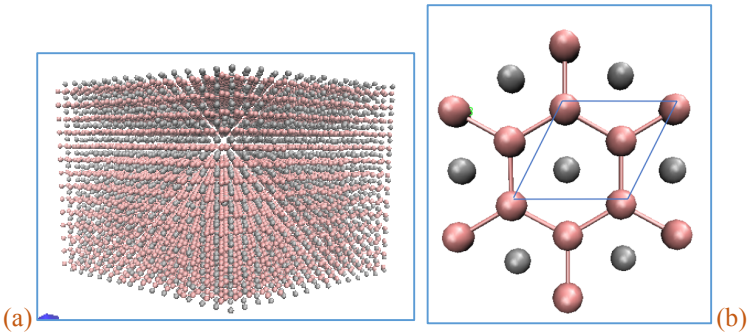

Fig. 1.1: Zirconium diboride lattice structure, showing (a) alternating stack of Zr and B and (b) hexagonal structure with unit cell

To develop an atomistic understanding of defect impacts (types and concentrations) on the

thermal properties, an optimized structure of perfect ZrB_2 was first obtained as in Fig. 1.1. On the left (see Fig. 1.1a) is the stack of alternating layers of individual species in the hexagonal structure while Fig. 1.1b shows a slice of the structure with unit cell. The non-clustered atoms demonstrate position integrity of each atom type in the lattice. The within layer Zr-Zr metallic bond is visually depicted without bond lines while the B-B within layer bond stiffness with thick lines, represents the strong sigma bond.

Characterizing Defect Structures

Three groups of defects have been considered in this study: vacancies, interstitials and isotopic defects. Fig. 2.1a-b show the nature of the resulting point defects, non-clustering out-of-plane Zr-interstitial, clustering in-plane B-interstitial. Zr interstitial (see fig. a and b) pulls adjacent Zr atoms creating a pseudo-cluster of defect. Zr vacancy (see fig. c and d) in the crystal lattice creates an in-plane atomic size void. While B interstitial deforms the B-B hexagonal structure without intra-plane interaction (fig. e and f). Like Zr, boron vacancy maintains structural integrity while creating atomic size void (fig. g and h). ZrB_2 stiffness attributed to the B-B within layer bond strength is visible in its lattice point integrity [27]. Boron interstitials form monolayer bond with nearest atoms without protruding clusters unlike the zirconium interstitial clusters which form interlayer bonding. Boron-11 and zirconium-97 were used for the isotopic defects in the lattice structure. All defects were introduced by first generating a 6x6x9 unit cell dimension in LAMMPS with periodic boundaries in all directions. The structure was the relaxed and energy of the system computed. Point defects were introduced and the structure was relaxed again using energy minimization before computing new energy of the system. In the case of interstitial defects, structure was further annealed to obtain lowest energy configurations.

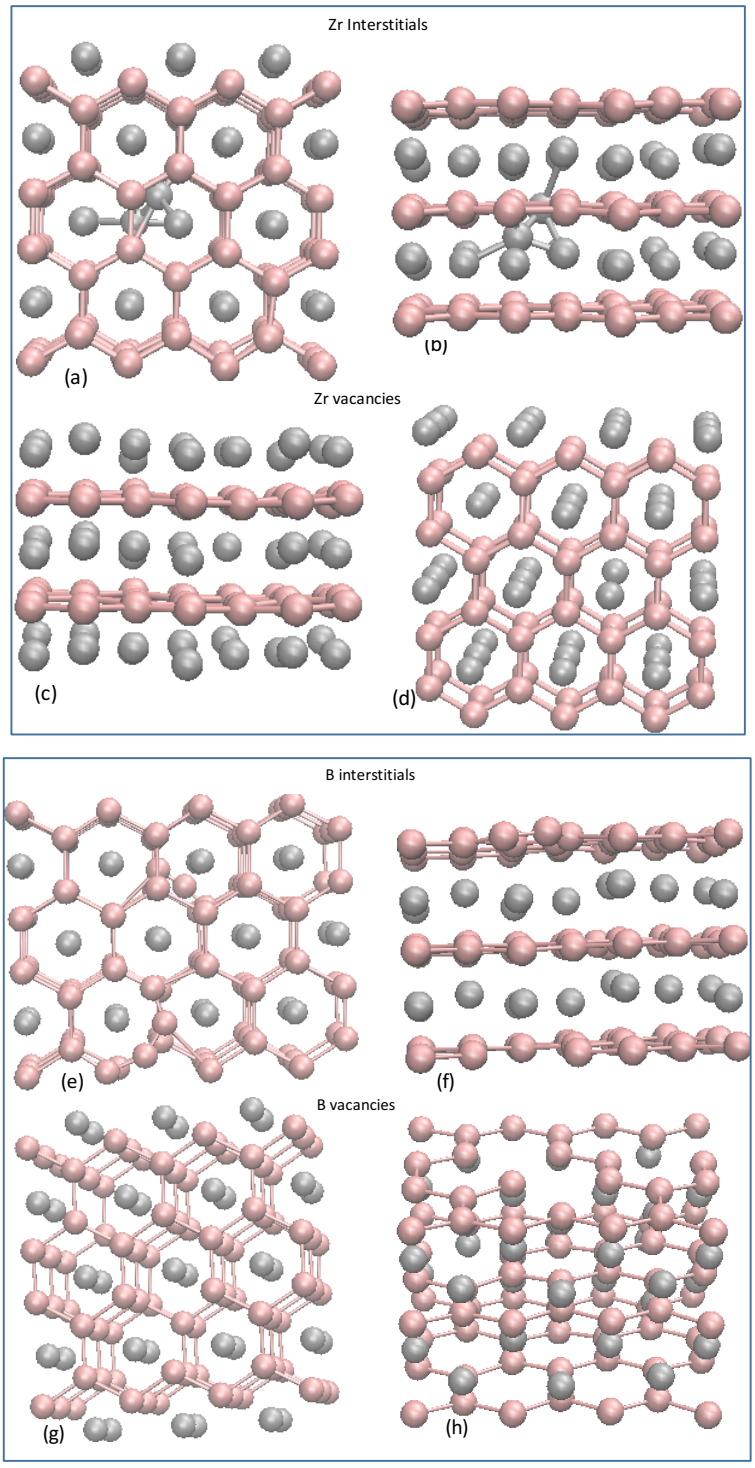

Fig. 2.1 Depiction of the defects computed in this work: (a-b) Zr interstitial and (c-d) Zr vacancy while (e-f) B interstitial and (g-h) B vacancy.

Each defect type was created and then annealed by heating to 900K and then cooling slowly to 300K over 5psi before quenching and relaxing the structure. The energy of each defect was

computed and the hessian matrix of the atoms in the vicinity of the defect computed. The computed change in cohesive energy of the system was used to calculated the energy of defect formation. The defect formation energies were used to justify the likelihood of formation of specific defects type. The energy attributed to the defect was calculated by

$$E_d = (E_D + E_R) - \frac{N_D}{N_o} E_o \qquad (1)$$

where E_D *and* E_o represents the final energy of the defective and defect-free ZrB_2 crystal system while N_D *and* $N_o$represents the number of atoms in the defective and defect-free ZrB_2 crystal system respectively. Fig. 2.2 presents the energy values for the various defects types considered. A study by Martin et al shows that it cost energy to create vacancies for Ti and Zr due to increased valence electron unlike Nb and Mo. [29]. Other studies only consider the enthalpy of formation of ZrB_2 including entropy of the system. The point defect creation and structural optimization to obtain energetically stable configuration is depicted in the schematic in Fig 2.2. Structures containing vacancies were not annealed, to minimize vacancy mobility from predetermined sites. It could be stated that structural stiffness of ZrB_2 crystal is noticeable from the positive energy of interstitial and vacancy defect formation increased with the number of defects. Fig. 2.1(a-h) depicted that the atomic sites of Zr in the lattice are non-deviating, thereby forcing the interstitial atoms to out of the Zr-Zr plain (intra-layer).

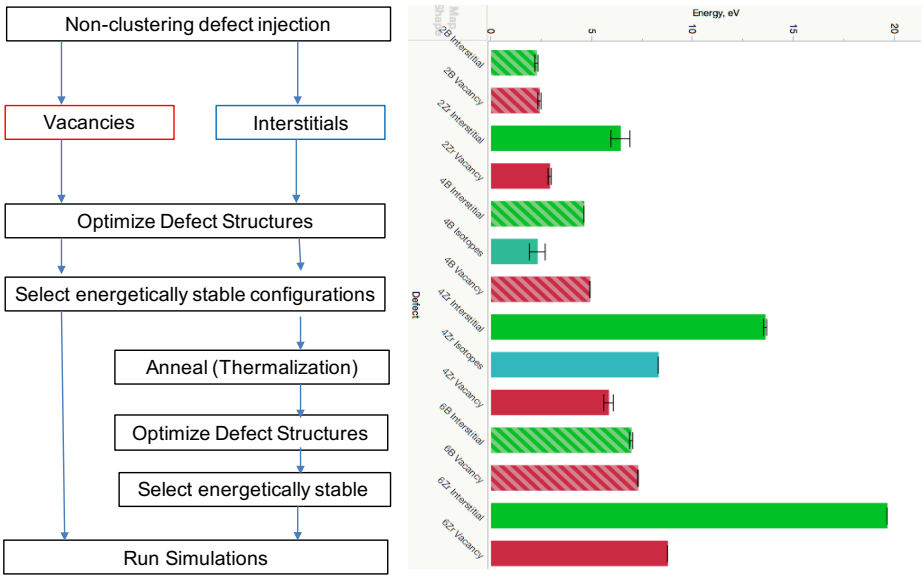

Fig 2.2 (left)Schematic of defect injection technique and (right) corresponding energies for interstitials, vacancies and isotopic defects. The interstitials and vacancies are shown in Fig. 2.1.

Calculation of Thermal Conductivity

Lattice thermal conductivity is the elastic effect of its vibration (phonons). There are two atomistic techniques that have been established and commonly used to compute the thermal conductivity of materials using MD simulations. These are Green-Kubo Method (an equilibrium method) and simulation of heat transport under an imposed temperature gradient (non-equilibrium method). The heat current autocorrelation function shows fluctuation about zero at equilibrium and therefore Green-Kubo method computes thermal conductivity based on the time it takes for the fluctuations to dissipate quantified by computing the integral of the heat current autocorrelation function. [11, 12]. It is given by [13]

$$\kappa = \frac{V}{k_B T^2} \int_0^\infty \mathbf{J}(t).\mathbf{J}(t+\tau)\, d\tau, \qquad 2.2$$

where $\boldsymbol{J}(t).\boldsymbol{J}(t+\tau)$ is termed the heat autocorrelation function, **J** is the heat current vector, V denotes the system volume, k_B is Boltzmann constant, and T is the system temperature. Green Kubo (GK) Theorem has been used extensively in studying the thermal conductivity of solid

materials but very limited analysis on zirconium diboride and its family of anisotropic ceramics. The GK method connects the integration of the ensemble average of the heat current correlation function to the lattice thermal conductivity tensor κ_{ij}.

$$\kappa_{ij} = \frac{V}{k_B T^2} \int_0^\infty J_i(0).J_j(\tau)d\tau, \qquad 2.3$$

where V is the system volume, k_B is Boltzmann constant, i, j = x, y, z, and T is the system temperature. The heat current vector can be calculated at time t, from the spatial configuration $\boldsymbol{J}(t) = \frac{1}{V}\left[\sum_i e_i v_i + \sum_{i<j}(f_{ij}.v_j)x_{ij}\right]$ where i and j represent atom i and neighbor j, $v_j$is the velocity of atom i, e_i is the per atom energy of atom i, f_{ij} is the force on atom i due to atom j and x_{ij} is the vector from x_i to x_j. Kaburaki et al. showed that the accuracy of the Green-Kubo method largely depends on the interatomic potential used for its implementation [46]. In order to simulate ZrB_2 using molecular dynamics, the proper super cell and interatomic potential is required. Murray et al. have used Tersoff interatomic potentials for modeling Zr, Hf, and B properties and demonstrated repeatability [29]. These potentials have been reported to be stable across multiple test for different properties of these diborides [5, 13, 47]. In our study, we have adopted this well-defined potential to investigate the thermal properties of perfect ZrB_2 lattice structure and some point defects.

Following Daw et al., simulation for perfect ZrB_2 was performed with 6 x 6 x 9 supercells for the prediction of thermal conductivity, k [16]. In this study, however, initial gross analysis simulations were performed at 300K using different super cell sizes to predetermine optimal thermal conductivity values along the axial directions computed for perfect ZrB_2. LAMMPS code were used to perform the MD simulation. The optimal 6 x 6 x 9 supercell boxes were created and simulated. The system was simulated in NPT ensemble to sweep average

volumetric expansion as a function of time under zero pressure. The system was them fixed at its average system dimensions at 300K and equilibrated in NVT ensemble at specified temperatures. This was followed by NVE ensemble to further equilibrate the system before starting to record the heat current autocorrelation. With maximum frequency of 30THz, the time for one full oscillation is 3.33×10^{-2}s. Low timesteps of 0.5fs was used to optimize sampling rate within one oscillation and to maintain energy conservation at given simulation temperature. Each system configuration was simulated five times for improved data mean and control of variability in initial velocities. Another challenge of Green-Kubo (GK) is the convergence of the heat current (flux) indicating time for system equilibration. Recent studies have highlighted the relevance heat flux integral contribution (see equation 2.1) in predicting the thermal conductivity based on duration of the oscillation [17, 18]. However, researchers have presented different views on how much oscillation time is sufficient and its significance to thermal diffusivity.

After system equilibration, autocorrelation of the heat flux was computed from the time series data from longer simulation time to reduce statistical noise. The averaged data from multiple correlation was considered to converge within 35ps of simulation time. Green-Kubo method uses the trapezoidal rule to integrate the heat current autocorrelation function (HCACF) $< J_i(0).J_j(\tau) >$ as expressed in equation 2.2. The normalized autocorrelation function (ACF) is shown in fig. 3.2.

Size Convergence

The hexagonal closed packed unit cell of ZrB_2 presents an opportunity to create data file of different box sizes. Defect-free crystalline system of ZrB_2 of different box dimension were investigated for thermal conductivity values as presented in Fig. 3.1. Simulations were

performed for different system configurations to understand the size effect on the thermal values. Fig. 3.1a correlates the thermal conductivities of 3 x 3 x 3 and a larger supercell 9 x 9 x 15 across temperature range (200-2100K). The supercell size is less impactful on the κ values. There is a wide variation in the computed thermal conductivity (κ) ranging from 45-194 W/(mK) as presented in Fig.3.1b with box size configuration starting from 3 x 3 x 3 to 15 x 15 x 15 at 300K. It is interesting to note that in the x and y direction, thermal conductivity decreased with increasing box length. Thermal conductivity, κ was computed using 6 x 6 x 9 supercell dimensions. Along the z-axis there is no conclusion on impact of box length on κ values. Studies have shown that there are directionally dependent thermal properties [19], however in this case our study is to optimize the average thermal conductivity by first performing size convergence. The average κ (Fig. 3.1a) is close to reported experimental data [20] but the contribution in each axial direction was not reported. Also, critical to using Green-Kubo is the convergence of the heat current autocorrelation function (HCAF).

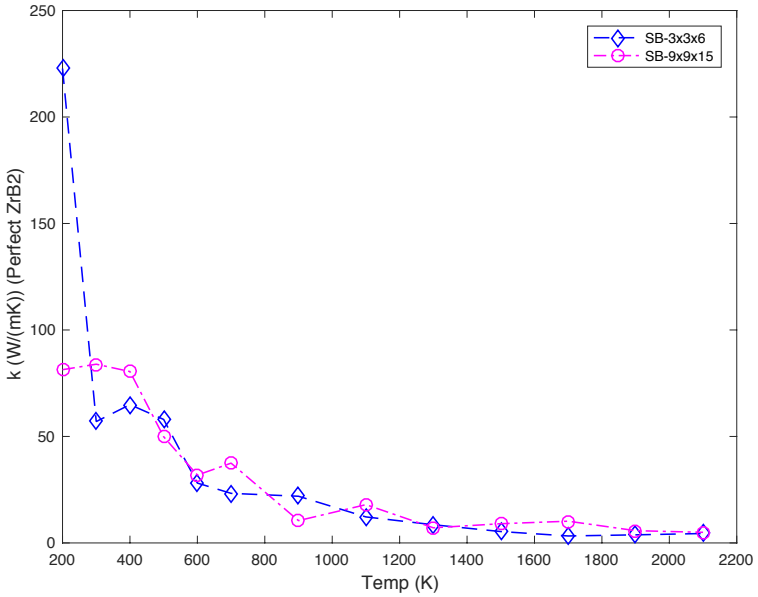

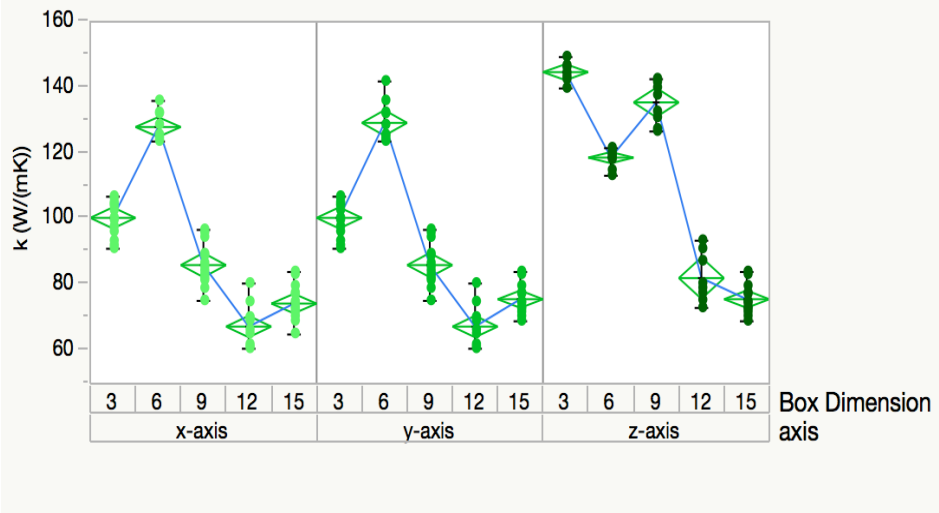

Fig. 3.1. In (a) thermal conductivity, κ for ZrB_2 in different supercell sizes across temp range (b) is the directional k along the basal x and y directions and z-direction at 300K.

HCACF Convergence

Fig. 3.2 presents the normalized heat current autocorrelation function (nHCACF). The result below shows defect-free crystalline ZrB_2 at T=300K as a control for variability in the presence of defects in subsequent simulations. The simple moving average model for the time series was applied to analyze the computed heat current. The decay and frequency of oscillation is similar on the basal direction along x and y but different from the decay in the z-direction. Although the initial oscillation in the z-direction is regular but converges faster. From Fig. 3.2, z-direction (HCCFzz) shows a slower convergence with high oscillations between ~23 - 30ps. The HCCFzz demonstrates why the simulation time should be truncated to prevent any accumulation of noise over longer time, similar approach was adopted by L. S. Oliveira in the study of thermal properties of graphite [30]. Along the x- and y-axis, long lasting simulation is required due to slower but more regular decay. The HCACF result is comparable to that obtained by Lawson et

al., [16] as it presents the decay along all three directions. The simulation times was sufficient for heat flux convergence along all axial directions and therefore the result is computed with relatively minimum noise, at which T=300K is about 127W/(mK) on average. Other methods have been reported to use longer and shorter simulation times to compute thermal conductivity. However, true thermal conductivity can only be computed at infinite simulation time, to include all average fluctuations.

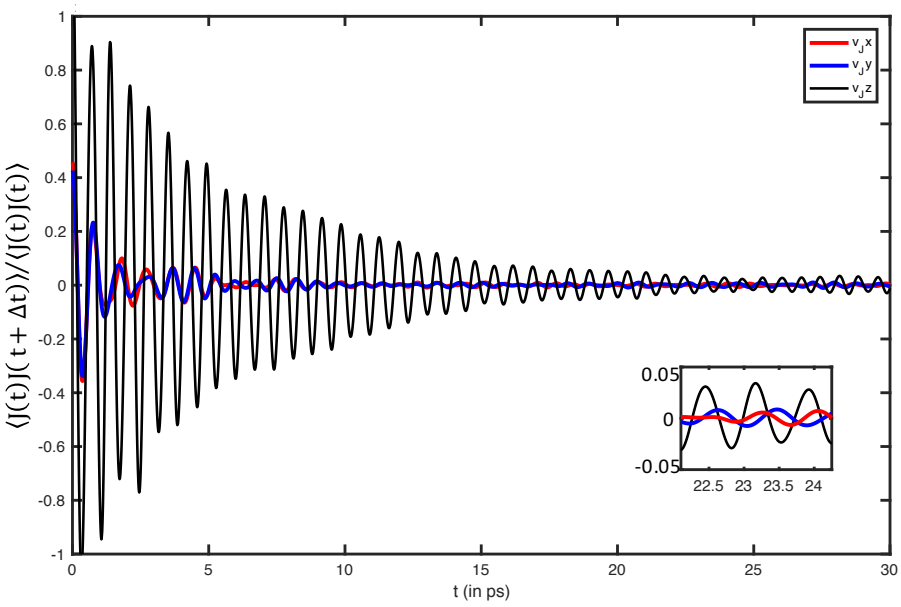

Fig. 3.2. the normalized HCACF computed overlay along xyz-axis for perfect ZrB_2

Thermal Conductivity of Defected ZrB_2

Previous articles have reported thermal conductivity trend for ZrB_2 with temperature but no characterization of thermally resistive processes due to point defects [20, 21]. Experiments have also shown differences in measured κ values for single crystal and polycrystalline ZrB_2, attributed mostly to grain boundaries resistance in polycrystalline [23]. Here we computed κ

values in the presence of different point defects class in ZrB_2 using a 6 x 6 x 9 supercell size at 300K. Thermal conductivities for vacancies and isotopes were higher than interstitial defects both for boron (B) and zirconium (Zr) (see Fig. 3.3). While Zr atoms interstitials measured κ values from 24.6, 13.9 and 5.4 W/(mK) for two, four and six interstitial atoms respectively, B atoms interstitials recorded 4.57, 11.3 and 6.72 W/(mK). For vacancy defects, measured κ values were higher than that for perfect ZrB_2 structure. Computed κ 183 and 198 W/(mK) respectively for two B and two Zr vacancies. Lee et al also recorded increased conductivity due to vacancy defects in graphene but attributed them to changes in localized electrons. Also, recent study by Oliveira and Greaney suggests the presence of localized modes for certain defect types [30, 31]. Significant differences in the results can be attributed to changes in the frequency of vibrational modes but there is more work to be done to determine how the orientation influenced the heat flux in the axial directions.

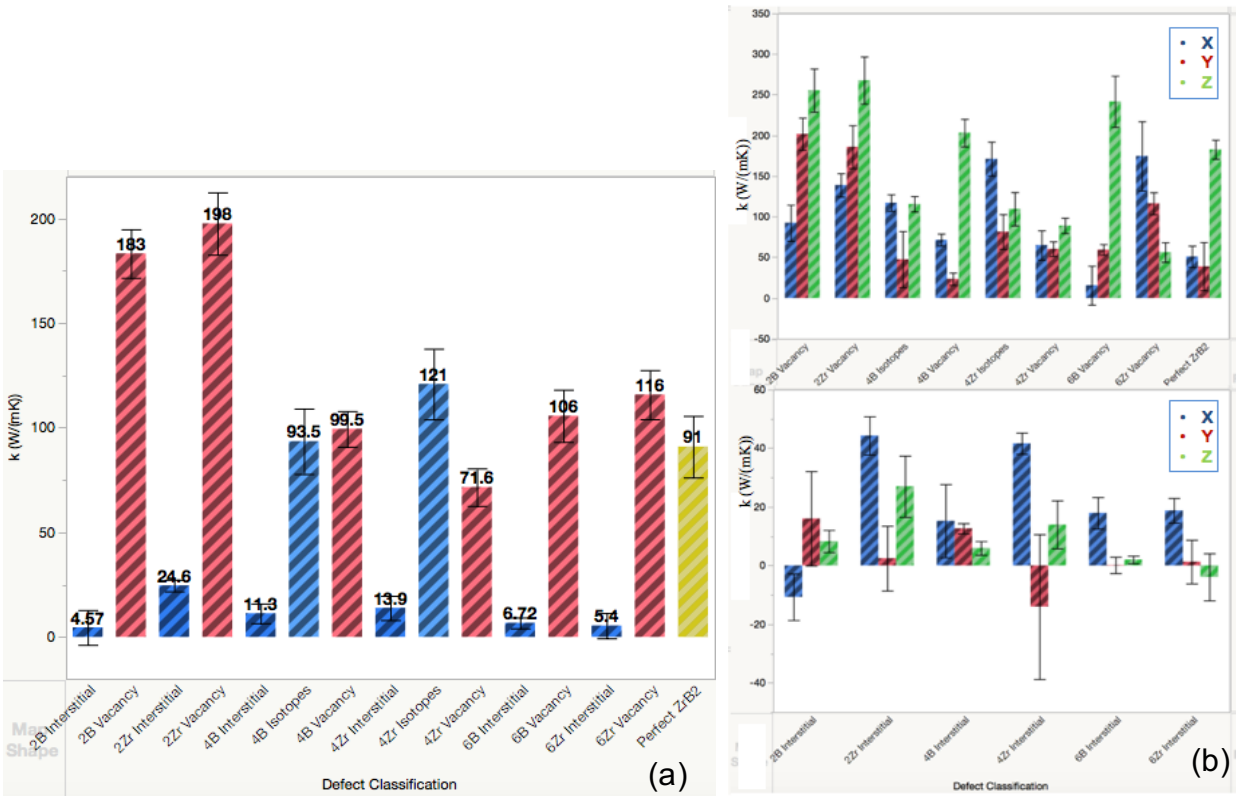

Fig. 3.3. Thermal conductivity values for different ZrB_2 defect systems at room temperature, (a) shows average k, (b) k in the x, y, z-directions for vacancy and interstitial defects.

The vacancy and isotopic defects increased κ values in the z-direction and proportional change in the basal direction. Similar results were obtained using a different supercell size hence the results may be dependent on the interlayer spacing and defect alignments. Interstitial defects decreased thermal conductivity both on the x-y plane and z-axis. Indicative of the thermal resistance imposed in the presence of interstitials of both Zr and B in the structure. The impact of vacancy defects was different, the vacancy defects increased k values in the c-direction and proportional change in the basal direction however, this value decreased as the number of vacancies increased. It is unclear if the B vacancies allow for a stronger lattice vibration but the absence of B-B sigma bond would improve interlayer Zr-Zr metallic bond. It is unclear if the B vacancies

allow for a stronger lattice vibration of the σ-bonds [9], however, the absence of B would constitute a stronger Zr-Zr metallic bond and thereby increasing thermal conductivity [10].

Experimental estimate at 300K by Devon Lee [20] measured 88 W/(mK) and the simulation results are in agreement for perfect ZrB_2 structure. This κ value is lower than 108 W/(mK) for sintered ZrB_2 measured by Zhang et al. These κ values are comparable to results at low temperatures published in other articles [9, 20-23]. The results presented in Fig. 3.3 do not indicate thermal conductivity variation with the number of defects in a cluster but rather the type of defects and maybe the spacing. There are little notable differences in the κ values computed along the z-direction compare to the basal directions for the various defect types. The injection of these defects is expected to change neighbor orientations, bond types and lengths. These characteristic changes are anisotropic and impact directionally dependent components such as the heat flux. In Fig. 3.4, the anisotropic ratio computed for the basal directions is presented for the various ZrB_2 classifications. Studies have not shown the changes in frequency modes to appropriately characterize thermal conductivity degeneracy or upswing.

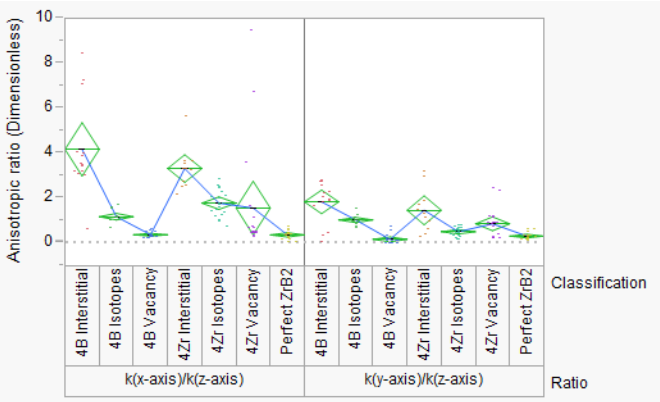

Fig. 3.4. Anisotropic ratio computed for the basal directions (x and y) in relation to z for the defect types.

Thermal conductivity values on Fig 3.3 indicate that the spatial orientation of the defect could be different and therefore pose variation in the overall conductivity of the system. There is

a dependence of κ on the type of defects whether interstitial or vacancy. However, there is little difference with regards to the number of interstitials or vacancies. Influence of an extra B-atom or the absence of it on the σ-bond within B plane and weak Π-bond intra-plane is reflected in the change in κ value recorded. In determining the resistance imposed by these defects relative to defect-free ZrB_2, the Mathieson's rule is applicable. If defect is considered a source of phonon scattering, according to Mathieson's rule the total resistivity is the sum of resistivity due to the defects and the resistivity due to the lattice vibration in the crystal structure. Therefore, the imposed thermal resistance (r) due to defect is calculated as shown below:

$$r_{defective} = r_{perfect} + r_{defects} \tag{3}$$

but thermal resistance, r = 1/κ, of the system

$$r_{defect} = \frac{1}{\kappa_{Defective}} - \frac{1}{\kappa_{Perfect}} \tag{4}$$

If the assumption of Mathieson is applicable, that means each defect scattering contribution is independent and the thermal resistance of the system is additive. The additive contribution to the thermal resistance due to defect is given as $r_{defect} = r_{defective} - r_{perfect}$. Fig. 3.5 presents the computed thermal resistance for a system size without defect ($r_{perfect}$) and one with point defects ($r_{defective}$). It therefore suggests that the same system size with double the number of defects would be in the form $r_{defective-2} = r_{perfect} + 2.r_{defects}$. The resistivity of the two interstitial Zr and B defects system are 0.09 and 0.24 mK/Wx10^{-3} respectively. However, the respective resistivity of four interstitial defects are 0.08 and 0.11 mK/Wx10^{-3}. Therefore, doubling the number of point defects does not correspondingly double thermal resistance. It is however (worth noting) that there are no data regarding how the orientation and

stacking of the defect in the system will change the resistive contributions.

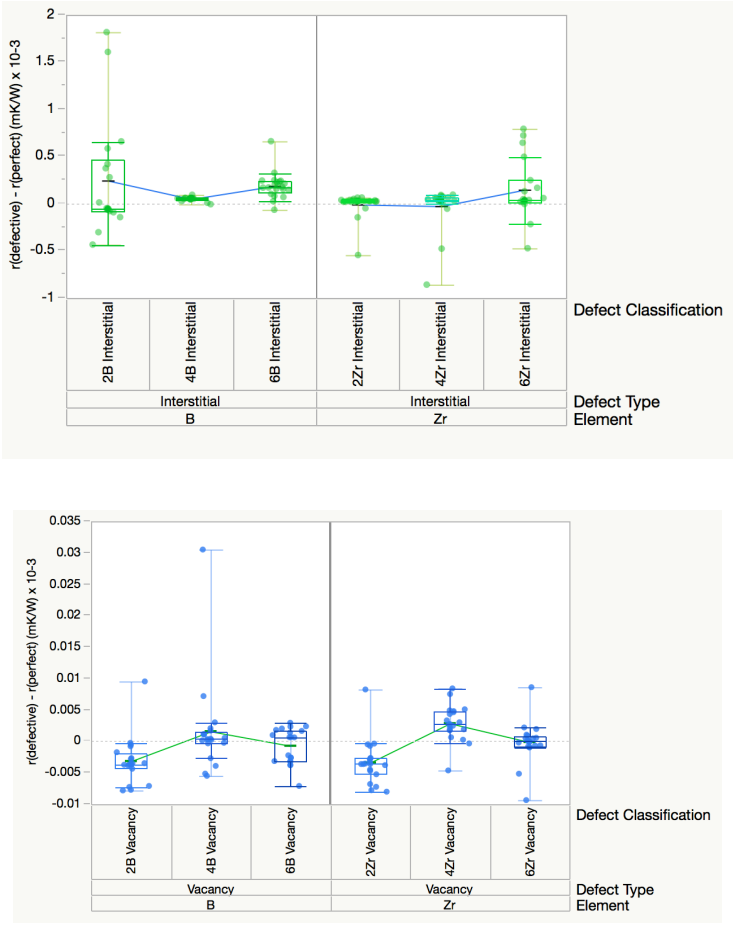

Fig. 3.5. Independent thermal resistance contribution of (a) B and Zr interstitial (b) B and Zr vacancies in ZrB_2 system

Summary and Conclusions

In this study, we have reported the thermal conductivity of both defect-free and imperfect ZrB_2 by Green-Kubo simulations. Perfect crystal lattice of ZrB_2 is different from real crystal structure due to variation in densification processes and nature of synthetic powder. Vacancy defects, packing and interstitials are common to real ZrB_2 materials. With an optimized 6 x 6 x 9 supercells, the Green-Kubo approach was used, and autocorrelation function converged within 35ps correlations time. Frequency of oscillation and decay in the z-direction is different from

basal direction. At 300K vacancy defects gave higher thermal conductivity than defect-free ZrB_2 while interstitial defects lowered the thermal conductivity. The integrity of the lattice sites in the Zr interlayer, force the interstitial atoms to position between adjacent layers. Computed values of thermal conductivity below 750K (Debye temperature) are consistent with literature. Higher temperatures did not show significant difference with defect types, which could be attributed to size of the simulation system. In addition to computing the trend in thermal conductivity due to defects, we have correlated the change in cohesive property in terms of energy of ZrB_2 crystal system with defect formation. There is increased energy required for interstitial and vacancy defect formation with the number of defects.

Acknowledgments.

This work used Oregon State University computing resources and also resources of the Bioinformatics Computational Research Group in University of California Riverside.

References

1. Bansal, Narottam P., ed. *Handbook of Ceramic Composites*. Springer. p. 192 (2004).

2. Salute, Joan; et al. *SHARP-B 2: Flight Test Objectives, Project Implementation and Initial Results*. 2nd Annual Conference on Composites, Materials and Structures, Cocoa Beach, FL, United States (2001).

3. Agarwal, D. C., and U. Brill, "Material Degradation Problems in High Temperature Environments," *Industrial Heating,* p. 56 (Oct. 1994).

4. A. Jankowiak, J.F. Justin. Ultra High Temperature Ceramics for aerospace applications. *ODAS 2014*, Jun 2014, COLOGNE, Germany. <hal-01103216v2>

5. Sylvia M. Johnson. Ultra High Temperature Ceramics: Applications, Issues and Prospects. NASA-Ames Research Center. 2nd Ceramic Leadership Summit Baltimore, MD. August 3, 2011

6. Zimmermann, J. W., Hilmas, G. E., Fahrenholtz, W. G., Dinwiddie, R., Porter, W., and Wang, H. “Thermophysical Properties of ZrB2-Based Ceramics” Journal of the American Ceramic Society 91, no. 5 (2008):1405-1411.

7. Hilmas, G. E., Fahrenholtz, W. G., Talmy, I. G., and Zaykoski, J. A. “Refractory Diborides of Ziconium and Hafnium” Journal of the American Ceramic Society 01, no. 5 (2007):1347-1364.

8. Wangsheng Chu[a, b], Ziyu Wu[b, d,], Wenhan Liu[a], N.L. Saini[c], A. Bianconi[c], Tiandou Hu[b], Yaning Xie. Lattice dynamics study of AlB2-type 4d transition-metal diborides by extended X-ray-absorption fine structure. Radiation Physics and Chemistry. Volume 127, (October 2016) .

9. Hyoung Joon Choi*, David Roundy*†, Hong Sun*, Marvin L. Cohen*† & Steven G. Louie. The origin of the anomalous superconducting properties of MgB2. Nature. Vol 418 (2002)
10. J. W. Zimmermann, G. E. Hilmas, and W. G. Fahrenholtz, "Thermophysical Properties of ZrB2 and ZrB2-SiC Ceramics," *Journal of the American Ceramic Society,* 91[5] 1405-11 (2008).

11. Melville S. Green. Markoff random processes and the statistical mechanics of time dependent phenomena. ii. irreversible processes in fluids. The Journal of Chemical Physics, 22(3), 1954.

12. Rajiv Asthana; Ashok Kumar; Narendra B. Dahotre (9 January 2006). Materials Processing and Manufacturing Science. Butterworth–Heinemann. pp. 158–. ISBN 978-0-08-046488-6. Retrieved 7 May 2013.

13. D. A. McQuarrie, Statistical Mechanics. University Science Books, Sausalito (2000)520-521.

14. Vijaya & Rangarajan and Gopala Rangarajan. Materials Science. Tata McGraw- Hill Education, February 2004. ISBN 0070534691.

15. H. Kaburaki, J. Li, S. Yip, and H. Kimizuka, J. Applied Physics 102,043514 (2007)
16. J. W. Lawson, M. S. Dawson and C. W. Bauschlicher, Jr. Lattice thermal conductivity of ultra-high temperature ceramics ZrB_2 and HfB_2 from atomistic simulation. Journal of Applied Physics, 110, 083507 (2011).

17. Laura de Sousa Oliveira, P. Alex Greaney. Thermal resistance from irradiation defects in graphite. Computational Materials Science 103 (2015) 68–76

18. D. P. Sellan, E. S. Landry, J. E. Turney, A. J. H. McGaughey, and C. H. Amon. Size effects in molecular dynamics thermal conductivity predictions. Phys. Rev. B 81, 214305 – Published 21 June 2010

19. William A. Paxton,1 Tevfik E. Özdemir,1 İlyas Şavklıyıldız, Terence Whalen, Hülya Biçer, Enver Koray Akdoğan, Zhong Zhong, and Thomas Tsakalakos1. Anisotropic Thermal Expansion of Zirconium Diboride: An Energy-Dispersive X-Ray Diffraction Study. Journal of Ceramics Volume 2016 (2016), Article ID 8346563

20. McClane, Devon Lee, "Thermal properties of zirconium diboride - transition metal boride solid solutions" (2014). Theses. Paper 7265.

21. H. Kinoshita, S. Otani, S. Kamiyama, H. Amano, I. Akasaki, J. Suda and H. Matsunami. Zirconium Diboride (0001) as an Electrically Conductive Lattice-Matched Substrate for Gallium Nitride. Japanese Journal of Applied Physics, Volume 40, Part 2, Number 12A.

22. J. W. Zimmermann, G. E. Hilmas, W. G. Fahrenholtz, R. B. Dinwiddie, W. D. Porter, and H. "Thermophysical Properties of ZrB2-Based Ceramics" Wang. Journal of the American Society. Vol. 91, 1405 (2008).

23. Zhang, D. A. Pejaković, J. Marschall, and M. Gasch, "Thermal and Electrical Transport Properties of Spark Plasma-Sintered HfB_2 and ZrB_2 Ceramics," Journal of the American Ceramic Society, 94[8] 2562-70 (2011).

24. Murray S. D., John W. L., and Charles W. B. Interatomic potentials for Zirconium Diboride and Hafnium Diboride. Computational Material Science 50 (2011) 2828-2835.

25. Thompson, M. J., Fahrenholtz, W. G., and Hilmas, G. E. "Elevated Temperature Thermal Properties of ZrB2 with Carbon Additions" Journal of the American Ceramic Society 1085, (2012)

26. Clougherty, E. V, Wilkes, K. E, and Tye, R. P. "Research and Development of Refractory Oxidation-Resistant Diborides" (1969).

27. S. Guo, T. Nishimura, and Y. Kagawa, "Preparation of zirconium diboride ceramics by reactive spark plasma sintering of zirconium hydride–boron powders," Scripta Materialia, 65[11] 1018-21 (2011).

28. Middleburgh, Simon C.; Parfitt, David C.; Blair, Paul R.; Grimes, Robin W. (2011). "Atomic Scale Modeling of Point Defects in Zirconium Diboride". Journal of the American Ceramic Society. 94 (7): 2225–2229

29. Zhi Wang and Zhanjun Wu. Fabrication, Microstructure, and Properties of Zirconium Diboride Matrix Ceramic. Dalian University of Technology, China. Source Title: MAX Phases and Ultra-High Temperature Ceramics for Extreme Environments. (2013) 59. DOI: 10.4018/978-1-4666-4066-5.ch012

30. Martin Dahlqvist, Ulf Jansson and Johanna Rosén, Influence of boron vacancies on phase stability, bonding and structure of MB2 (M = Ti, Zr, Hf, V, Nb, Ta, Cr, Mo, W) with AlB2 type structure, 2015, Journal of Physics: Condensed Matter, (27), 43, 435702.

31. L. S. Oliveira, P. A. Greaney, Thermal resistance from irradiation defects in graphite. Computational Materials Science 103 (2015) 68–76.

32. Geunsik Lee, Kwang S. Kim, and Kyeongjae Cho, Theoretical Study of the Electron Transport in Graphene with Vacancy and Residual Oxygen Defects after High-Temperature Reduction. J. Phys. Chem. C, 2011, 115 (19), pp 9719–9725

4.0 Effect of defects on coefficient of thermal expansion and specific heat capacity of ZrB_2

Jude O. Ighere, Aria Hosseini, Laura de Sousa Oliveira, and P. Alex Greaney

Abstract

Due to thermal storage potential and thermal expansion properties, ZrB_2 is favorably considered for advanced applications including supersonic aircraft and fusion reactors. This article presents density functional theory calculations of its states, microstructure and quasi-harmonic levels calculations of thermophysical properties. Band structure highlighted dynamical instability with metallic impurities in ZrB_2 structure based on frequency modes. The observed projected density of states (PDOS) appropriate 4d orbital of Zr dominated at low frequency both in perfect crystal in the presence or absence of covalent impurities while B 2s and 2p orbitals dominate higher frequency states. Temperature dependency and anisotropy of coefficient of thermal expansion (CTE) were evaluated with various impurities. Various thermodynamic properties like entropy and free energy were explored for degrees of freedoms resulting from internal energy changes in the material. Computed results for heat capacity and CTE were compared to available numerical and experimental data.

Introduction

Zirconium diboride (ZrB_2) attracts much attention as it is used in various high temperature applications including nuclear reactors, turbine engines and leading-edge aircraft due to its unique thermal properties at extreme conditions. This ultra-high temperature ceramics (UHTC) reportedly melts at the range of 3000-3245^{o}C [5, 6]. The characteristic properties of expansion and heat capacity are therefore critical to inform life design methods for thermal stress

optimization. This article is concerned with the impact of defects on its thermal properties and the hexagonal lattice structure of ZrB_2. With relatively low density, ZrB_2 is a list of few candidates for hypersonic flight which generates high temperatures at its leading edges. Its atoms do not deviate from their lattice sites hence the thermal and mechanical stability which is ascribed to its well layered in-plane and out-of-plane bonding in the hexagonal honeycomb (Fig. 1).

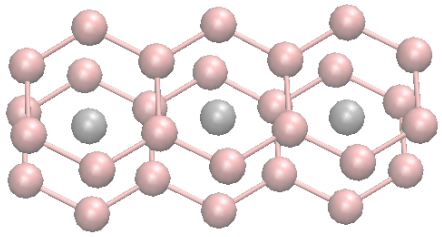

Fig. 1: Hexagonal Honeycomb layers of boron-boron atoms alternate with layers of Zirconium atoms centered in the hexagons.

The behavior of the material under thermal stress are quantified using heat capacity and thermal expansion. However, the perfect crystal of ZrB_2 rarely exist due to its partially covalent nature, and induced defects from synthesis and sintering processes [7-9]. Defects such as surface oxides, metallic impurities and carbides are unavoidably created during processing stages or exist in nature. These impurities, when present, results in microscopic structural changes, and hence redistribution in localized electron density. This induced variation in the mechanical reliability of the material creates phonon or electron (carrier) scattering differences evident in its thermal properties or processes.

First principle calculations are critical at such microscopic levels to contrast the perfect ZrB_2 crystals to one with impurities and correlate electrical and thermodynamic properties. In this article, band structures and density of states (DOS) were investigated and the defect commonalities to heat capacity and thermal expansion explored.

Coefficient of Thermal Expansion of ZrB_2

In considering ZrB_2 as the leading favorite in the internal design of nuclear reactors, one should critically evaluate its lifecycle potential based on expansivity [10,11]. Studies have shown that the thermal expansion of ZrB_2 is anisotropic along the various lattice directions [1]. This directionally dependent property is attributed to the varying bond strengths along the different axes which determines stiffness and therefore the expansion [3, 4]. Researchers have attributed the characteristic stiffness of ZrB_2 crystal structure to the strong in-plane boron-boron sigma covalent bonds (Fig. 1). [2, 3]. Generality of the expression for coefficient of expansion holds true on the assumptions: (i) that the expansion is insensitive to the individual axial-direction (ii) the individual molecules do not expand but merely vibrates due to kinetic energy. Therefore, for ZrB_2, the essence of linear expansion is also considered to quantify the anisotropic thermal expansion especially in the z-direction. The coefficient of linear thermal expansion is given as $\alpha_{x,y,z} = (1/L_i)(dL_i/dT)$, where L_i represents specific axial-length (x, y, z) at temperatures T. For a typical solid, the coefficient of thermal expansion (CTE) (or volumetric expansivity) is generally expressed as;

$$\gamma = \frac{(V_f - V_i)}{V_i(T_f - T_i)} \quad (1)$$

where γ is the volumetric expansion coefficient, $V_{f,i}$, $T_{f,i}$ are the respective initial and final volumes and temperatures. However, in potentially anisotropic materials, the linear (directional)

expansion along the different directions can be calculated using;

$$\alpha(l) = \frac{1}{l}\left(\frac{\delta l(T)}{\delta T}\right) \quad (2)$$

where l dimension of the crystal lattice in any direction x, y, z and $\alpha(l)$ is respective linear coefficient of thermal expansion.

In leading edge applications (figure 2), aircraft moving through space with speed many times the speed of sound are subjected to extremely high thermal stress. Uneven expansion and contraction across the temperature gradient poses a threat to structural reliability of the material. Thus, this work investigated temperature dependency of CTE for ZrB_2 and the impact of impurities.

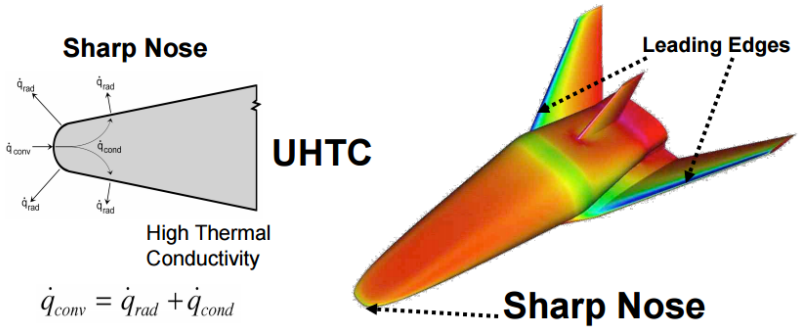

Figure 2: Depicting temperature gradient and regional component in ramping temperatures [18].

Specific Heat Capacity of ZrB_2

Several studies have focused on thermal conductivity and diffusivity of ZrB_2-based ceramics but only a few have given attention to its heat capacity. This property is essential in characterizing the state of the microstructure of materials for improved tailoring [12,13]. It can be defined at constant volume or pressure and correlated respectively to the internal energy or

enthalpy of the crystal structure. Phonon-based (lattice) constant volume heat capacity was formulated by Einstein and later modified by Debye for low temperatures are shown in equations 3 and 4 respectively;

$$\mathrm{C_{Ev}} = 3\mathrm{NK_B}\frac{\mathrm{x^2 e^x}}{(\mathrm{e^x}-1)^2} \tag{3}$$

$$C_{Dv} = 9NK_BT\left(\frac{T}{\theta_D}\right)^3\int_0^{\theta_D/T}\left(\frac{x^4e^x}{(e^x-1)^2}\right)dx \tag{4}$$

where θ_D and N represent the Debye temperature and the Avogadro and $x = \hbar\omega/K_BT$. This relationship is simplified at low temperature and can be written as;

$$C_v = \beta T^3 \tag{5}$$

The coefficient, β (specific heat coefficient) is correlated to the Debye temperature $\theta_D(0)$ via;

$$\theta_D(0) = \left(\frac{1944}{\beta}\right)^{\frac{1}{3}} \tag{6}$$

Both models show that the transfer of phonons in lattices contribute to measurable change in the energy. And Debye's model further attributes the interaction between harmonic oscillating atoms to the exponential increase in heat capacity with temperature. Also analyzed in this article are the free energy, entropy and enthalpy of the system in a bid to explain the heat capacity offset in the presence of impurities.

Computational Details

The density function theory (DFT) calculations for this study were performed using Vienna Ab-initio Simulation Package (VASP) [14,15]. The projected augmented wave (PAW) exchange energy potential was used in combination with the correlation functional developed by Perdew, Burke, and Ernzerhof (PBE). A cutoff of 600eV was used for the kinetic energy for the planewave, and a Monkhorst-Pack k-point mesh of 4x4x4. The free (total) energy change and band structure energy change convergence point was set to less than $1x10^{-4}$eV between steps. For a more accurate band structure and density of states, higher k-point grid 12x12x12 was further used. A classical molecular dynamic simulation data was also employed for comparison. Phonopy (open source package) was used for phonon calculations. Package uses statistical thermodynamic expressions to compute free energy (F), heat capacity (C), entropy (S), and enthalpy (H). Smearing method was used via Phonopy to calculate the phonon density of states (DOS) on a sampling mesh.

The classical MD simulations were performed using Large-Scale Atomic/Molecular Massively Parallel Simulator (LAMMPS) to calculate the coefficient of thermal expansion (CTE) of perfect ZrB_2 and contributions from impurities [16]. Tersoff interatomic potential was used to describe the atomic interactions [17]. Tersoff potential has been used previously to model the properties of Zr, B, Hf, ZrB_2 and SiC [4,9,17]. Periodic boundary conditions were applied to model the ZrB_2 crystal structure to enable interaction across boundary. Langevin thermostat was used to control the temperature within NPT ensemble. This mechanical ensemble allows for variable volume at equilibrium, at constant pressure and temperature. Defining the thermodynamic trend of the system. A timesteps of 0.5fs was employed with 0.6 ns equilibration time for within a simulation duration of 15 ns. Literature values for ZrB_2 lattice constant were

adopted, $\boldsymbol{a_o}$, $\boldsymbol{b_o = 3.035}$ Å and $\boldsymbol{c_o = 3.223}$ Å. All atoms with same z-coordinates are termed same plane, with alternating B and Zr layer. Added validation procedure to ensure that the crystal lattice generated (see Fig. 3b) does not deviate was applied and VESTA was used to load and generate XRD patterns for the created lattice structure. Fig. 3, compares to published experimental XRD patterns for perfect ZrB_2 [1].

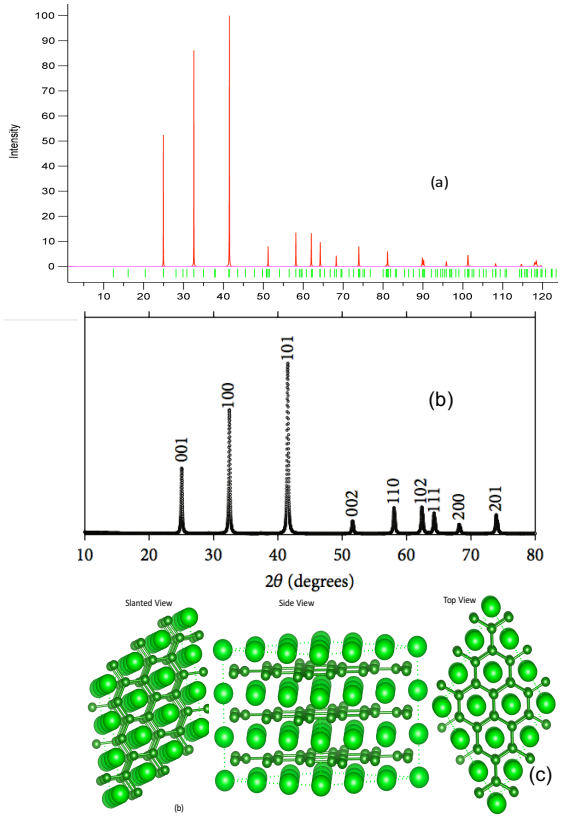

Fig. 3 (a) XRD pattern for perfect ZrB_2 crystal lattice (a) obtained from VESTA, (b) obtained from experiment (c) lattice structure created and used for simulations.

Results and Discussions

Thermal Expansion Coefficient of ZrB_2

At near room temperatures (300K), the CTE for all configurations coincide at 2.5~3.0x10^{-6} K^{-1}. Thermal expansion shows early stable expansion with temperature from 300 to 1200K and suffers contraction at temperature exceeding 2000 approaching melting values. CTE for Hf impurity stands out in its rate of expansion. Notable breakdown at temp above 3000K for all structures. NPT allows for dimension stabilization at given temperature which helps to predetermine the timesteps duration for thermodynamic equilibrium. Correlation showed early dependency on temperature which is consistent with reported analysis by Okamoto et al [19]. However, with temperatures reaching ~1500K, almost twice the Debye value for ZrB_2 (750K), the expansivity peaked for all configurations (see Fig. 4a). Hafnium (Hf) impurities in ZrB_2 was highest 7.9x10^{-6} K^{-1} at ~1500K while carbon (C), boron vacancies, boron interstitials defects were 6.1x10^{-5} K^{-1}, 6.25x10^{-6} K^{-1}, and 7.7x10^{-6} K^{-1} respectively. There is a slight correlation of CTE values to atomic radius (Hf > B > C) of the respective impurities added. The control simulation of perfect ZrB_2 reported values within the ranges previously reported in experiments (6.66-6.93x10^{-6} K^{-1}) compared to simulations (5.9-6.68x10^{-6} K^{-1}) [1,4,18,19]. Fig 4(a) also shows at temperatures within melting range (2900-3500^{o} C), there is a gradual break down, potentially structurally with uncontrollable expansivity. Also, the independent axial contribution to the expansion coefficient was investigated using the normalized values of the lattice parameters.

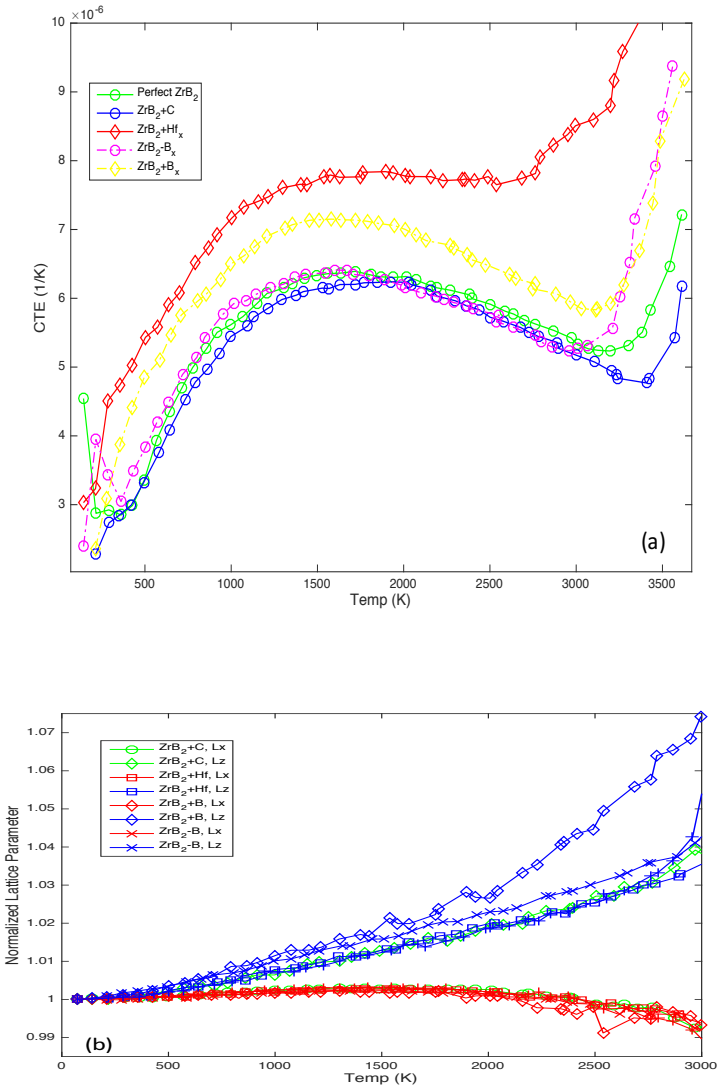

Fig. 4 (a) Coefficient of thermal expansion of ZrB_2 w/o defects. (b) temperature dependency of lattice parameter w/o defects

Fig 4. (b) shows the normalized lattice parameter with very uniform slow contraction along x and overlapping dimensions for all crystal lattice configurations. Along z, one can attribute expansion and dimension offsets to structural changes. It aligns with the results obtained from X-ray diffraction study on ZrB_2 anisotropy with matching reflections [1]. The structural and bonding properties of ZrB_2 was highlighted in the first article. With a strong (stiff) B-B sigma-

bond within-plane allowing the lattice structure to vibrate in the x-y plane only by first contracting, and thus enables the softer B-B pi-bond inter-plane to expand.

Specific Heat Capacity and Structure of ZrB_2

To understand the effect of the impurities on the structural characteristics, the calculated total density of states (DOS) are plotted in Fig. 5. The number of states for perfect ZrB_2 reduced with increasing energy level. DOS for the covalently bonding impurities (C and Si) are closely overlapped with the pure crystal but with more dominating states likely from the projected orbitals of Si and C impurities at higher energy. The metallic impurities showed some dynamic instability due to relaxation, and the non-imaginary states have been excluded from this analysis. Potential bonding interaction between the covalent nature of ZrB_2 with both Si and C is noticeable in the overlap with perfect structure (when overlayed) which is not the same for metallic impurities. Si extended the conduction band to 34.1eV, while C impurities made negligible changes to the conduction band. Both Hf and W impurities extended both the conduction and the valence band. The conduction band in all cases are dominated by B orbitals. Increased width of valence band denotes increase in electron delocalization and therefore reduced band gap. On the other hand, decreasing width of conduction band indicates electron delocalization weakening. Occurrence of these impurities generated additional localized states and potential changes to conductive properties. Lattice contribution to heat capacity is be computed from the phonon density of states (DOS) as using the expression below;

$$\mathbf{C_v(t) = K_B \int \frac{(\hbar\omega/K_BT)^2 e^{\hbar\omega/K_BT}}{[e^{\hbar\omega/K_BT}-1]^2} F(\omega) d\omega} \qquad (7)$$

where $\boldsymbol{F(\omega)}$ represents the phonon DOS, lattice heat capacity ($\boldsymbol{C_v}$), $\hbar$ represents Planck's constant and $\boldsymbol{K_B}$ denotes Boltzmann's constant.

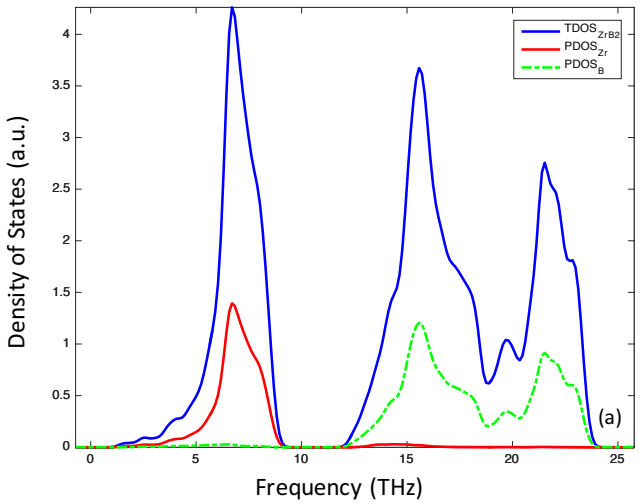

Fig. 5: Phonon total density of states (TDOS) and the projected contribution of Zr and B (PDOS)

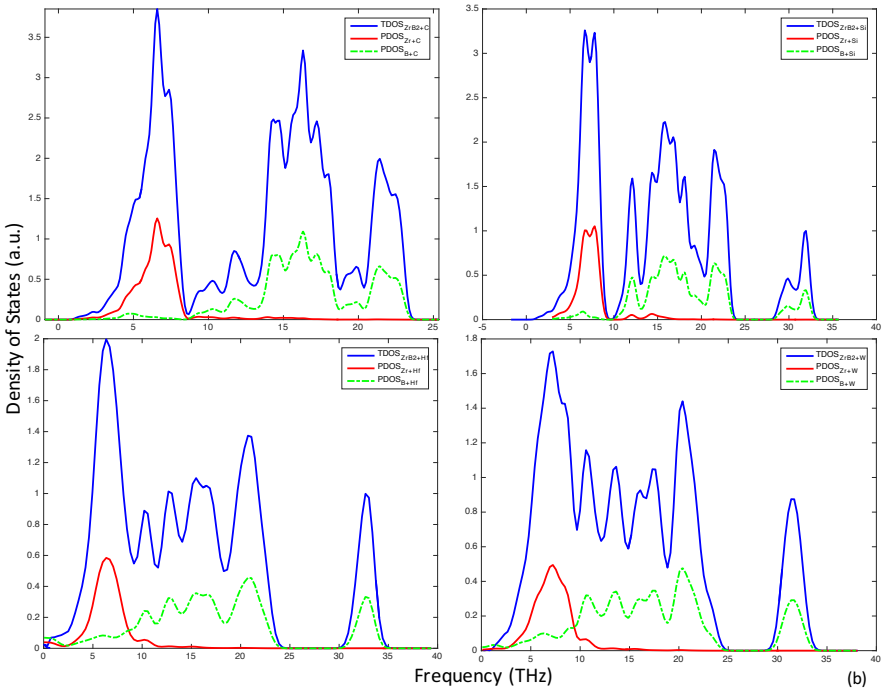

Fig. 6 Phonon density of states for ZrB_2 lattice structure with impurities of C, Si, Hf, W.

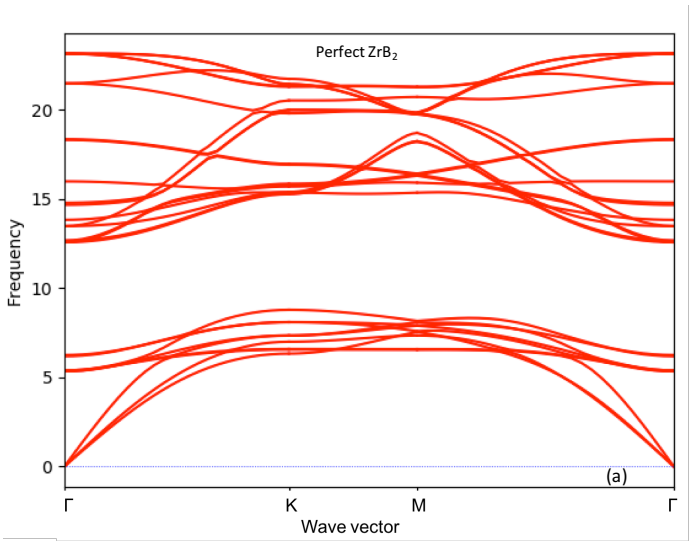

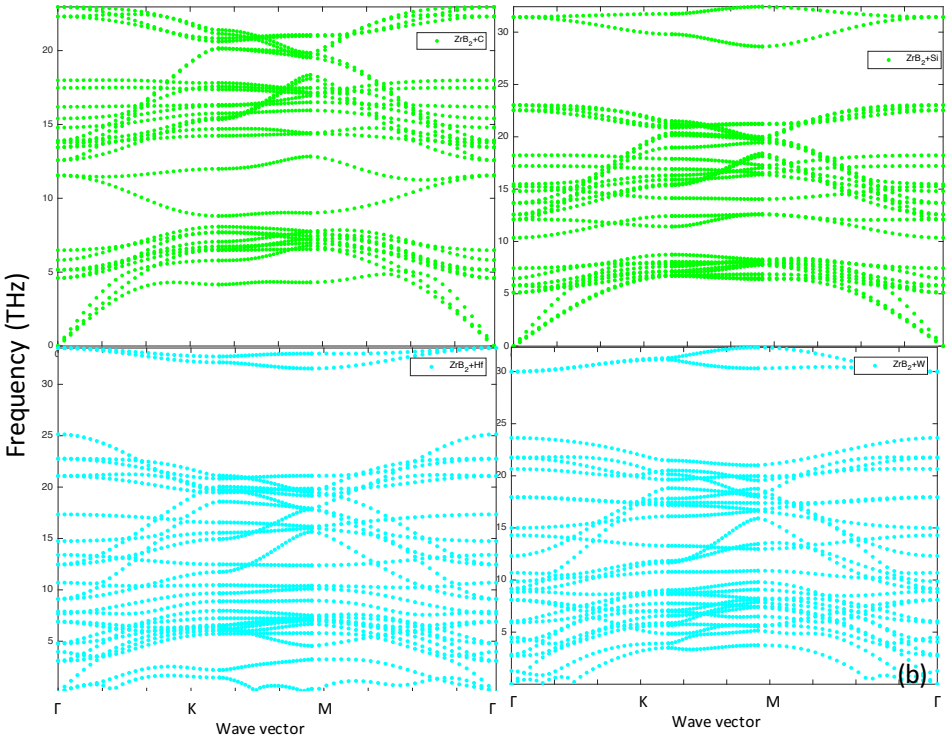

Fig. 7 Phonon dispersion (a) showing frequency modes for perfect ZrB_2 (b)frequency modes for ZrB_2 with impurities in lattice structure.

The phonon dispersion for ZrB_2 structure was calculated along the high symmetry directions Γ-K-M- Γ as presented in Fig. 6a. The result for perfect crystal, shows dynamic stability as there are no imaginary modes, thus consistent with M. S Daw et al data [20]. Such

stability is expected for structures with high atomic defect energy, low tendency for atomic distortion. In the presence of impurities, there are observable differences. C and Si impurities show dynamical stability similar to perfect structure but in addition to the dominant acoustic modes, there exist more low frequency optic modes. The added optic modes for Si are at relatively higher frequency than C. The case is different for the metallic impurities (Hf and W) with low and high frequency modes generated including more flat modes closing the gap between the conduction band and the valance band as shown in Fig. 7. The negative phonons (imaginary branches) created from non-relaxed Hf and W configurations were excluded from this analysis as it demonstrated dynamic instability for configurations with these impurities. It is noteworthy that some optic modes are also created by both Hf and W. The evolution of near zero frequency phonons transitioning, both normal and imaginary modes, points to changes in charge density area indicating that both of these metallic impurities have significantly distorted the original charge density distribution of ZrB_2. Also, no phonon softening is exhibited in band structure due to increased weight from added impurities.

The computed specific heat is plotted for the respective impurities as show in Fig 7a. The specific heat reaches a hard limit near the Debye temperature (~750K) following Dulong-Petit prediction. At maximum lattice vibration, phonon contribution to heat capacity will not change even with increased temperature based on Debye model. Phonopy applies quasi-harmonic approximations (QHA) which is not applicable at very high temperatures of complete anharmonicity. In this study, specific heat capacity in the temperature range of 0-1000K was investigated. The presence of 5%vol of Hafnium (Hf) and Tungsten (W) impurities shows specific heat capacity values of 91.8J/K/mol, closely matched to the perfect ZrB_2 at reference Debye temperature (750K) of ZrB_2 crystal structure. This value is similar to that of Carbon (C)

and Silicon (Si) impurities but both covalent impurities show a larger offset at lower temperatures. This can be described as stronger phonon scattering effects and reduced group velocity by Hf and W impurities in the ZrB_2 crystal. The subplot in Fig. 7a also shows the offset between Si and C in C_v.

Fig. 7b shows the changes in the thermodynamic properties with respect to lattice temperature. The dependences of free energy and entropy on lattice vibration and temperature are expressed in equations 8 and 9. The internal energy changes in the material is clearly observed in entropy dispersed. It is non-trivial but shows differences in the microstates (degrees of freedom) of the various material. Translating it by equipartition theorem, the small offsets in heat capacity values (Fig. 8a) is equivalent to changes in its degrees of freedom. The overlaps, further aligns with the differences in the phonon bands between the covalent (C and Si) and metallic impurities (Hf and W).

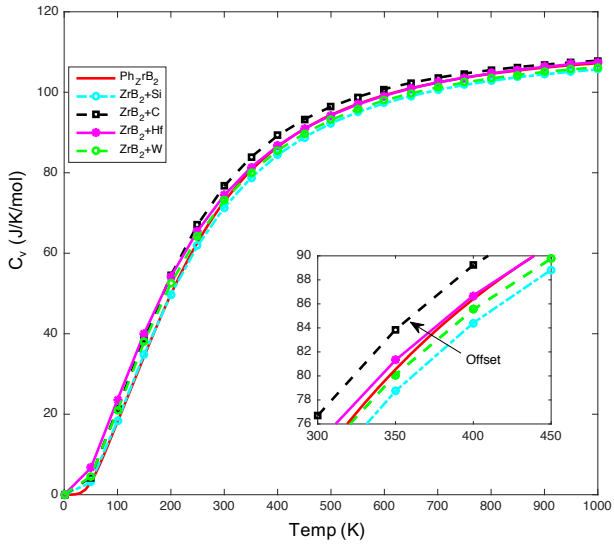

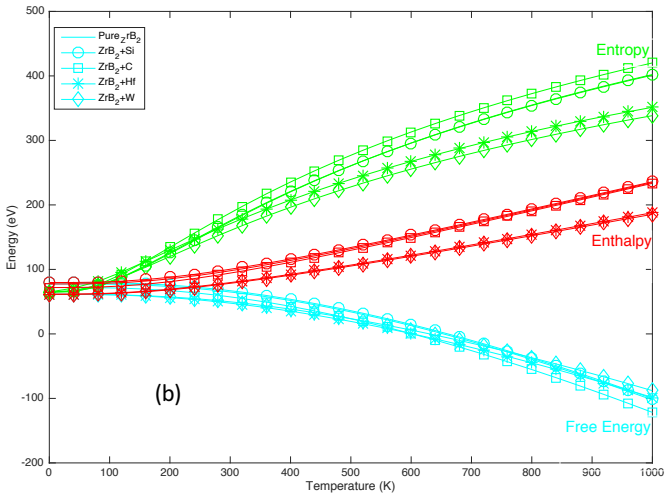

Fig. 8: (a) Overlay of calculated molar specific heat of ZrB2 with impurities (b) Thermodynamic properties: Free Energy, Entropy and Enthalpy of respective impurities with temperatures.

$$\mathbf{F(T) = E_{tot} + E_{zp}}$$

$$\mathbf{+K_B T \int F(\omega) ln[1 - e^{-\frac{\hbar\omega}{K_B T}}]\, d\omega\}} \qquad (8)$$

$$\mathbf{S(T) = K_B\{\int \frac{\frac{\hbar\omega}{K_B T}}{e^{\frac{\hbar\omega}{K_B T}} - 1} F(\omega) d\omega}$$

$$\mathbf{- \int F(\omega)[1 - e^{-\frac{\hbar\omega}{K_B T}}]\, d\omega\}} \qquad (9)$$

Summary and Conclusion

Having presented the approaches used for heat capacity and thermal expansion calculations with microstructural explanation using phonon properties, it has been shown that volumetric coefficient of thermal expansion is driven by anisotropic z-direction expansion with temperature. Impurity effects add to the knowledge gathering for better forecasting of thermal properties of ZrB_2-based materials. Exponential elevation of CTE near the melting temperatures shows structural breakdown and needs further investigation for phase transition. The challenge surrounding specific heat calculation, particularly using Phonopy is the quasi-harmonic level considerations, approximating anharmonic dependencies. Where available, computed thermal expansion and heat capacity data are compared to numerical and experimental data and are found to be within the range of experimentally reported results. Noteworthy is the redistribution of available states around the femi level by metallic impurities, different from the covalent impurities in the electronic density of states. Further interest in structural differentiation in ZrB_2 and other transition metal diborides by analytical development is justified as the production process has presented wide variations in density and purity of the material.

Acknowledgements

This work used Oregon State University computing resources and also resources of the Bioinformatics Computational Research Group in University of California Riverside.

References

1. Paxton A. W., Ozdemir T., Savkliyildiz I., Bicer H., Akdogan K., Whalen T., Zhong Z., Tsakalakos T., Anisotrpic Thermal Expansion of Zirconium Diboride: An Energy-Dispersive X-Ray Diffraction Study. Materials Science and Engineering, Rugers, The State University of New Jersey, Piscataway, NJ 08854 USA.

2. Kaji, N., Skikano, H., and Tanaka, I. “Development of ZrBr2-Graphite Protective Sleeve for Submerged Nozzle” Taikabustsu Overseas (1992):39-43.

3. Hyoung Joon Choi, David Roundy, Hong Sun, Marvin L. Cohen & Steven G. Louie. The origin of the anomalous superconducting properties of MgB2. Nature. Vol 418 (2002)

4. J. W. Zimmermann, G. E. Hilmas, and W. G. Fahrenholtz, "Thermophysical Properties of ZrB_2 and ZrB_2-SiC Ceramics," *Journal of the American Ceramic Society,* 91[5] 1405-11 (2008).

5. Rudy E. Ternary phase equilibria in transition metal-boron-carbon systems: part V, compendium of phase diagram data. Technical Report AFML-TR-65-2. Wright Patterson Air Force Base (OH): Air Force Materials Laboratory 1988.

6. Portnoi KI, Romasho VM, Vyroshina LI. Phase diagram of the zirconium-boron system. Poroshkoviaia Metallugia 1970;10(7):68-71

7. S. K. Mishra, S. Das and P. Ramchandrarao. Microstructure Evolution During Sintering of Self-Propagating High-Temperature Synthesis Produced ZrB2 Powder. Volume 17, Issue 11 November 2002, Pg. 2809-2814.

8. Kübra Gürcan and ErhanAyas. In-situ synthesis and densification of HfB2 ceramics by the spark plasma sintering technique Author links open overlay panel. Volume 43, Issue 4, March 2017, Pg. 3547-3555.

9. Zhang, S. C; Hilmas, G. E; Fahrenholtz, W. G (2006). "Pressureless Densification of Zirconium Diboride with Boron Carbide Additions". Journal of the American Ceramic Society. 89 (5): 1544–50.

10. Chubb, W. Coating a uranium dioxide nuclear fuel with a zirconium diboride burnable poison. 15 April, 86; US PATENT DOCUMENT 4,582,676/A/; U.S. Commissioner of Patents, Washington, D.C. 20231, USA.

11. I.B. Fiero and Z.E. Karoutas. Implementation of Zirconium Diboride Burnable Absorber Coatings in CE Nuclear Power Fuel Assembly Designs. Westinghouse Non-Proprietary Class 3, WCAP-16072-NP, Rev00 April 2003

12. V. V. Novikov, A. V. Matovnikov, O. S. Volkova and A. N. Vasil'ev. Synthesis, thermal and magnetic properties of RE-diborides. Journal of Magnetism and Magnetic Materials Volume 428, 15 April 2017, Pages 239-245 Volume 428, 15 April 2017, Pages 239-245

13. Mukubwa, A. (2018). Electronic Specific Heat of Iron Pnictides Based on Electron-Cooper Pair Interaction. Open Access Library Journal, 5: e5107.

14. G. Kresse and J. Furthmuller, ¨ Phys. Rev. B: Condens. Matter Mater. Phys., 1996, 54, 11169–11186.

15. G. Kresse and D. Joubert, Phys. Rev. B: Codens. Matter Mater. Phys., 1999, 59, 1758.

16. S. J. Plimpton, J. Comput. Phys. 117, 1(1995)

17. J. Tersoff, Phys. Rev. B 38, 9902 (1988)

18. Sylvia M. Johnson. Ultra-High Temperature Ceramics: Application, Issues and Prospects. NASA-Ames Research Center, 2nd Ceramic Leadership Summit Baltimore, MD August 3, 2011.

19. N. L. Okamoto, M. Kusakari, K. Tanaka et al., "Temperature dependence of thermal expansion and elastic constants of singlecrystals of ZrB2and th e suitability of ZrB2as a substrate for GaN film," Journal of Applied Physics, vol. 93, no. 1, article 88, 2003.

20. M. S. Daw, J. W. Lawson and C. W. Bauschlicher Jr. Interatomic Potentials for Zirconium Diboride and Hafnium Diboride. Computational Material Science 50 (2011) 2828-2835.

5.0 Characterizing Thermal Conductivity Effects of Impurities (C, Si, Hf, W) in ZrB_2: The role of Stiffness Matrices, Charge Density and Phonon Lifetimes

Jude O. Ighere, Aria Hosseini, Laura de Sousa Oliveira, and P. Alex Greaney

Abstract

The scope of thermal applications of ZrB_2 based ceramics depends on the effective engineering of heat carrier due to lattice vibration (phonons). Applying existing knowledge to characterize metallic (Hf and W) and covalent impurities (Si and C) effect on thermal transport determinants is presented in this study. Equilibrium simulation using Green-Kubo approach has been used for phonon thermal conductivity prediction at 300K. Simulated solid solutions with 5% impurities decreased thermal conductivity of perfect crystal structure of ZrB_2 from greater than 88 $Wm^{-1}K^{-1}$ to 39 $Wm^{-1}K^{-1}$ with C impurities, 46.5 $Wm^{-1}K^{-1}$ with Si, 88.3 $Wm^{-1}K^{-1}$ with Hf and 71.8 $Wm^{-1}K^{-1}$ W impurities. The resistance to thermal transport is correlated to impurity concentration. Increased resistance with increasing number of impurity atoms observed with exception attributed to impurity orientation. Electronic structure through density of states were calculated to correlate pseudo-gap and intensity variation between low and high frequency modes to dominant atomic orbitals. Phonopy used to compute the dispersion property and obtained the density of states (DOS). Projected DOS presents atomic orbital dominating the different regimes of the energy level as available state increased with added of Si, Hf and W except for the boron-like C impurity.

Introduction

The presence of impurities in bulk solid material is not avoidable based on occurrence in nature and the synthesis from constituent compounds and the densification procedure. These

impurities create distortion in physical property some of which are negligible based on the application. In-depth theoretical understanding of the physical properties and structure of the pure crystalline solid is fundamental to technological advancement. Zirconium diboride, ZrB_2, is the one of interest in this study since it has found applications in advanced thermal systems. Its real form is obtained from high temperature chemical processing of zirconium compounds with boron substituents and annealing from 800^o C to 1200^o C [1]. At such high processing temperature, powdered ZrB_2 is obtained, requiring densification. Due to it refractory nature, solid state sintering of powdered ZrB_2 is very difficult. Different techniques have been used for improved sintering and densification requiring enhancement by additives (or sintering aids), since sintering is usually at below melting temperatures [1-3]. Variations in manufacturing processes, densification and attrition-milled with tungsten-carbon, silicon-carbon or other media introduces differing purity and density which differentiates real materials from perfect lattice [7-9]. The impurities introduce electrostatic and geometric distortion resulting in new equilibrium positions for nearest neighbor atoms and new vibration frequencies. Although ZrB_2, is popular for ultra-high temperature applications, other areas requiring tailored properties ceramic matrix composites include thermoelectric, metrology probes, electrodes etc. Figure 1 illustrates the basic steps in sintering powdered solid.

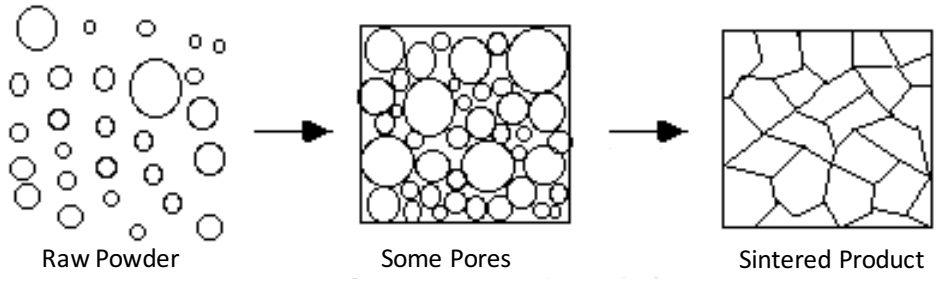

Fig 1: Illustrating the microstructural stages in sintering process

Thermal conductivity in crystalline solids are both phonon and electron driven. The carrier which dominates heat transport process in crystalline materials characterize these solids into conductors, semiconductors and insulators. The electron (e) contribution to the thermal conductivity of ZrB_2 can simply be obtained from the electrical conductivity using the relationship developed by Gustav Wiedemann and Rudolph Franz, $\kappa_e = \sigma LT$. Where L denotes Lorenz constant, T is temperature and σ is electrical conductivity. This paper focuses on phonon (ph) contribution to thermal conductivity computed using molecular dynamics (MD) simulations, solving Green-Kubo (GK) formulation. Most recent work by Lawson et al reported κ_e to be 32W/(m.K) while κ_{ph}as 28W/(m.K) for polycrystalline ZrB_2. Same article also noted that $\kappa_{tot}$for single crystal is much higher, with 140W/(m.K) along xy plane and 100W/(m.K) along the z-axis.

The mechanism of phonon heat transport correlates to the scattering mechanisms, phonon lifetimes, stiffness matrixes, density of states among other phonon properties. Essentially these properties are expected to vary between perfect lattice structure and one with defects. While GK solution is based on the fluctuation theorem and autocorrelation of heat flux, other direct non-equilibrium methods may compute thermal conductivity directly from Fourier law applications hence non-equilibrium methods do not present the full tensor of thermal conductivity.

Phonon Scattering, Lifetimes and Stiffness Matrix

The concept of phonon propagation derived from the understanding of vibrations of individual sites connected by bonds in frames governed by central-force springs. Characterized structural-mechanical stability of frames as stiffness can explain local force changes with respect to nearest neighbors per frame in the presence of imperfection. The stress induced due to

changing force constants creates different rigidity and percolates through crystal structure. Maxwell's rule (Maxwell's frames) later denoted these frames as lattices and quantified stiffness using coordination number. The transition in stiffness from one rigidity level to another in the presence of localized external force is a critical component in microstructural evolution as it relates to vibrational modes. For ZrB_2 which follows the family of AlB_2 crystal structure with different bonding types within structure. The alternating B and Zr layers (see Figure2) in the z-direction supports the covalent B-B sp^2 bonding and interlayer ionic Zr-B bonding, responsible for structural stiffness and characteristic properties [22, 23]. In this study, we examine phonon properties further by looking at the scattering mechanisms in the presence and absence of defects.

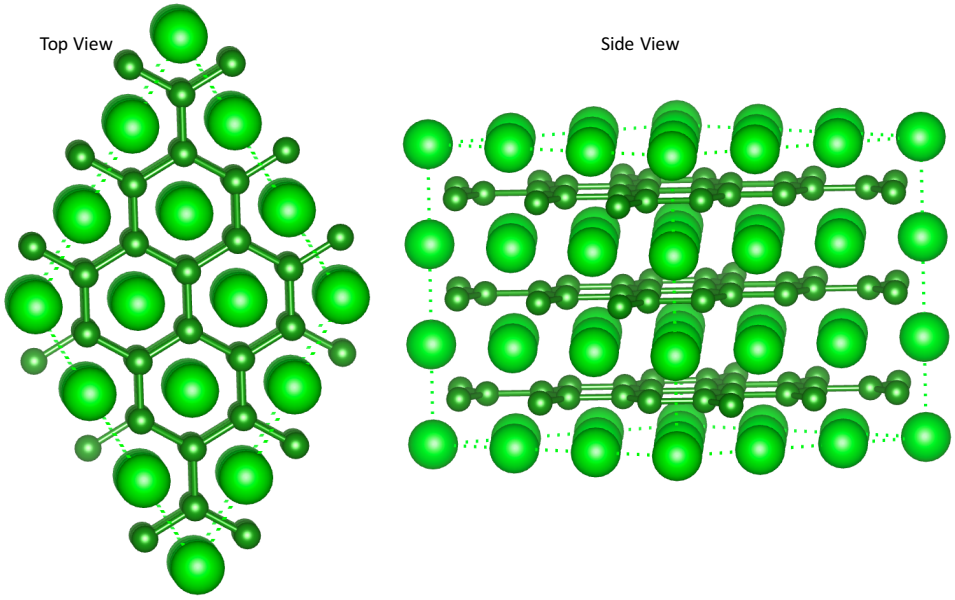

Fig. 2: Top view and Side view depiction of alternating layer of Zr and B in ZrB_2

The scattering contribution from imperfection or phonon-phonon interaction to the Matthiessen's resistance defines the extent of thermal transport [10]. Impurity changes periodicity in perfect crystal lattice. This induced disorder, strain, inhomogeneity changes the rate and mechanism of the scattering in the lattice. Analysis of the scattering rate in lattice

structure may include impurity, phonon-phonon, boundary, phonon-electron and vacancy scattering. And for independent scattering, the combined impact is computed using Mathieson's Rule as expressed;

$$\frac{1}{\tau_C} = \frac{1}{\tau_{imp}} + \frac{1}{\tau_{ph-ph}} + \frac{1}{\tau_B} + \frac{1}{\tau_{ph-e}} + \frac{1}{\tau_{vac}} \quad (1.1)$$

The parameters $\tau_{imp}, \tau_{ph-ph}, \tau_B, \tau_{ph-e}, \tau_{vac}$ denote the scattering time due to phonon interaction with impurity, phonon-phonon, boundary, phonon-electron, vacancy respectively. For the sake of this study, a perfect lattice is assumed, devoid of any mechanical imperfection except for the impurities under investigation. Phonon-phonon scattering accounts for the temperature dependence of phonon mean free path, $\lambda_{ph} \propto 1/T$ at elevated temperatures. Thus, from the combined relaxation rate, τ_C the scattering time is obtained to calculate thermal conductivity. Therefore, phonon decay and phonon lifetimes play important role in system relaxation energy and thermal conductivity [11]. Thus, using the classical phonon gas model, thermal conductivity is shown as a function of phonon average group velocity, V_s constant volume specific heat capacity, C_v and mean free path, λ_{ph} [12]

$$\kappa = \frac{1}{6\pi^2} \sum \int V_s \, C_v \, \lambda_{ph} \quad 1.2$$

Dissipation Function and Autocorrelation

A well-established method of calculating thermal conductivity in solids is the Green-Kubo formulation. The approach relates the heat flux density fluctuation resulting from thermal energy dissipation to the duration of the fluctuation. In this case, the dynamics for heat flux is attributed to small atomic level local fluctuations. Similar to fluctuation theorem, GK method

relates its linearized transport coefficient to the time dependence of equilibrium fluctuations in heat flux. The dependence on time-lag is obtained from the heat current autocorrelation. Denoting the heat current, J at times t and $t+\tau$ as J(t) and J($t+\tau$), the autocorrelation function, J(t) J($t+\tau$) is obtained. By integrating the resulting heat current autocorrelation function (ACF), Green-Kubo's expression for thermal conductivity is written as;

$$\kappa = \frac{V}{3k_B T^2} \int_0^\infty < J(t)\, J(t+\tau) > d\tau \qquad 1.3$$

and the temperature dependent term, $V/3k_B T^2$ is as expressed for three-dimensional solids of volume, V. Where k_B and T denote Boltzmann constant and temperature respectively. ACF computation and use for Green-Kubo has been used for recent studies on transition metal diborides and allows for appropriate cross-referencing and data comparisons within the limits of error depending on interatomic potentials [12, 14-15].

Computational Procedure:

Equilibrium Simulations and GK Calculations

To evaluate impurity effects on conductivity property of ZrB_2, molecular dynamics (MD) is used for all the simulations in this study. The Green-Kubo is an established method that uses the linear response theory to heat current fluctuation in an equilibrium homogenous system. All the dynamic variables required to compute the heat current are available in MD simulation process. Equation 2.1-2 show parameters required to quantify instantaneous heat current (**J**) in a simulation;

$$\mathbf{J} = \frac{\mathbf{d}}{\mathbf{dt}} \sum_{\mathbf{i}} (\mathbf{E_i} - \mathbf{h})\, \mathbf{r_i} \qquad 2.1$$

where E_i and h denote microscopic energy per atom and enthalpy per atom in the system. Under many body interaction, the derivative of the potential energy function gives the dynamic variables explicitly for the simulation to obtain heat current, **J.** It is expressed as;

$$\mathbf{J} = \sum_i \left\{ (\boldsymbol{E_i} - \boldsymbol{h})\boldsymbol{v_i} + \boldsymbol{r_i}[\, \boldsymbol{v_i}.\boldsymbol{F_i} + \sum_j \frac{\partial \boldsymbol{E_i}}{\partial \boldsymbol{r_j}}.\boldsymbol{v_j}] \right\}$$

$$= \sum_i \left\{ (\boldsymbol{E_i} - \boldsymbol{h})\boldsymbol{v_i} + \boldsymbol{r_i} \sum_j (\, -\boldsymbol{v_i}.\frac{\partial \boldsymbol{E_j}}{\partial \boldsymbol{r_i}}) + \boldsymbol{r_i} \sum_j \frac{\partial \boldsymbol{E_i}}{\partial \boldsymbol{r_j}}.\boldsymbol{v_j} \right\}$$

$$= \sum_i \left\{ (\boldsymbol{E_i} - \boldsymbol{h})\boldsymbol{v_i} + \sum_{j \neq i} \boldsymbol{r_{ij}} (\frac{\partial \boldsymbol{E_i}}{\partial \boldsymbol{r_j}}.\boldsymbol{v_j}) \right\} \qquad 2.2$$

where $\boldsymbol{v_j}$ is the velocity of atom j and $\boldsymbol{r_{ij}}$ is the position vector of atom, i due to neighbor j. These dynamic variables enable molecular dynamics compute heat current. As discussed in section 1, GK relates the phonon thermal conductivity to the time integration of the autocorrelation of the heat current function (2.2).

Randomly distributed 5%vol impurities in a 3x3x3 supercell of ZrB_2 at 300K with lattice parameters of a = 3.170 Å and c= 3.533 Å. All MD simulations used for thermal conductivity calculations were performed with the large-scale atomic/molecular massively parallel simulator (LAMMPS) [16]. Interactions between particles were modeled using the Tersoff potential developed by Tersoff and Benner [17]. Simulation boxes has been tested for convergence and optimal supercell size in our previous work and found no difference in convergence in comparison to 6x6x9 and 9x9x15. These are large enough sizes consistent with previous studies [15]. Two Microcanonical ensemble were employed in this study for optimal results. The structure was first thermalized and relaxed using mechanical thermodynamic ensemble, NPT to allow possible dimensional expansion or contraction. Equilibrium studies were then conducted

using NVE. A timesteps of 0.5 fs was used to simulate ten (10) configurations for every run. The heat current time trend simulation was collected under NVE for all directions of the lattice to compute the autocorrelation function (ACF) at thermal energy equivalence of T=300K. The initial simulations were performed for 5ns to ensure no noise or bump in the recorded ACF before truncating to 3ns on subsequent runs.

Following Green-Kubo (GK) method, using the time series data from MD simulations, the heat current autocorrelation function (HCACF) was calculated and integrated using the trapezoidal rule. Perfect ZrB_2 MD and subsequent thermal conductivity values obtained using GK method. Impurity heat current and thermal conductivity were similarly obtained from molecular dynamics and GK method with Lennard-Jones potential was used as additive potential with Tersoff interaction. Lennard-Jones prediction model has been shown to be consistent with experiments, particularly for solid argon [18]. More details about the usage or additive potential is in LAMMPs examples [16].

Density functional theory (DFT) was used for all the first principle calculations performed with Vienna *ab initio* simulation package [19, 20]. The projector augmented-wave (PAW) method with the generalized gradient approximation (GGA) of Perdew-Burke-Ernzerhof (PBE) exchange correlation functional at 500eV energy cutoff point was used. Monkhorst-Pack k-point grid was used following Brillouin zone integration as recommended for hexagonal structures [21]. The k-point is optimal for convergence before the cutoff energy such that the product atoms in lattice structure and k value is greater than the cutoff. For all the calculations in DFT, supercell size 3x3x3 has been considered. After VASP simulations, Hessian computation (stiffness matrix) were obtained from the resulting force constants by Phonopy and the atomic

displacements. Other phonon properties such as Phonon dispersion and thus density of states evaluation were calculated from the resulting VASP calculations using Phonopy.

Results and Discussions

Impurities (C, Si, Hf, W) Thermal Conductivity of ZrB_2

The thermal conductivities of impurities in zirconium diborides (ZrB_2) considered in this study are displayed in figure 3. The results clearly define decrease in thermal conductivity in the presence of impurities. With the thermal conductivity value for perfect ZrB_2 matching the range 87 to 99 W/m/K published in literatures [5, 15, 24]. Figure 3 shows the thermal conductivity (k)impact of 15 atoms (4%) impurities to the perfect lattice of ZrB_2, at temperature of 300K. Recorded k values for covalent bonding impurities of Si and C are generally lower that the metallic impurities Hf and W. Harrington et al. reported that increased content of carbon impurity decreased ZrB_2 thermal conductivity at different experimental temperatures due to lower mean free path [24]. Zimmerman in other reports observed that silicon carbide (SiC) impurity lowered the conductivity of ZrB_2 [24, 25]. These are interesting findings that require further detailed electronic and phononic properties research. Considering thermal conductivity correlation to mean free path, λ and carrier density of states, ρ in $k \approx \frac{1}{2} v_s * C * \rho * \lambda$, the lower k values can also be attributed to the potential drop in the number of available states due to impurities. From figure 5, the phonon density of states is obviously changed in the presence of various impurities both in the conduction region or/and in the valence region. Results presented is focused on impurity impact and microstructural implications and does not include temperature trend to minimize impurity migration [24, 25].

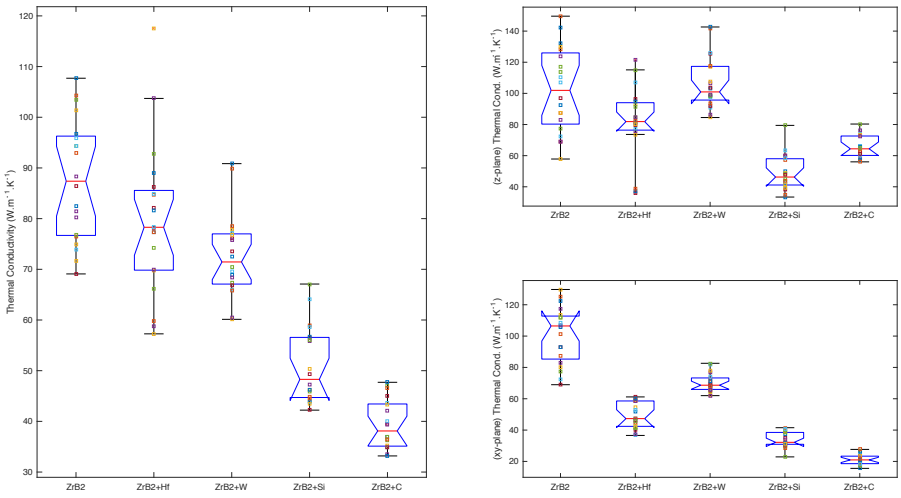

Fig. 3: Thermal Conductivity of ZrB2 w/o impurities of C, Si, Hf, W (a) isotropic k (b) k in z-plane and (c) xy-plane thermal conductivity

The resistance to thermal transfer through a material is critical, not only for tuning purpose but for characterizing impurity impact. For perfect crystals, this property (resistance) is inversely proportional to thermal conductivity. Impurities addition experimentally to powdered ZrB_2 require different densification technique creating discrepancies in reported thermal conductivity data [1, 2, 7, 24,25]. The induced thermal resistance due to defect can be obtained as s $r_{impurity} = r_{total} - r_{perfect}$. Where r_{total}, $r_{perfect}$ and $r_{impurity}$ denote the total resistance in the impure material, resistance in the pure material and the induced resistance due to impurity respectively. In this article, we present thermal resistance trend with impurity concentration range from 0 to 4% impurity atom (see Figure 4). Increased thermal resistance with increasing concentration of impurities was observed, however, the nonlinear nature of the correlation at 5 Hf atoms and 15 W atoms impurities suggest variation in the orientation of the impurity in the lattice structure. Using the impurity coefficient (slope), Si concentration impact can be proposed

as a property knob. Low thermal resistance (elevated k) values observed at 5 Hf atoms impurities and 15 W atoms impurities presents basis for future topics on the effects of orientation of impurities and its correlation to scattering mechanisms with variable concentration. For the metallic impurities, the decrease in k values is also related to size (radius) of the additive as W impurities lowered the thermal conductivity much more than Hf. Phonon properties observed are presented in the next section to provide further insight into the impact of impurities on thermal conductivity using microstructural parameters and variation in dynamic matrixes.

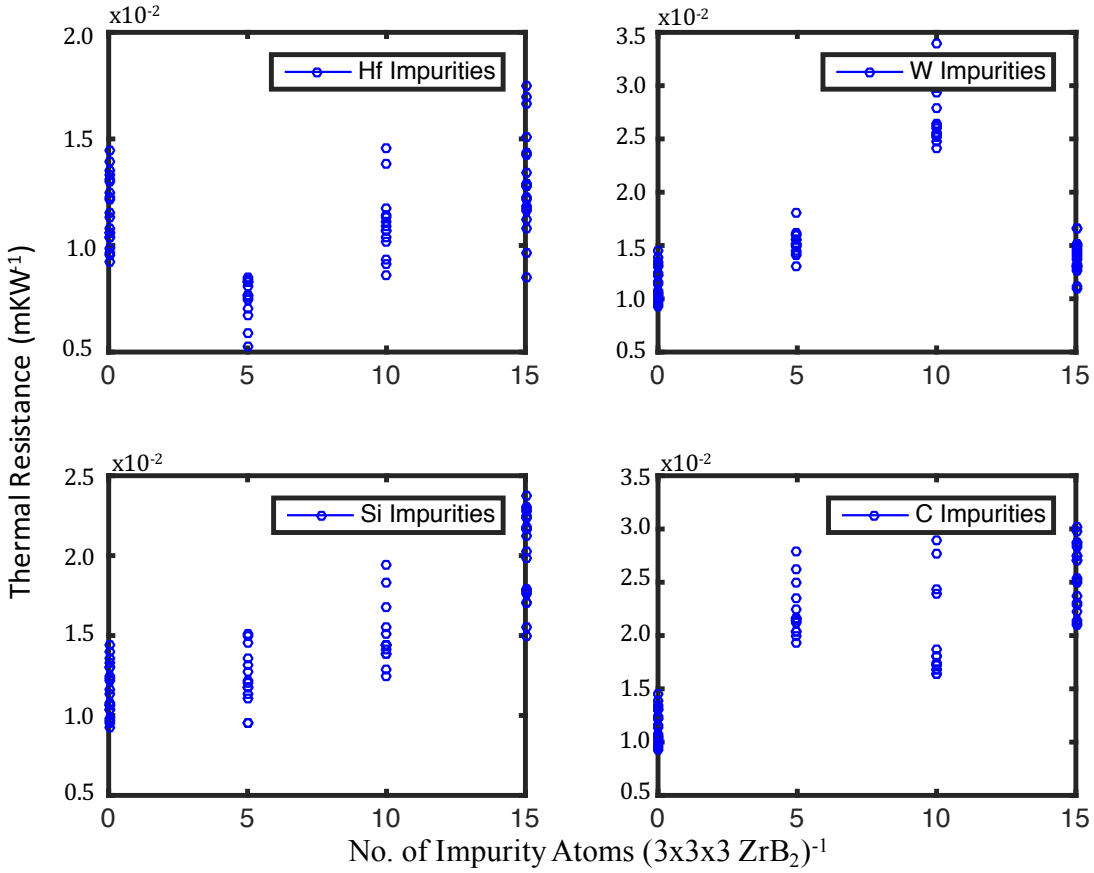

Fig. 4: total thermal resistance correlation to number of impurity atoms (Hf, W, Si, C)

Impurities (C, Si, Hf, W) Impact on Phonon Properties

Density of States: Enormous amount of data can be extracted from decay mechanism of phonons which is determined by scattering. Density functional theory (DFT) computation was performed for 81 atoms unit cell of ZrB_2 from which phonon properties were extracted. Figures 5-7 presents the total and projected density of states showing induced variation due to impurities. The results from the projected density of states (PDOS) shows that Zr 4d orbitals dominates the low frequency states while the B 2s and 2p orbitals dominates the high frequency for perfect ZrB_2 or with covalent impurities (C and Si). The electronic structure of C and the potential combination of hybrid orbitals (wave function) are similar to Boron and could best explain the project density of states in ZrB_2 with the impurity. However, additional states at are observed on Fig. 6 in the B dominated region appropriated to the presence of Si impurities. The number of states for the perfect ZrB_2 reduced with energy level. DOS for the covalently impurities are closely overlapped with the pure crystal but with more dominating states likely from the projected orbitals of silicon and carbon at higher energy. The metallic impurities show states dominating at lower energy and slow increase in the number of available states with frequency. Potential bonding interaction between the covalent nature of ZrB_2 with both Si and C is noticeable in the overlap, unlike with metallic impurities. Si extended the conduction band to 34.1eV, while C impurities made negligible changes to the conduction band. Both Hf and W impurities extended both the conduction and valence band. The conduction band in all cases are dominated by B orbitals. Increased width of the valence band denotes increase in electron delocalization and therefore reduced band gap. On the other hand, decreasing width of the conduction band indicates electron delocalization weakening. Occurrence of these impurities generated additional localized states and potential changes to conductive properties.

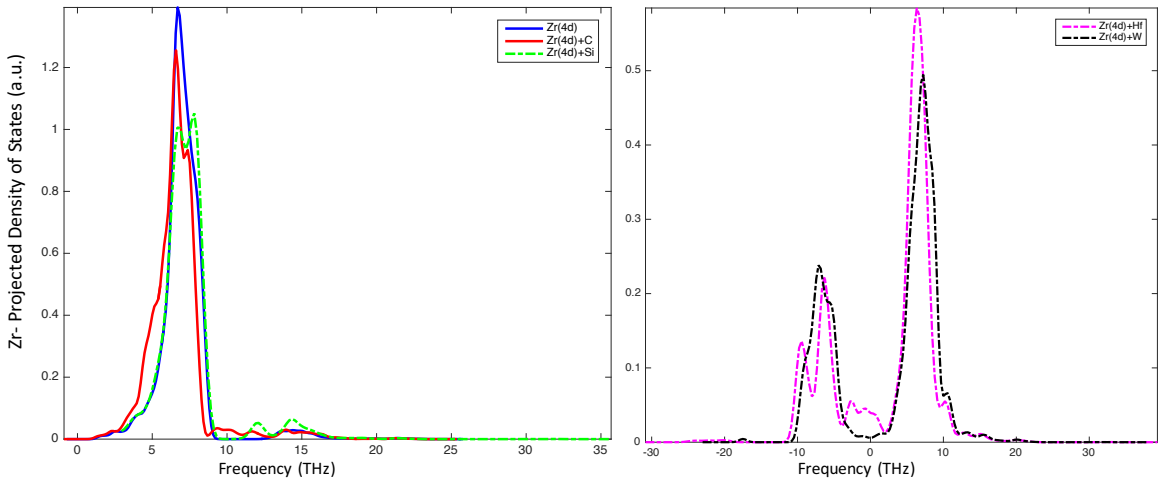

Fig. 5: Overlay of Zr orbital dominated region of the projected density of states (PDOS) for ZrB_2 with impurities (C, Si, Hf, W)

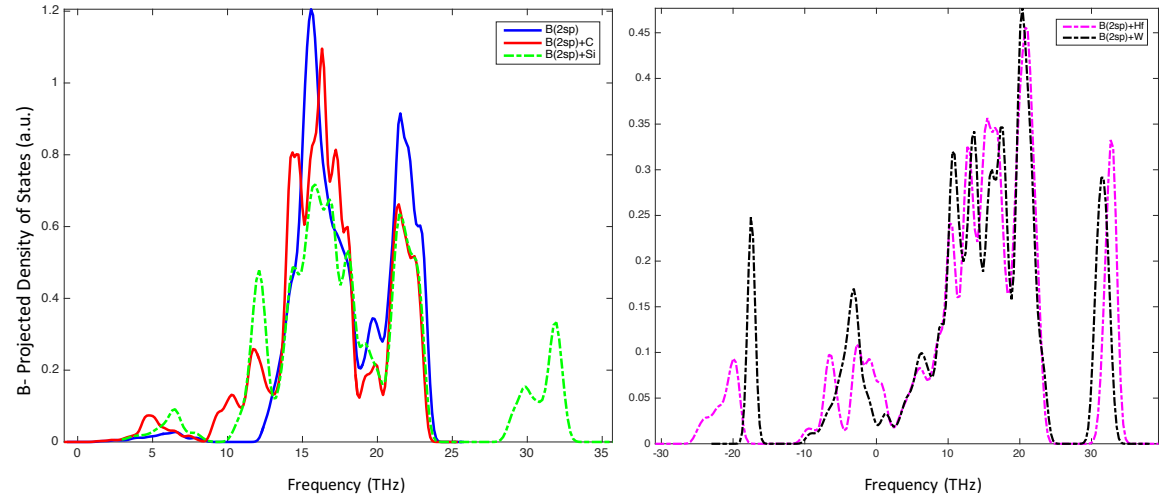

Fig. 6: Overlay of B orbital dominated region of the projected density of states (PDOS) for ZrB2 with impurities (Si, C, Hf, W)

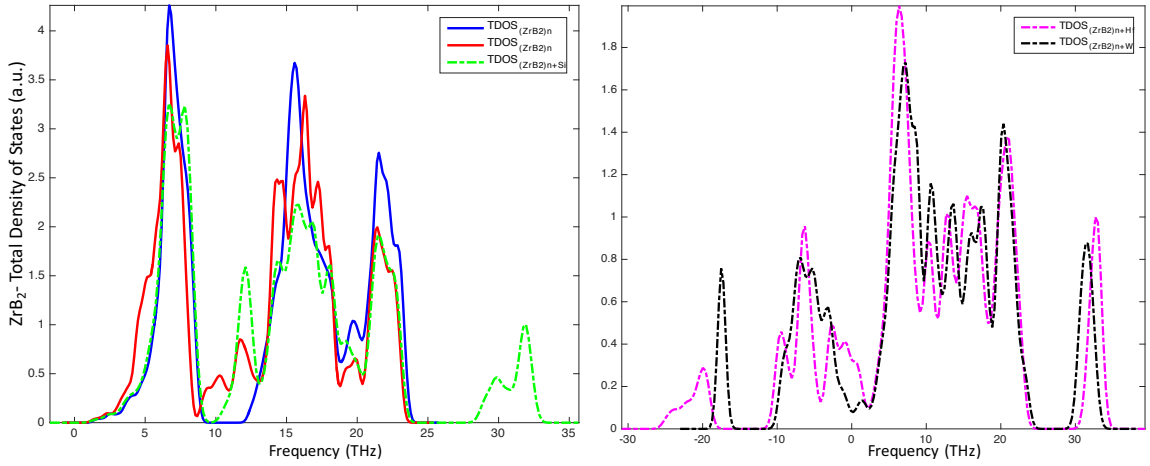

Fig. 7: Overlay of total density of states (TDOS) for ZrB2 with impurities (Si, C, Hf, W)

Density of states is not enough to characterize impurities in crystals, other phonon properties are required including stiffness variations in the lattice structure, lifetimes and group velocity. Phonon decay captured by its lifetime analysis can be obtained approximately from the normalized autocorrelation of total energy flux as;

$$\tau_{\mathrm{v}}^{\kappa} = \int_0^{\infty} \frac{\langle (\mathrm{E}_{\mathrm{v}}^{\kappa};\mathrm{t})(\mathrm{E}_{\mathrm{v}}^{\kappa};0)\rangle}{\langle (\mathrm{E}_{\mathrm{v}}^{\kappa};0)(\mathrm{E}_{\mathrm{v}}^{\kappa};0)\rangle}\,\mathrm{dt} \qquad 3.1$$

where $E_v^{\kappa};0$ and $E_v^{\kappa};t$ are the normal mode total energy at initial time and time t. Equation 3.1 is particularly applicable to study disordered lattices [26] maybe due to imperfections. However, in this study me delved into a more defining stiffness property.

Stiffness Matrix and Charge Density: Variations in stiffness properties of solid results in frequency drift across the quasi-harmonic range [26] which means changes in phonon scattering and lifetimes. The microscopic level distortion within the lattice structure as a result of phonon flux and geometric changes in the presence of impurities is captured in the stiffness matrix. Stiffness difference due to impurities is simply calculated by subtracting the stiffness property of the perfect ZrB_2 unit cell from the new stiffness obtained by adding impurities. The stiffness property is a hessian matrix of each atom across the frames (function of many variables). It is the second derivative of the energy eigenstate with respect to displacement of each atoms. Fig. 8 (right) shows the stiffness matrix plot for perfect ZrB_2 2x2x2 lattice structure with natural stiffness between the bonds. For this 24 atoms unit cell, each with 3 degrees of freedom gives a

total of 72 degrees of freedom. Therefore, one degree of freedom displacement for instance Zr in the x-direction impacts quantifiable force on the rest of Zr and also on Boron, particularly nearest neighbors. In Fig. 8(right), each block is modelled as a degree of freedom (number of unit cell atoms x 3. i.e. 24 atoms each with 3 displacement directions). Equation 3.2 presents the expression to calculate individual terms (coefficients) of stiffness matrix

$$H_{ij} = \frac{\partial^2 E}{\partial u_i \partial u_j} \qquad 3.2$$

where E represents the energy eigenstates of the atoms displaced in u-direction while i,j indices represent the ixj term on the nxn matrix.

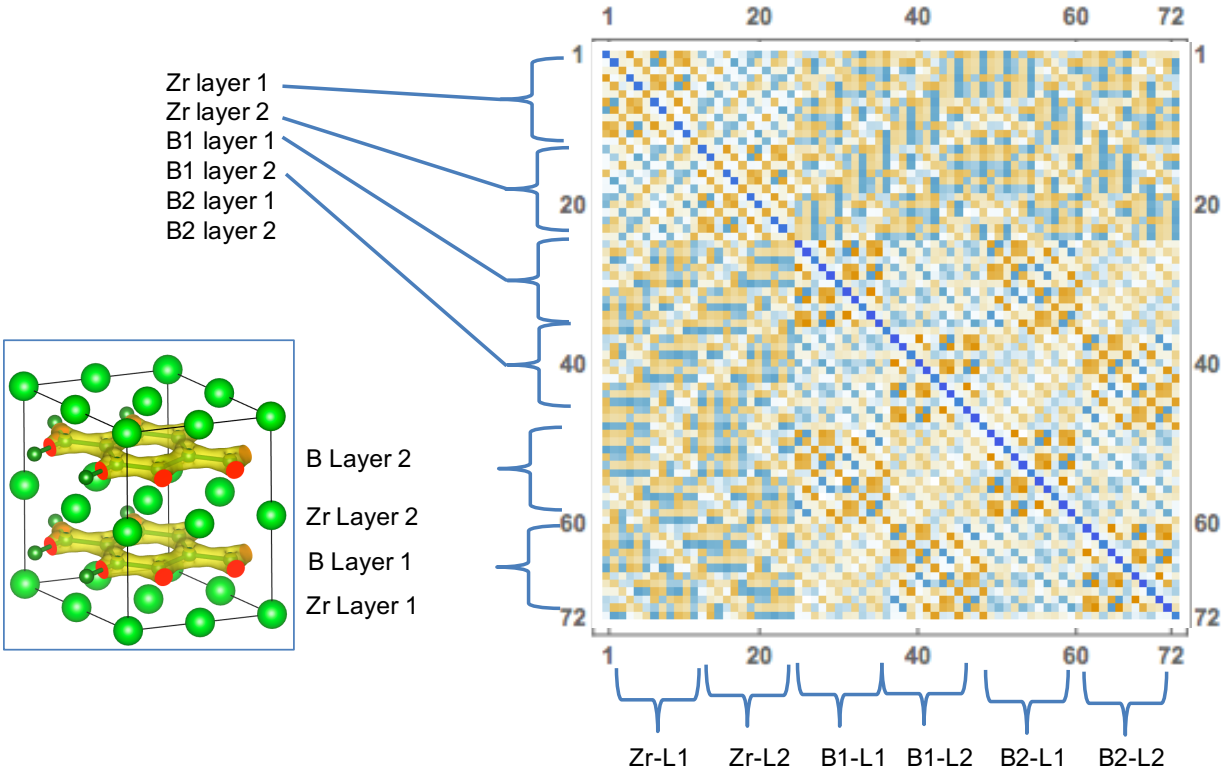

Fig. 8: (Right) Stiffness matrix plot for perfect ZrB_2 2x2x2 crystal structure and (left) its charge density for alternating Zr and B layers

Fig. 9 shows the stiffness difference with C, Si, Hf and W impurities which is calculated by subtracting the stiffness of the perfect ZrB_2 unit cell from the new stiffness obtained with impurity present. Hf shows no difference to the Zr stiffness but changes the stiffness around the B atoms, with alternating frames softer (orange) and stiffer (blue). W shows similar impact but slightly changes the stiffness around nearest Zr. For the covalent impurities as expected, there is not stiffness impact of Zr layers but interacts with the B-B bonds. The charge density difference was investigated to understand the underlying reasons for the observed interactions. The change in stiffness matrix is obtained using equation 3.3 below and plotted as presented in Fig. 9

$$\Delta H = H_{Defect} - H_{Perfect} \tag{3.3}$$

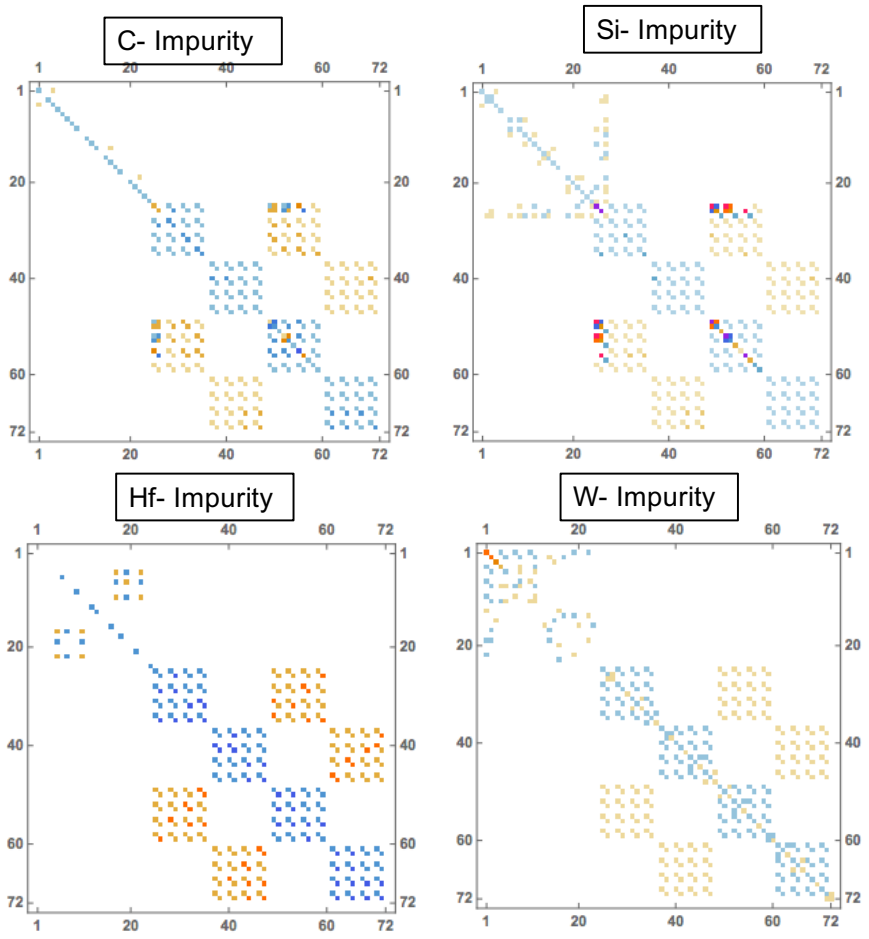

Fig. 9: Stiffness matrix difference imposed by impurities

The charge density wave structure is defined by the interaction between constituent atoms in a molecule. However, as the interaction changes so is the charge density around the atoms. For perfect ZrB2, the charge density is conducted away from Zr atoms and are mostly clouding the B atoms (see Fig. 8(left)). Fig. 10 shows the charge density difference with the various impurities. The charge density for the perfect crystal was obtained from density functional theory calculations. Similarly, the charge density of the structure with individual impurities are computed on DFT. The charge density difference is obtained from VESTA visual kit. It subtracts the perfect crystal lattice from the one with impurities in the same isosurface. The impact of the impurities on Boron is evident from the induced charge density around the boron atoms (or bonds).

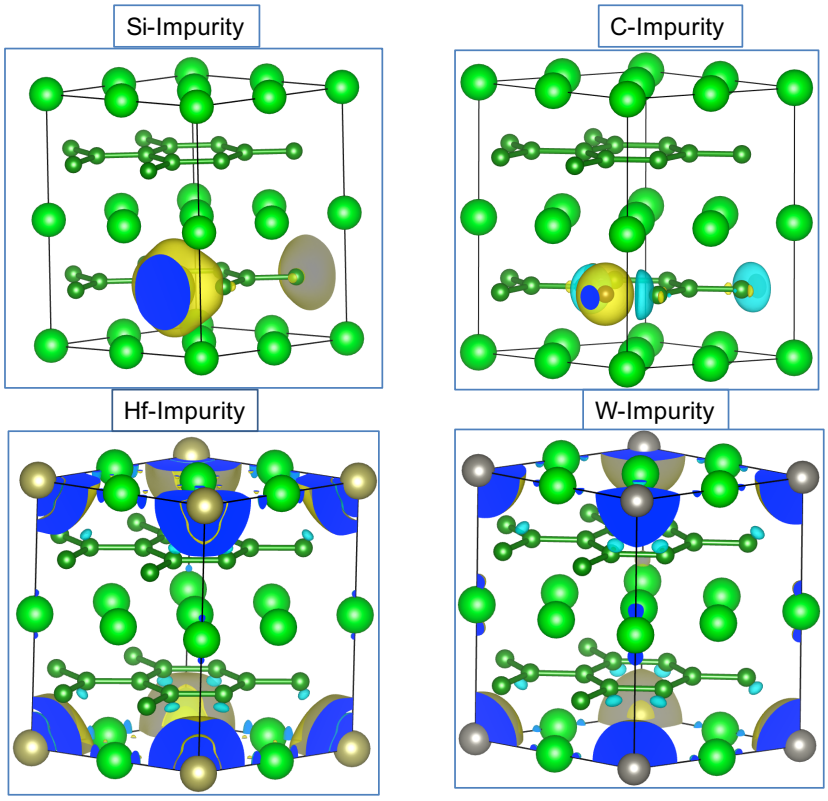

Fig. 10: charge density difference imposed by impurities

Understanding the stiffness contributions of various impurities and correlating it to the charge density difference is crucial. It enables one to setup simulation with impurities simply as mass defects (interstitials) and impose correction for Lennard-Jones (LJ) interatomic potential for

appropriate inter atomic spacing after the computing the stiffness matrix (hessian). This is an avenue for continuous improvement in future work.

Summary and Conclusion

Thermal-structural challenges posed by leading edge designs require some compulsory ultra-high temperature materials. Transition metal diborides exhibit unique thermal-mechanical properties of interest for this application. Fundamental knowledge of thermal transport as it relates to the localized energy in lattice crystal is crucial in further development of these (diborides) ceramic materials. Experimental procedures have established concepts of thermal conductivity in solids but challenged in methods to collect information of interest, particularly at the microscopic level. Molecular dynamics (MD) simulations correlates thermal conductivity to the complexities in atomic structure. Mode transition of energy carriers (phonons) and polarizations are underling characters of its scattering mechanisms which varies due to imperfection in lattices. Green-Kubo (GK) method applied here to calculate thermal conductivities shows the respective change in the property in the presence of various impurities. The approach gives insight into the HCACF convergence variations in the different axial directions. Decrease in thermal conductivity is consistent with reported increase in thermal resistance. Ab initio calculations was performed using DFT to investigate impurities impact on atomic level structure. Phonopy used to compute the dispersion property and obtained the density of states (DOS). Interestingly additional states are observed by adding Si, Hf and W impurities. This text contributes to the knowledge of atomic level characterization of ZrB_2 based UTHC and its correlation to thermal conductivity with or without impurities.

Acknowledgments.

This work used Oregon State University computing resources and also resources of the

Bioinformatics Computational Research Group in University of California Riverside.

References

1 Shuqi Guo, D. H. Ping, Yutaka Kagawa. Synthesis of zirconium diboride platelets from mechanically activated $ZrCl_4$ and B powder mixture. Ceramics International Volume 38, Issue 6, August 2012, Pages 5195-5200.

2 Kübra Gürcan and ErhanAyas. In-situ synthesis and densification of HfB_2 ceramics by the spark plasma sintering technique Author links open overlay panel. Volume 43, Issue 4, March 2017, Pg. 3547-3555.

3 Zhang, S. C; Hilmas, G. E; Fahrenholtz, W. G (2006). "Pressureless Densification of Zirconium Diboride with Boron Carbide Additions". Journal of the American Ceramic Society. 89 (5): 1544–50.

4 Kai-Long Hsiao. Calculation Aerodynamic Heating to A Stagnation Point of an High Speed 2-D Cylindrical Nose for Protection the Mechatronics System and Structure. WSEAS Transactions on Heat and Mass Transfer. Issue 11, Volume 1, November 2006

5 Sylvia M. Johnson. Ultra-High Temperature Ceramics: Application, Issues and Prospects. NASA-Ames Research Center, 2nd Ceramic Leadership Summit, August, 2011.

6 McClane, Devon Lee, "Thermal properties of zirconium diboride - transition metal boride solid solutions" (2014). Theses. Paper 7265.

7 A.L. Chamberlain, W.G. Fahrenholtz, G.E. Hilmas, and D.T. Ellerby, "HighStrength Zirconium Diboride-Based Ceramics," J. Am. Ceram. Soc., 87 [6] 1170- 2 (2004).

8 E.V. Clougherty, R.J. Hill, W.H. Rhodes, and E.T. Peters, Research and Development of Refractory Oxidation-Resistant Diborides. Part 2, Volume 2: Processing and Characterization. 2003.

9 M. Gasch, S. Johnson, and J. Marschall, "Thermal Conductivity Characterization of Hafnium Diboride-Based Ultra-High-Temperature Ceramics," J. Am. Ceram. Soc., 91 [5] 1423-32 (2008).

10 Ashcroft, N. W. and Mermin, N. D. (1976). Solid State Physics. W. B. Saunders, Philadelphia.

11 Zhun-Yong Ong, Eric Pop, and Junichiro Shiomi. Reduction of Phonon Lifetimes and Thermal Conductivity of a Carbon Nanotube on Amorphous Silica. Dept. of Physics, Univ. Illinois at Urbana-Champaign, Urbana IL 61801, USA. https://arxiv.org/pdf/1106.2612.pdf

12 Bing-Yang Cao and Zeng-Yuan Guo. Equation of motion of a phonon gas and non-Fourier heat conduction. Journal of Applied Physics 102, 053503 (2007)

13 D J Evans, E G D Cohen and G P Morriss, Probability of Second Law Violations in Shearing Steady States, Phys. Rev. Lett., 71, 2401, 1993.

14 Gubner, John A. (2006). Probability and Random Processes for Electrical and Computer Engineers. Cambridge University Press. ISBN 978-0-521-86470-1.

15 John. W. Lawson, Murray S. Daw and Charles W. Bauschlicher. Lattice thermal conductivity of ultra-high temperature ceramics ZrB2 and HfB2 from atomistic simulations. American Institute of Physics 110, 083507 (2011).

16 LAMMPS Molecular Dynamics Simulator". Sandia National Laboratories. Retrieved 2010-10-03.

17 J. Tersoff, Phys. Rev. B 37, 6991 (1988).

18 H. Kaburaki, J. Li, S. Yip, and H. Kimizuka, J. Appl. Phys. 102, 043514 (2007)

19 Kresse, G.; Furthmüller, J. Efficiency of ab-initio total energy calculations for metals an semiconductors using a plane-wave basis set. Comput. Mater. Sci. 1996, 6, 15–50.

20 Kresse, G.; Furthmüller, J. Efficient iterative schemes for ab initio total-energy calculations using a plane-wave basis set. Phys. Rev. B 1996, 54, 11169–11186.

21 Monkhorst, H.J.; Pack, J.D. Special points for Brillouin-zone Integrations. Phys. Rev. B 1976, 135, 5188–5192.

22 P. Vajeeston, P. Ravindran, C. Ravi, and R. Asokamani, "Electronic structure, bonding, and ground-state properties of AlB2-type transition-metal diborides," Physical Review B, 63 [4] 045115 (2001).

23 G P Shveikin, "The Chemical Bonding and Electronic Properties of Metal Borides," Russian Chemical Reviews, 63 [9] 711-34 (1994).

24 Gregory J. K. Harrington, Greg E. Hilmas, William G. Fahrenholtz. Effect of carbon on the thermal and electrical transport properties of zirconium diboride. Journal of the European Ceramic Society Volume 35, Issue 3, March 2015, Pages 887-896

25 James W. Zimmermann Gregory E. Hilmas William G. Fahrenholtz Ralph B. Dinwiddie Wallace D. Porter Hsin Wang. Thermophysical Properties of ZrB2 and ZrB2–SiC Ceramics. he American Ceramic Society. Volume91, Issue5 May 2008

26 Alan J. H. McGaughey* and Jason M. Larkin. Predicting Phonon Properties from Equilibrium Molecular Dynamics Simulations. Department of Mechanical Engineering, Carnegie Mellon University 5000 Forbes Ave., Pittsburgh PA 15213

6. Conclusions

A systematic study of a binary transition metal-diboride, zirconium diboride (ZrB_2) is presented in this document. The impact of impurities from sintering aids and point defects on the thermal properties of ZrB_2, particularly thermal conductivity, specific heat and thermal expansion. Paper I answered some vital questions on point defects formation energies and the impact on thermal conductivity of the material. It shows how these imperfections are structurally positioned, with Zr interstitials sticking out of plane while B remains in plane. The damaging impact of interstitial defects on thermal conductivity values computed using Green-Kubo method is different from the impact with vacancies. Paper II shows the heat capacity and thermal expansion of ZrB_2 in the presence of impurities. Negligible changes in the heat capacity was reported with different impurities. Increase in coefficient of thermal expansion with temperature was observed but decreased as it approached melting temperature of material. An exception is Hf impurities which improved stability in rate of expansion.

Paper III provides answers on stiffness matrix and charge density, induced by impurities as well as influence on thermal conductivity. The imposed changes in bond stiffness from the respective impurities computed by subtracting the stiffness matrix (hessian) of perfect ZrB_2 from the resulting stiffness matrix using Mathematica. The presence of Hf impurities does not show any difference to Zr bond stiffness but changes the stiffness around boron. W shows some difference around its immediate area of the impurity attributed to higher valence electron than Hf. For C and Si impurities, no changes to the stiffness observed around Zr, however we see some bonding interactions with the boron. Bimodal thermal conductivity values were observed, with covalently bonding impurities showing lower values than metallic defects. Higher conductivity values were observed in the c-direction across all configurations. Also, on this

paper is presented the charge density difference to understand the electronical doping or non-doping effects in the presence of impurities.

7. Future Work and Recommendations

For the next decade, resurging interest in ultra-high temperature ceramics such as ZrB_2, HfB_2, HfN, TaC will continue, mostly due to the limitations of hypersonic aircraft. Production of these ceramic materials and property tuning for advanced thermal design will determine extent of research. Therefore, approaches to thermal properties quantification and microstructure visualization needs further improvement.

The Green-Kubo approach depends on the integral of the heat current autocorrelation function (HCACF) which is a function of the heat flux. The first task on the study was to investigate the convergence of the HCACF and therefore size independent thermal conductivity. Other studies have reported both size dependent and size independent phonon frequency. This discrepancy could be investigated further to develop an approach for characterizing the uncertainties associated with the HCACF to synchronize approach globally.

Decomposition of thermal flux into phonon components extends from characterizing the phonon modes (wave vectors), polarization (longitudinal and transverse waves) to acoustic and optical phonon branches contributing to is conductivity or refractory property. Further classical and quantum investigation of descriptive concepts of phonons to improve atomic based description of the microstructure for both stoichiometric and impurity defects. This will also require a standardized method for defect introduction for comparable data.

The role of density of states in calculating specific heat capacity as discussed in chapter 4 warrants further study at it relates to impurities. Metallic impurities lowered the peak specific heat capacity for ZrB_2 proportionally to the intensity curve. Whether the lower phonon density of states resulted in higher electronic density of states could not be investigated in this study. Also,

increased library of impurities including molecular impurities should be investigated for offset these refractory properties.